Current Control for a Single-Phase Grid-Connected Inverter Considering Grid Impedance

by

Jiao Jiao

A dissertation submitted to the Graduate Faculty of
Auburn University
in partial fulfillment of the
requirements for the Degree of
Doctor of Philosophy

Auburn, Alabama
August 5, 2017

Keywords: Grid-connected inverter, grid impedance, current control method

Approved by

Robert Mark Nelms, Chair, Professor of Electrical and Computer Engineering
John York Hung, Professor of Electrical and Computer Engineering
Steve Mark Halpin, Professor of Electrical and Computer Engineering
Robert Neal Dean, McWane Professor of Electrical and Computer Engineering

Abstract

The voltage source inverters are typically used to connect between distributed generation and the utility grid. In the grid-connected inverter, an output filter is often utilized in the inverter terminals to reduce the pulse width modulation (PWM) switching harmonics. To achieve a sinusoidal grid current with unity power factor, the single-loop proportional integral (PI) or proportional resonant (PR) controller is often utilized for current control in the grid-connected inverter. However, in the distribution system, the grid can have a large impedance, which will affect the inverter control performance, even the stability of the inverter system. Presented in this work are four control methods aimed at reducing the effect of the grid impedance.

The impedance-based control is designed based on the relationship between the inverter output impedance and the grid impedance in the frequency domain. Through the analysis of the inverter output impedance in the frequency domain, the current controller parameters can be adjusted to regulate the output impedance to improve the control performance when the inverter is connected to a large grid impedance.

State feedback control combined with a PI/PR controller is a robust control method. Based on the pole placement method, the system stability and dynamic performance can be specified directly by determining the closed-loop pole locations. The system stability, robustness to grid impedance uncertainties, as well as damping to reduce the LC filter resonance can be improved.

Gain scheduling control is an adaptive control, which adjusts the controller parameters to make the system robust to grid impedance variations based on the grid impedance estimation. An

optimal gain is determined by the desired controller bandwidth and the phase margin of the system. Therefore, the inverter control performance can be maintained even with the grid impedance variation.

Grid-current observer-based compensation method aims to compensate for disturbances from the grid side; two different compensation control structures are proposed. The feed forward compensation uses the estimated grid current as a feed forward signal. The modified disturbance observer is utilized to compensate for the disturbance introduced into the inverter system. Both of the compensation methods are based on a grid current observer.

Experiments were implemented on a 1 kW Texas Instruments single-phase grid-connected inverter with an LC filter to verify the effectiveness of the control methods introduced.

Acknowledgments

I would like to express my sincere appreciation to my advisor, Dr. R. Mark Nelms, for his patient guidance, constant support and encouragement during my study at Auburn University. I feel very lucky to have such a highly respected advisor who gave me the freedom to think and to explore, and help me when I encountered difficulties. He taught me how to think, which I think it is an invaluable treasure for my future career and life.

I would also like to thank Dr. John Y. Hung not only for the help in my research, but also for the attitude towards life and work. I'd like to thank Dr. S. Mark Halpin for a lot of knowledge I gained from his courses. And I'd like to thank Dr. Robert N. Dean for serving as my committee members. I would like to thank all my committee members for their supports and suggestions for this work.

I would like to thank my family for their love and concern all these years. With my heartfelt respect, I would like to thank my parents, Hongyou Jiao and Rongxiang Liu, for their continuous love, support and encouragement throughout my life.

Table of Contents

List of Tables

List of Figures

CHAPTER 1 INTRODUCTION

1.1 Background

With increasing concerns about the impact of burning fossil fuels on global climate change, renewable energy such as solar and wind are getting more and more attention for their environmental friendly feature [1]. The voltage source inverter (VSI) is widely used as the interface between a renewable energy source and the utility grid. The VSI is a power electronic converter that can convert direct current (DC) to alternating current (AC) at a required voltage level and frequency. Figure 1.1 shows the general structure of a typical grid-connected inverter. It consists of fast switching devices, such as insulated gate bipolar transistors (IGBTs), which generate the desired output voltage through pulse width modulation. However, pulse width modulation can cause high frequency switching harmonics in the output current. In order to reduce the current switching ripple, a filter is commonly adopted for the VSI inverter in a grid-connected arrangement [2].

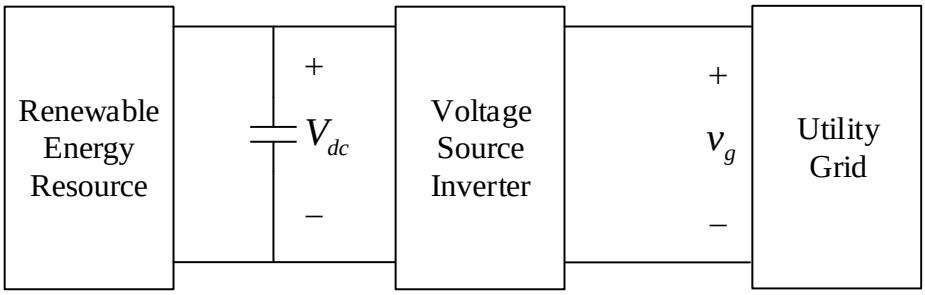

Figure 1.1 General structure of a typical grid-connected inverter.

Many grid-connected inverters are installed in the distribution system, which is characterized by long distribution lines and low power transformers [3]. An inductive grid reactance would decrease the resonant frequency of the inverter output filter, while a capacitive grid reactance would introduce other resonant peaks into the system. Moreover, load conditions

may have significant effect on the grid impedance as it changes over time [4]. Accurate modeling of the distribution network is important for transient and steady state performance analysis. Several researches have proposed different models for the utility grid at the distribution level [5, 6, 7]. However, exact impedance modeling of a distribution network is difficult because of the complexity and dynamic nature of the system.

In a traditional radial network, the grid impedance seen by a grid-connected inverter is determined mainly by its distance from the substation transformer, which can be modeled as an inductor in series with a resistor. For simplification, the grid at the point of common coupling (PCC) is modeled by its Thevenin equivalent circuit, consisting of an ideal voltage source in series with the grid impedance [7]. From an inverter controller point of view, this simple model has been employed by many researchers to address the impact of the grid on inverter operation [3,6,7,10,40,59]. The term "weak grid" is used in this work to describe the situation where the grid impedance is much larger than the filter inductance of the inverter [8].

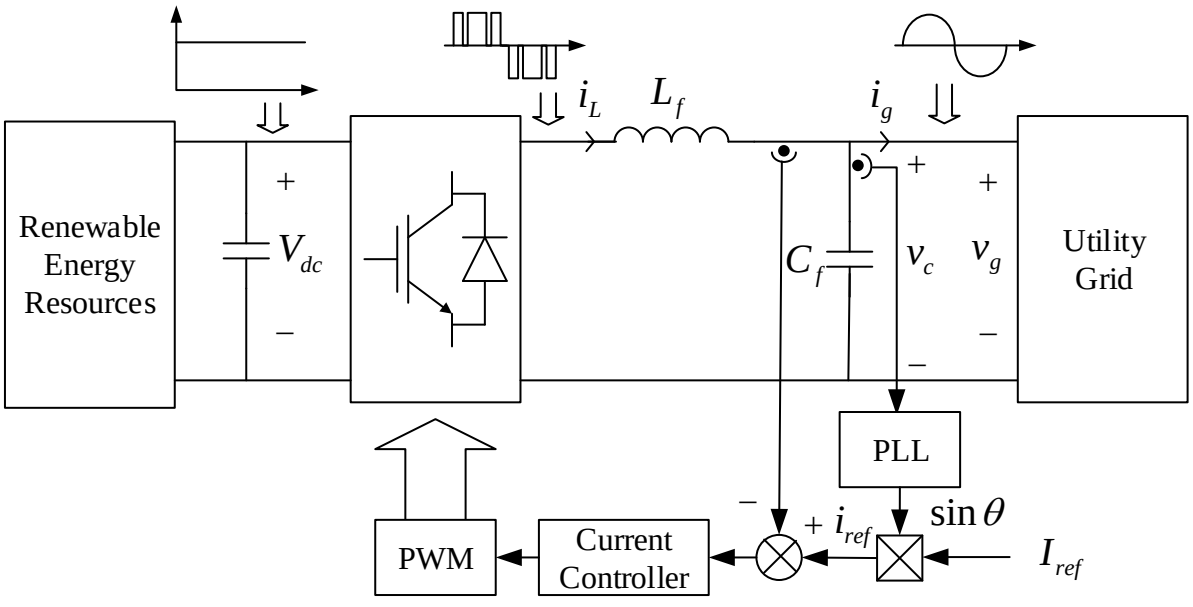

Figure 1.2 Control structure of a single-phase grid-connected inverter.

Figure 1.2 shows the control structure of a single-phase grid-connected inverter. Since the current switching harmonics caused by the pulse width modulation nature of the inverter output voltages should be kept under the IEEE standard limits, an L/LC/LCL filter is placed between the inverter and the utility grid. Compared with the L filter, the LC and LCL filters haver better performance in attenuating high frequency harmonics with a smaller component size and weight. However, the LCL filter is third order, which can introduce a resonant peak into the system that will cause an oscillation. For small power inverter (a few kW), an LC filter is a better choice for the switching harmonics attenuation [2]. Currents i_L and i_g are labelled in Figure 1.2. In order to achieve a sinusoidal current i_g with unity power factor, a current controller is usually used to track the reference, which is generated using the grid voltage phase detected by the phase lock loop (PLL) and the current amplitude command.

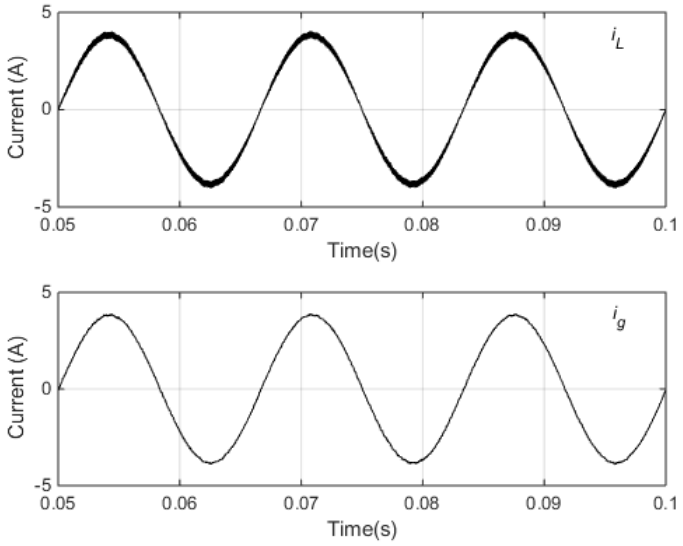

Figure 1.3 Inductor current i_L (upper) and grid current i_g (lower) waveform.

A current controller is an important requirement of a grid-connected inverter. It is not only responsible for reference tracking, but also system stability and response to grid disturbances. Generally, the current controller design for a grid-connected inverter doesn't take the grid

impedance into account. Researchers have shown that the grid impedance can affect the control performance of grid-connected inverter and stability of the system and lead to harmonic resonance [9, 10, 11, 12]. The injected grid current can be greatly distorted by the grid voltage harmonics [1,3,4]. Therefore, studies of the grid impedance effect on the inverter system are necessary.

1.2 Control Methods

Many control methods have been investigated in the literature for grid-connected inverter to achieve the goal of high quality output current and robustness to grid disturbance. A brief description of these is given below.

1.2.1 Single-Loop Control

The single-loop approach often uses a proportional-integral (PI) or proportional-resonant (PR) controller for inverter current control [13] [14]. A PR controller can track the current reference without steady state error, but it does not have high gain at non-resonant frequencies [15, 16, 17]. A PI controller is simple to implement, but it cannot eliminate the steady state error at the grid frequency [18] [19]. Although the single-loop control has been widely used due to its simplicity, desirable stability margins and dynamic performance, it has the disadvantage that it cannot guarantee the system bandwidth and resonance rejection at the same time [12].

1.2.2 Multiloop Control

To improve the transient and steady state performance of the system, a multiloop control can be used with the outer loop ensuring steady state reference tracking and the inner loop ensuring fast dynamic compensation for system disturbances and improving stability [20, 21, 22, 23, 24]. Multiloop control inherently provides damping effects to the inverter system and can therefore solve the limitations of the conventional single-loop control [24].

1.2.3 Deadbeat Control

Deadbeat control is an attractive control method, because it can reduce the steady state error to zero in a finite sampling period [25, 26, 27, 28]. In addition, it has the advantage of fast dynamic response and good steady state performance. However, this control method is sensitive to parameter uncertainty and measurement noise, which might cause system stability issues.

1.2.4 Hysteresis Control

Conventional fixed hysteresis-band controller has the advantage of fast current control response and inherent peak current limiting capability, but it has a variable switching frequency. Although an adaptive hysteresis-band controller can achieve a fixed switching frequency, it highly depends on the system parameters to maintain a constant modulation frequency [6] [29]. Therefore, the control performance might be degraded due to its sensitivity to system parameter variations.

1.2.5 State Feedback Control

State feedback control has been used in many applications such as uninterruptible power supply (UPS) and considered to be more comprehensive than the transfer function based design [30, 31, 32, 33, 34, 35, 36]. Pure state feedback control cannot eliminate steady state errors. An integrator or resonant controller is often used in conjunction with state feedback to achieve zero steady state error. By proper design of the closed-loop poles, it can ensure the system stability even with a weak grid.

1.2.6 Adaptive Control

Recently, many adaptive control methods such as model reference adaptive control [37] and gain scheduling control [38] [39] have been used to tune the controller parameters to improve the controller performance. Model reference adaptive control adjusts the controller parameters based on the difference between the output of the system and the output of a reference model, but

it has the possibility of making the system unstable. The gain scheduling method is a more conservative adaptive control method. It adjusts the controller parameters based on the grid impedance value, which can maintain the controller performance when the grid impedance is large.

1.2.7 H-Infinity Control

H-infinity control is also a promising method to deal with the stability problem caused by the grid impedance uncertainty [40]. It can exhibit high gains around the line frequency while providing enough high frequency attenuation to make the control loop stable. The disadvantage of this method is that it is valid for a predefined range of the grid impedance. If the grid impedance is beyond this range, the weight functions of the H-infinity controller must be recalculated.

1.3 Research Objectives

The objectives for the current controller design of the single-phase grid-connected inverter with LC filter are as follows:

- Ensure the inverter output current can track the reference current precisely and with low harmonics to meet the requirement of standard IEEE-1547 [41], shown in Table 1-1.
- Guarantee the stability of the system in the presence of grid impedance and robustness to grid impedance variation.
- Good harmonic rejection ability in suppressing grid voltage distortion.
- The ability to damp the resonant frequency caused by the LC filter and grid impedance.

Table 1-1 Distortion Limits for Distribution Generation Systems Set By IEEE-1547.

Odd Harmonics	Distortion Limit
$3^{rd} – 9^{th}$	< 4.0 %
$11^{th} – 15^{th}$	< 2.0 %
$17^{th} – 21^{st}$	< 1.5 %
$23^{rd} – 33^{rd}$	< 0.6 %

1.4 Organization of the Dissertation

The focus of this dissertation is the development of a robust control strategy for a single-phase grid-connected inverter when connected to a weak and distorted grid. Each chapter in this dissertation is organized as below.

Chapter 1 introduces the background of this research and presents the research objectives. It also provides the control methods used for a grid-connected inverter.

Chapter 2 describes the 1 kW Texas Instruments single-phase grid-connected inverter with an LC filter and its mathematical model.

Chapter 3 explores the grid impedance effect on the stability of a single-phase grid-connected inverter based on an analysis of the inverter output impedance. By modeling the output impedance of the inverter, it can be determined that the proportional gain and integral gain of the controller have an effect on the output impedance. Analytical and experimental results show that by adjusting the PI controller parameters, the ability for harmonic reduction and stability of the system can be improved.

Chapter 4 investigates the state variable feedback control combined with a PI/PR controller for a single-phase grid-connected inverter operating under weak grid conditions. State feedback control can offer full controllability, which can enhance stability and increase damping to reduce

the LC filter resonance. A PI/PR compensator is augmented with state feedback control to achieve a more accurate current reference tracking. Therefore, state feedback control combined with a PI/PR controller has been utilized to maintain inverter performance under weak grid conditions.

Chapter 5 introduces a gain scheduling control strategy based on grid impedance estimation to adjust the controller parameters so that the system is robust to grid impedance variations. An optimal gain is determined based on the controller bandwidth of the system and the phase margin of the system. Simulation and experimental results demonstrate the effectiveness of this method.

Chapter 6 presents a grid current observer based compensation control for a single-phase grid-connected inverter that is connected to a weak grid. Two different compensation control structures are proposed. One is a feed forward method, which uses estimated grid current as a feed forward signal. The other one is a modified disturbance observer method, which compensates for the estimated disturbance. Disturbance rejection ability can be improved by adopting these methods.

Chapter 7 presents conclusions and suggestions for future work.

CHAPTER 2 SINGLE-PHASE INVERTER TESTBED AND MODEL

The control performance of the grid-connected inverter will be affected when it is connected to a weak grid. Therefore, it is necessary to design a robust controller to improve the control performance of the grid-connected inverter under a weak grid. Before investigating the design of the inverter controller, a mathematical model describing the system is needed. In this chapter, a 1 kW Texas Instruments single-phase grid-connected inverter with an LC filter is introduced. Its continuous time and discrete time models are developed. This experimental testbed was utilized to verify the effectiveness of the control strategies proposed in later chapters.

2.1 Inverter Description

Figure 2.1 shows the 1 kW Texas Instruments single-phase grid-connected inverter. Its main function is to convert the DC power into grid-synchronized AC power. The main components of the inverter include IGBTs, DC capacitance, an LC filter, a microcontroller board, analog measurement circuits and other auxiliary circuits for safety.

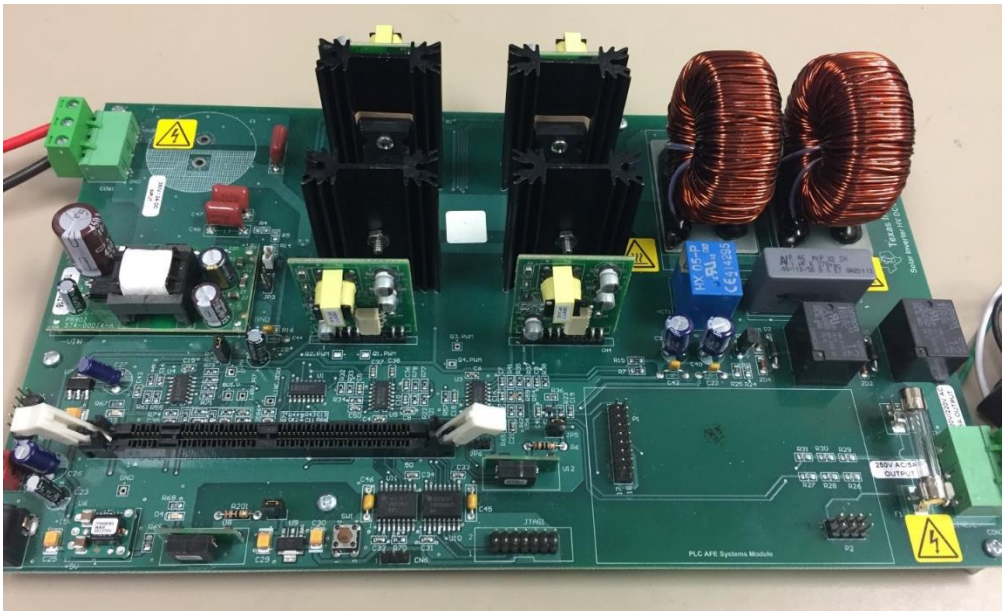

Figure 2.1 Photograph of the Texas Instruments 1 kW single-phase grid-connected inverter.

2.1.1 Power Stage

Figure 2.2 shows a schematic diagram of the single-phase grid-connected inverter. The inverter is connected to the grid through an LC filter, which consists of the inverter side inductance L_f and the filter capacitance C_f. R_f is the parasitic resistance of inverter side inductance. Two filter inductances are employed to attenuate the common mode noise current in the circuit. In addition, electromagnetic interference (EMI) effects are reduced. V_{dc} is the input DC link voltage, and v_{inv} is the output voltage of the H-bridge inverter. The inductor current, i_L, is sensed for current control to regulate the injected current with lower harmonics and unity power factor. A phase lock loop (PLL) is used to synchronize the inverter current reference with the grid voltage. The current reference magnitude I_{ref} is set in the microcontroller according to the specified active power of the inverter.

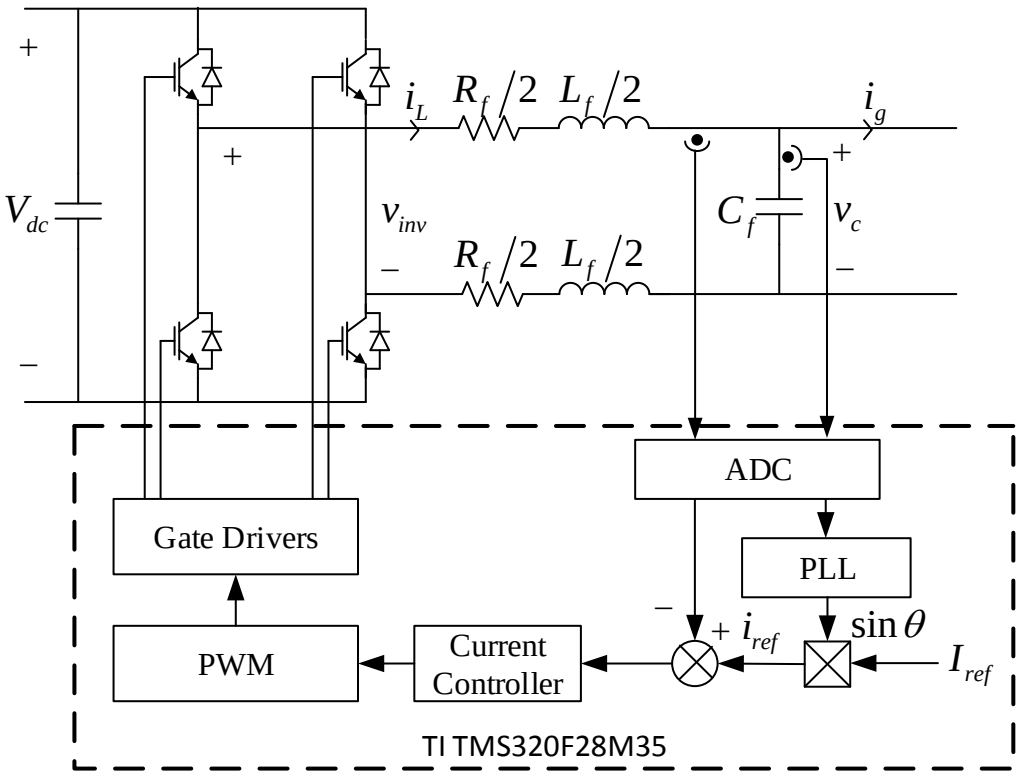

Figure 2.2 Schematic structure of a single-phase grid-connected inverter.

The filter inductance was designed mainly based on the desired inverter output current ripple [2]. The maximum current ripple can be expressed as: $\Delta I_{\max} = V_{dc} T_s / 4L_f$. Therefore, a 7 mH inductor was selected to make the maximum current ripple within 20% of the rated output current. A 1 μF capacitor was selected to provide reactive power less than 5% of the rated power [2]. The system parameters for the inverter shown in Figure 2.2 are provided in Table 2-1 [42].

Table 2-1 System Parameters [42]

System Parameter	Symbol	Value
DC-link Voltage	V_{dc}	380 V
Utility Grid Voltage	v_g	120 V
Fundamental Frequency	f_0	60 Hz
Inductor Parasitic Resistance	R_f	0.4 Ω
Filter Inductance	L_f	7 mH
Filter Capacitance	C_f	1 μF
Switching Frequency	f_{sw}	19.2 kHz
Sampling Frequency	f_s	19.2 kHz
Voltage Sensor Gain	H_v	0.001
Current Sensor Gain	H_i	0.0484

2.1.2 Controller Stage

The TMS320F28M35 microcontroller card, shown in Figure 2.3, is used for digital control of the inverter system. The main peripherals used are [43]:

- Enhanced pulse width modulator (ePWM)

The ePWM module has the following features: 16-bit time-base counter, two PWM outputs, dead-band generation, trigger the ADC start of conversion (SOC), and PWM chopping by high frequency carrier signal. This module is responsible for PWM generation to drive the IGBTs in the inverter. The duty ratio calculated by the current controller is loaded into the PWM compare

register to produce the PWM output signals, which are made available to the driver circuit through the GPIO peripheral.

- Analog-to-Digital Converter (ADC)

The ADC module includes two 12-bit ADC cores with built-in dual sample-and-hold (S/H). It is responsible for converting the analog voltage and current measurements to digital signals used for the control loops, background routines and safety check.

Figure 2.3 Photograph of the TMS320F28M35 microcontroller card.

2.2 Mathematical Model

A mathematical model of the grid-connected inverter is necessary for controller design and performance analysis. Therefore, a continuous time model and a discrete time model of the inverter circuit shown in Figure 2.2 are developed, respectively.

2.2.1 Continuous Time Model

Since the VSI switching frequency is sufficiently higher than the power system fundamental frequency, the inverter circuit in Figure 2.2 can be represented by an "average switching model" [44] [45]. The inverter switches are represented by their average value over each carrier interval $v_{inv}(t)$, as shown in Figure 2.4.

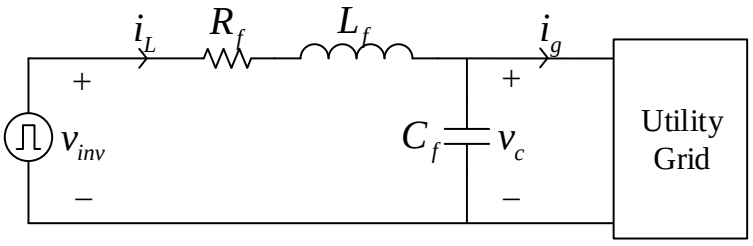

Figure 2.4 Average model of a single-phase grid-connected inverter.

A set of differential equations describing the plant system is developed according to Kirchhoff's laws. The circuit equations can be derived as follows:

$$L_f \frac{di_L(t)}{dt} + R_f i_L(t) = v_{inv}(t) - v_c(t) \tag{2.1a}$$

$$C_f \frac{dv_c(t)}{dt} = i_L(t) - i_g(t) \tag{2.1b}$$

The continuous time plant model is developed by taking the Laplace transform of the differential equation (2.1a). The transfer function between inductor current and the difference between the inverter output voltage and the capacitance voltage can be derived as

$$G_p(s) = \frac{I_L(s)}{V_{inv}(s) - V_c(s)} = \frac{1}{L_f s + R_f} \tag{2.2}$$

Since many power converters are controlled using a digital microcontroller, a sampling and computation delay will be introduced [46-48]. The current signal is sampled by an analog-to-digital converter, which introduces a sampling delay. This delay is caused by the zero-order hold (ZOH) effect, which is a half sampling period. The time domain diagram from sampling input to drive output is depicted in Figure 2.5. During the sampling period T_s, the sampled current $i(k)$ is used to calculate the duty ratio value $d(k)$. $u^*(k)$ is the PWM reference value loaded into the PWM compare register. It cannot be updated until the next time instant $(k+1)T_s$. The time interval between the sampling instant and PWM reference update instant is called the computation delay, which is one sampling period.

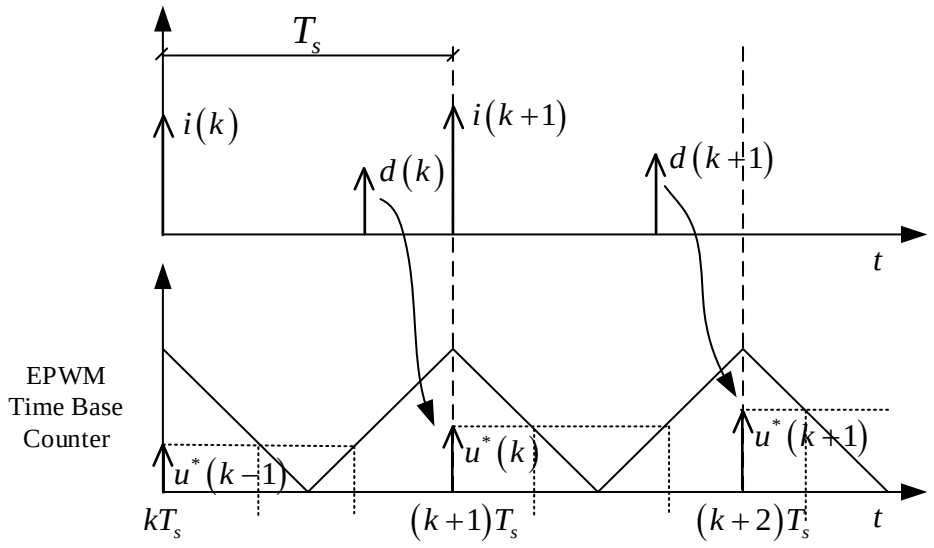

Figure 2.5 Delay introduced by symmetric PWM and sampling processes.

Therefore, the total delay can be approximated as one and a half of the sampling period. It can be modeled by using an exponential delay model in continuous time.

$$G_d(s) = \frac{1-e^{-0.5T_s s}}{s} \cdot \frac{1}{T_s} \cdot e^{-0.5T_s s} = e^{-1.5T_s s} \approx \frac{1}{T_d s + 1} \tag{2.3}$$

where $T_d = 1.5T_s$, and T_s is sampling period.

Since the switching frequency is sufficiently high, the pulse width modulator will have negligible impact on the inverter control dynamics. Therefore, the inverter bridge can be represented by a constant gain K_{pwm}, which is 1 for simplification [45]. The inverter circuit in Figure 2.2 can be represented by its average model block diagram form as shown in Figure 2.6.

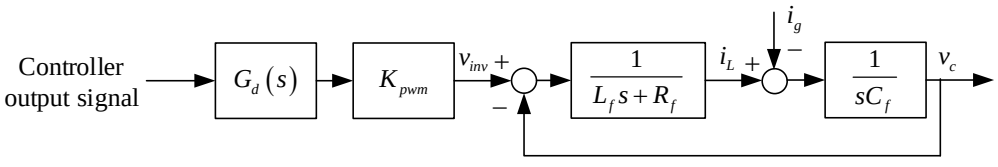

Figure 2.6 Block diagram for a single-phase grid-connected inverter.

2.2.2 Discrete Time Model

The direct discrete design of the current controller requires a discrete time model for the inverter system. This can be achieved by converting the continuous time state space model to its discrete time state space model. The continuous time state space model for the single-phase grid-connected inverter can be derived according to (2.1a) and (2.1b), as shown in (2.4).

$$\begin{aligned} \dot{x}(t) &= Ax(t) + Bv_{inv}(t) + Ei_g(t) \\ y(t) &= Cx(t) \end{aligned} \tag{2.4}$$

where the state variables are the inductor current and capacitor voltage, $x = \begin{bmatrix} i_L & v_c \end{bmatrix}^T$. The control input of the system is the inverter output voltage v_{inv}, and the grid current i_g can be considered as a disturbance input to the system. The switching cycle averaged inverter output voltage v_{inv} is considered to be constant during sampling period. The state transition matrix A, input matrix B, disturbance input matrix E, and output matrix C are:

$$A = \begin{bmatrix} -R_f/L_f & -1/L_f \\ 1/C_f & 0 \end{bmatrix} \quad B = \begin{bmatrix} 1/L_f \\ 0 \end{bmatrix} \quad E = \begin{bmatrix} 0 \\ -1/C_f \end{bmatrix} \quad C = \begin{bmatrix} 1 & 0 \end{bmatrix} \tag{2.5}$$

The discrete time state space model is established in (2.6). Taking the zero-order hold effect into consideration leads to the following relationships between the continuous and discrete realization matrices:

$$\begin{aligned} x_d[k+1] &= F_d x_d[k] + G_d v_{inv}[k] + J_d i_g[k] \\ y_d[k] &= H_d x_d[k] \end{aligned} \tag{2.6}$$

where

$$\begin{aligned} F_d &= e^{AT_s} = L^{-1}\left\{(sI - A)^{-1}\right\} \\ G_d &= \int_0^{T_s} e^{A\tau} d\tau B \quad J_d = \int_0^{T_s} e^{A\tau} d\tau E \\ H_d &= C \end{aligned} \tag{2.7}$$

$$F_d = \begin{bmatrix} \cos(\omega_{res}T) & -\dfrac{\sin(\omega_{res}T_s)}{L_f\omega_{res}} \\ \dfrac{\sin(\omega_{res}T)}{C_f\omega_{res}} & \cos(\omega_{res}T_s) \end{bmatrix} \quad G_d = \begin{bmatrix} \dfrac{\sin(\omega_{res}T_s)}{L_f\omega_{res}} \\ 1-\cos(\omega_{res}T_s) \end{bmatrix} \quad J_d = \begin{bmatrix} 1-\cos(\omega_{res}T_s) \\ -\dfrac{\sin(\omega_{res}T_s)}{C_f\omega_{res}} \end{bmatrix}$$

$\omega_{res} = \sqrt{1/L_fC_f}$ is the resonant frequency of the LC filter. Since R_f is small, it's ignored in (2.7).

Due to the computation delay between the inverter output reference voltage and inverter output voltage, another state equation should be considered.

$$v_{inv}^{*}[k] = v_{inv}[k+1] \tag{2.8}$$

where v_{inv}^{*} is the inverter output reference voltage. Therefore, the discrete time state space model can be expressed as:

$$\begin{gathered} \underbrace{\begin{bmatrix} x_d[k+1] \\ v_{inv}[k+1] \end{bmatrix}}_{x[k+1]} = \underbrace{\begin{bmatrix} F_d & G_d \\ 0 & 0 \end{bmatrix}}_{F} \underbrace{\begin{bmatrix} x[k] \\ v_{inv}[k] \end{bmatrix}}_{x[k]} + \underbrace{\begin{bmatrix} 0 \\ 1 \end{bmatrix}}_{G} v_{inv}^{*}[k] + \underbrace{\begin{bmatrix} J_d \\ 0 \end{bmatrix}}_{J} i_g[k] \\ y[k] = \underbrace{\begin{bmatrix} 1 & 0 & 0 \end{bmatrix}}_{H} x[k] \end{gathered} \tag{2.9}$$

2.3 Grid Modeling

Grid impedance is an essential parameter for power grid modeling. It depends on the power grid structure and the connected loads. An accurate grid impedance model could be achieved by measuring the grid impedance at the point of interest. By injecting a harmonic current and measuring the voltage response, the grid impedance can be estimated [49, 50, 51]. Grid modeling based on the impedance measurement has been explored by many researches [52, 53, 54, 55, 56], and is beyond the scope of this work. Most of the voltage source inverters are installed at the distribution level, which mainly consists of long distribution lines and low power transformers as shown in Figure 2.7.

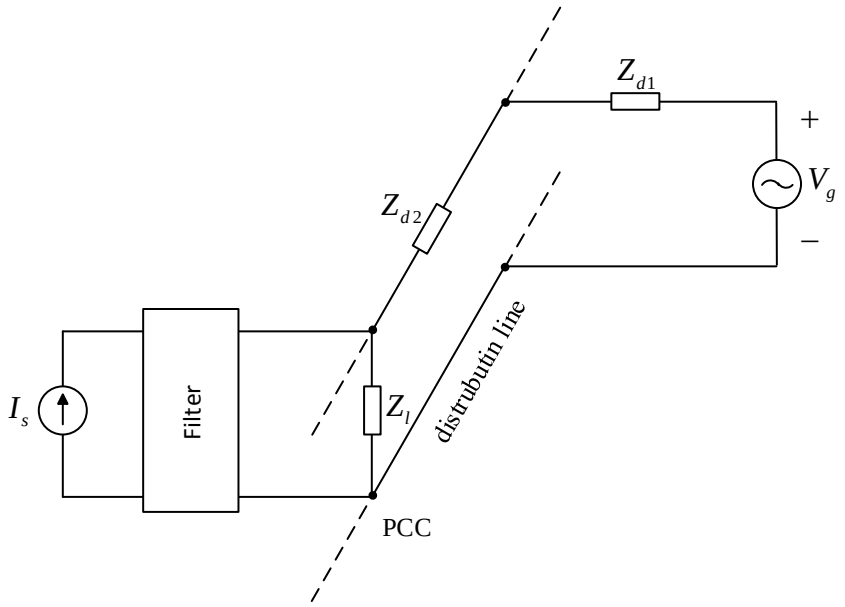

Figure 2.7 Impedance model representation of a distribution grid with an inverter connected [45].

To develop an equivalent network model at the point of common coupling (PCC) is important for the transient and steady state analysis of the grid-connected inverter system. The distribution system presents less interaction with residential area loads [34]. Therefore, from the inverter control point of view, the grid impedance at the PCC can be modeled as a paralleled capacitor and an inductor in series with a resistor [53] as shown in Figure 2.8. The capacitive impedance is introduced by the distribution line, transformer and reactive power compensation, and can cause a resonance phenomenon [36,48]. This would make the grid impedance characteristics more complex.

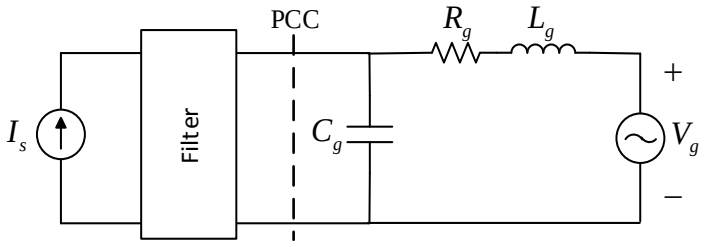

Figure 2.8 Grid modeling at PCC with an inverter connected.

The analysis of grid impedance effect on the inverter system is performed mainly in the low frequency range. For simplification, an assumption is made that the parallel capacitor effect is negligible at low frequency [53]. Therefore, the grid at the PCC can be modeled by its Thevenin equivalent circuit, consisting of an ideal voltage source in series with the grid impedance, as shown in Figure 2.9.

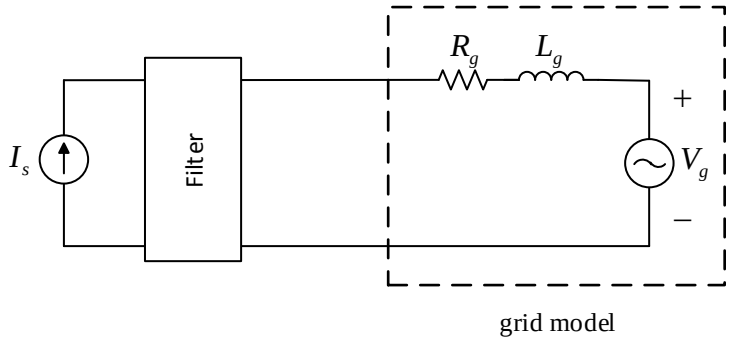

Figure 2.9 Simplified grid model at PCC with an inverter connected.

2.4 Experimental Testbed

An experimental testbed is utilized to verify the proposed control schemes. Figure 2.10 is a diagram of the experimental system. The single-phase VSI is directly coupled to the grid through a 1 kVA 1:1 isolation transformer. R_l is a resistor load required by TI for grid-tie operation. A Chroma programmable AC source model 61504 was utilized to simulate the grid voltage. All waveforms were recorded with a Tektronix MDO 3024 oscilloscope, and the harmonic analysis was performed by this scope. The grid impedance is modeled by an adjustable discrete impedance, which was inserted between the inverter and the AC source. Since the grid resistance offers a certain degree of damping, which can stabilize the system, a pure inductance is considered here to represent the worst condition.

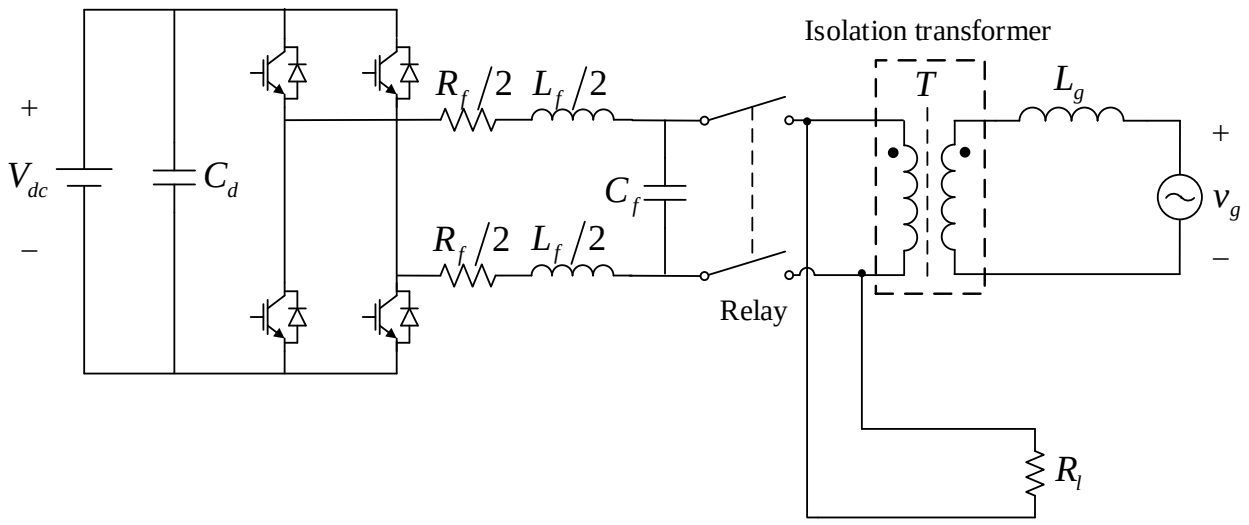

Figure 2.10 Configuration of the experimental system.

2.5 Inverter Operation without Current Control

Figure 2.11 is a block diagram for the single-phase grid-connected inverter without current controller. Experiments of inverter operation without a current controller were performed for ideal grid and distorted grid (10% 3rd harmonic, 5% 5th harmonic and 3% 7th harmonic) under different grid impedances (L_g = 1.5 mH, 2.5 mH, 6.5mH, 10.5 mH, 13.5 mH and 19.5 mH), which are shown in Figure 2.12 and Figure 2.13. The inverter output current harmonic analysis for an ideal grid and for a distorted grid are given in Table 2-2 and Table 2-3. It can be seen that without current control the harmonics of the inverter output current are much larger than the requirement set by the standard shown in Table 1-1.

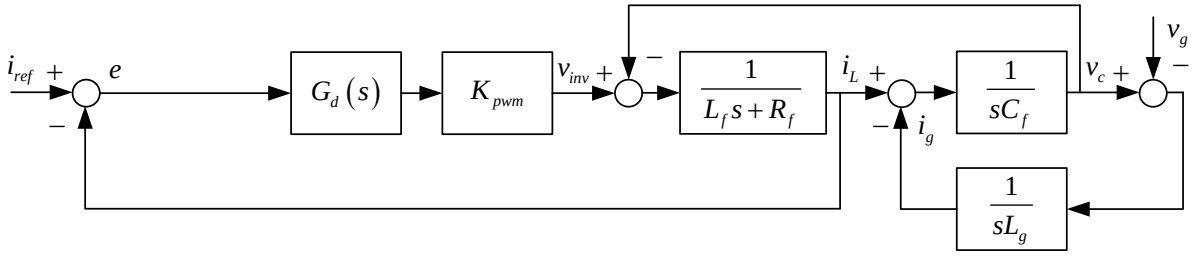

Figure 2.11 Block diagram for a single-phase grid-connected inverter without current controller.

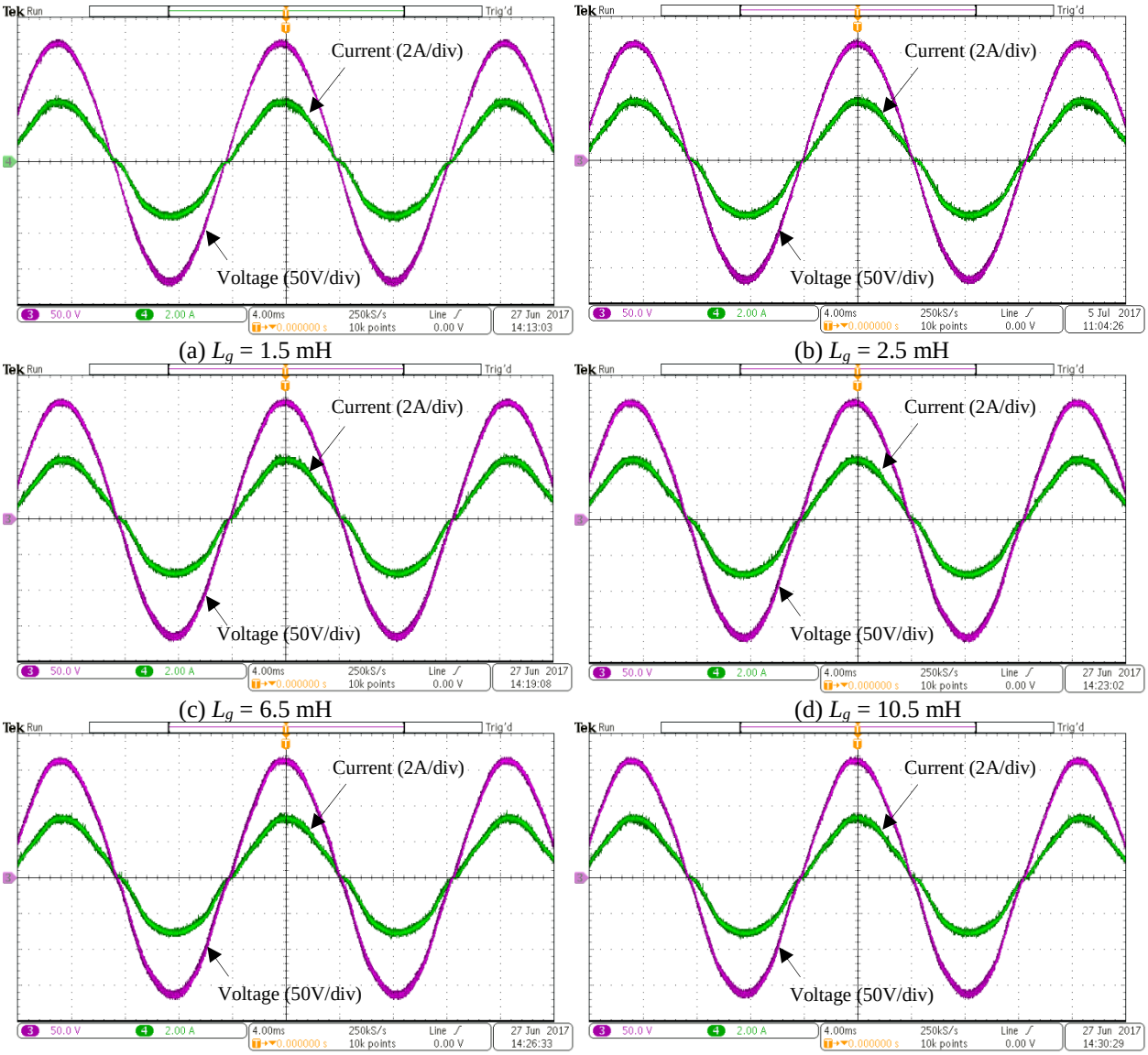

(a) L_g = 1.5 mH (b) L_g = 2.5 mH

(c) L_g = 6.5 mH (d) L_g = 10.5 mH

(e) L_g = 13.5 mH (f) L_g = 19.5 mH

Figure 2.12 Inverter output voltage and current under different grid impedances.

Table 2-2 Inverter Output Current Harmonics for an Ideal Grid

Harmonic Order	L_g = 1.5 mH	L_g = 2.5 mH	L_g = 6.5 mH	L_g = 10.5 mH	L_g = 13.5 mH	L_g = 19.5 mH
3rd	9.03%	8.29%	7.72%	7.25%	7.29%	7.75%
5th	5.03%	5.09%	5.49%	4.90%	4.67%	4.79%
7th	3.12%	3.14%	3.15%	3.22%	3.08%	3.18%
9th	1.99%	2.09%	1.95%	2.06%	2.00%	1.93%
11th	1.22%	0.99%	0.86%	0.69%	0.95%	0.83%
13th	1.18%	1.19%	0.98%	1.30%	0.96%	0.81%

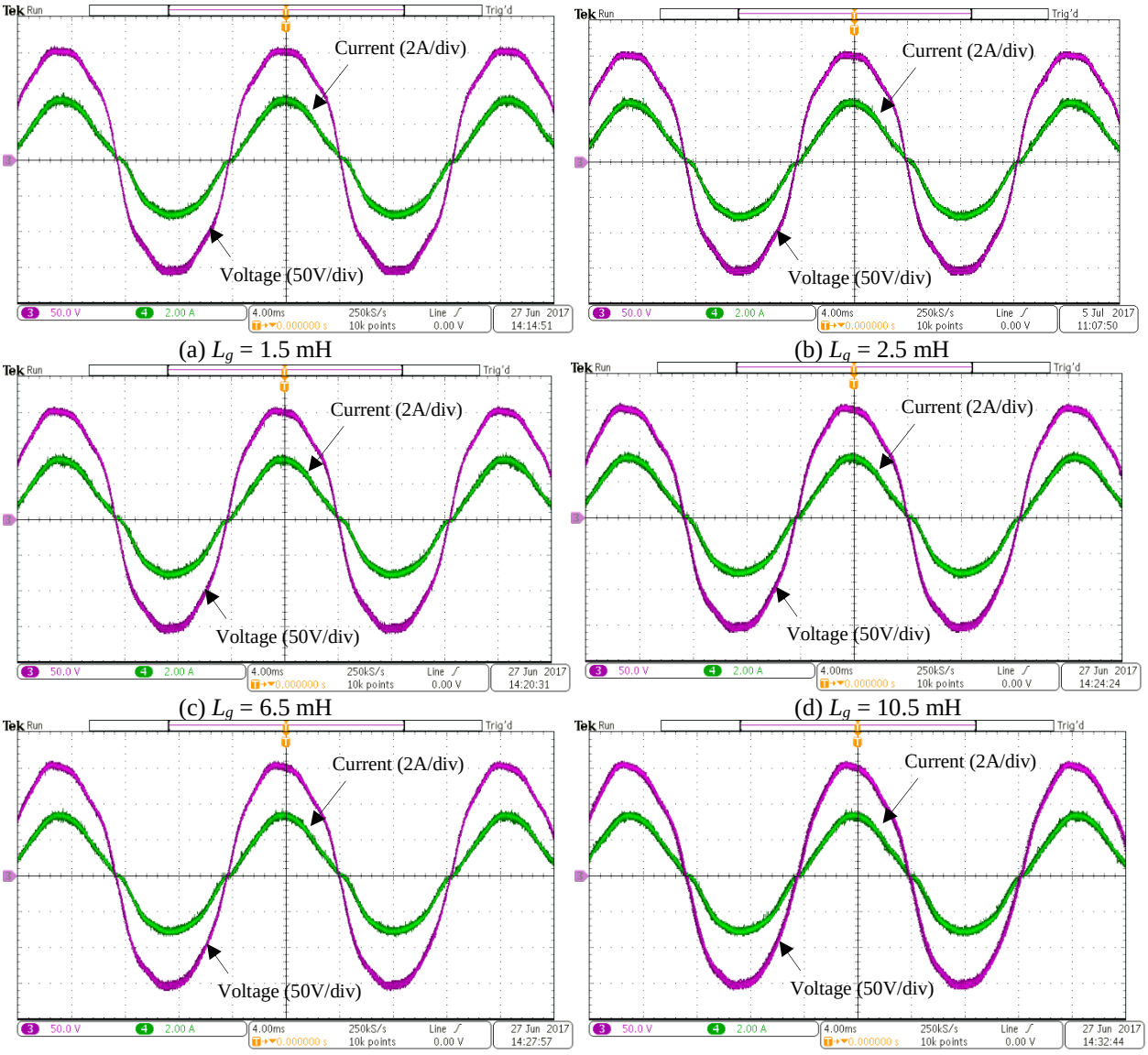

(a) L_g = 1.5 mH (b) L_g = 2.5 mH

(c) L_g = 6.5 mH (d) L_g = 10.5 mH

(e) L_g = 13.5 mH (f) L_g = 19.5 mH

Figure 2.13 Inverter output voltage and current under different grid impedances.

Table 2-3 Inverter Output Current Harmonics for a Distorted Grid

Harmonic Order	L_g = 1.5 mH	L_g = 2.5 mH	L_g = 6.5 mH	L_g = 10.5 mH	L_g = 13.5 mH	L_g = 19.5 mH
3rd	10.96%	9.88%	9.71%	9.87%	9.37%	9.43%
5th	6.53%	5.60%	6.18%	6.49%	5.65%	5.74%
7th	3.55%	3.61%	3.80%	3.43%	3.46%	3.47%
9th	1.91%	1.73%	2.06%	1.81%	1.94%	2.01%
11th	0.74%	0.74%	0.91%	0.72%	0.72%	0.82%
13th	1.14%	0.86%	0.93%	0.84%	1.08%	0.91%

CHAPTER 3 IMPEDANCE-BASED CONTROLLER DESIGN

As mentioned in the Chapter 1, the grid impedance can affect the inverter control performance and the stability of the inverter system [1,3,4,11]. The output impedance of the inverter can give an insight into the robustness and the harmonic rejection ability of the control system. Both the robustness and the harmonic rejection ability of the grid-connected inverter can be changed by shaping its output impedance [11, 57]. In this chapter, the inverter output impedance model is developed, and the relationship between the inverter output impedance and the grid impedance is investigated in the frequency domain. Through the analysis of the inverter output impedance in the frequency domain, the controller parameters can be adjusted to change the inverter output impedance so as to improve the system stability. The experimental testbed introduced in Chapter 2 is used to verify the effectiveness of the theoretical analysis.

3.1 Introduction

The inverter controller is usually designed by assuming an ideal grid, that is, a sinusoidal voltage source without any impedance. However, in the case of long distribution lines and lower power transformers, the grid can have a large impedance, which will degrade the inverter control performance [3]. Researchers have shown that the low frequency gain and bandwidth will be seriously decreased by the grid impedance [31,40].

In order to study the effect of grid impedance on the stability of the inverter system, the output impedance of the inverter can be utilized. The interaction between the grid-connected inverter and the utility grid has been studied by many researchers based on impedance analysis in the frequency domain [11, 58, 59, 60]. The stability of the system can be examined by the ratio of the grid impedance to the inverter output impedance [11]. One approach to reduce the effect of the

grid impedance is to shape the inverter output impedance correspondingly to improve the stability of the system. Therefore, the output impedance shaping based method is explored under a weak and distorted grid.

3.2 Inverter Output Impedance

3.2.1 Controller Design

PI control is commonly used in the stationary reference frame for inverter current control [19]. The inductor current of the inverter is controlled by a single-loop PI current controller. The control structure of a single-phase grid-connected inverter is presented in Figure 3.1.

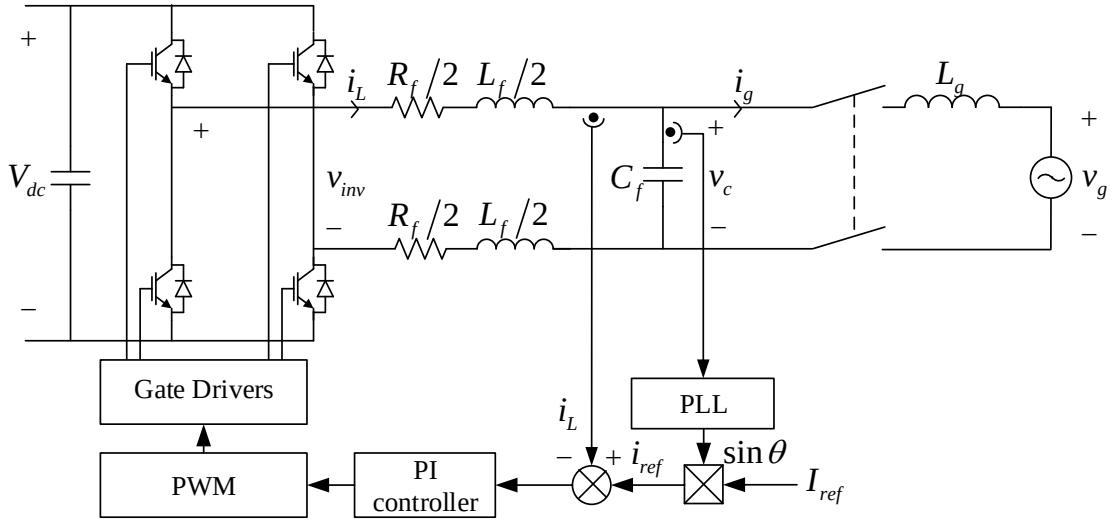

Figure 3.1 The control structure of a single-phase grid-connected inverter.

The requirement of the current controller for the system performance and stability can be specified by small steady-state error, fast dynamic response and sufficient stability margin. These specifications can be determined by the open loop gain, cutoff frequency (f_c), phase margin (PM), and gain margin (GM) of the system. Generally, f_c is designed to be 1-2 kHz for fast dynamic response, PM in the range between 30° and 60° for good dynamic response and robustness, and GM ≥ 3-6 dB for system robustness [60, 61].

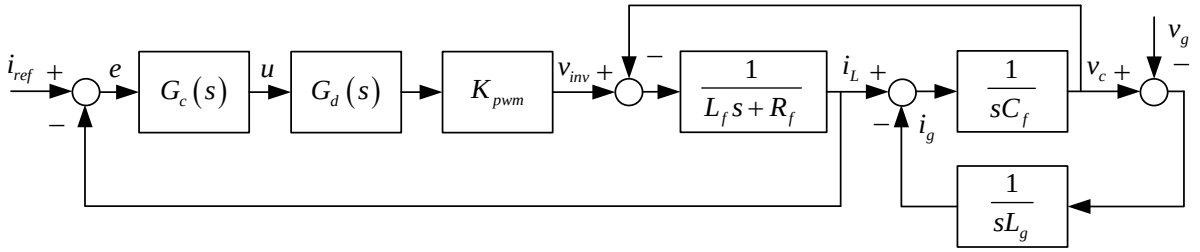

Figure 3.2 Control block diagram for a single-phase grid-connected inverter.

Figure 3.2 shows the control block diagram for the single-phase grid-connected inverter. The open loop transfer function from the current reference i_{ref} to the inductor current i_L can be expressed as:

$$G_{open1}(s) = \frac{K_{pwm} G_c(s) G_d(s)}{sL_f + R_f} \tag{3.1}$$

The transfer function of a PI controller is as follows:

$$G_c(s) = k_p + \frac{k_i}{s} \tag{3.2}$$

where k_p is the proportional gain and k_i is the integral gain. The proportional gain is usually designed to achieve unity gain at the cutoff frequency (ω_c). The magnitude of the open loop transfer function from the inductor current to the reference current at the cutoff frequency can be expressed:

$$\left|G_{open1}(s)\right| = \left|\frac{K_{pwm} G_c(s) G_d(s)}{sL_f + R_f}\right|_{s=j\omega_c} = 1 \tag{3.3}$$

Because R_f is usually small, it is ignored here. $G_c(s)$ can be approximated to k_p at the cutoff frequency [61]. Therefore,

$$k_p = \frac{1}{K_{pwm}} \left| -L_f T_d \omega_c^2 + j\omega_c L_f \right| \tag{3.4}$$

The desired phase margin can be expressed by (3.5).

$$PM = 180^\circ + \angle \frac{K_{pwm} G_c(s) G_d(s)}{sL_f + R_f}\bigg|_{s=j\omega_c} \tag{3.5}$$

The integral gain can be calculated by (3.6).

$$k_i = \frac{k_p \omega_c - k_p \omega_c^2 T_d \tan(PM)}{\omega_c T_d + \tan(PM)} \tag{3.6}$$

Since the current controller is implemented in the microcontroller, the calculated k_p and k_i must be converted to the corresponding parameters in the software. Both voltage and current are sensed by measurement circuits; therefore, the voltage sensor gain H_v and the current sensor gain H_i should be considered. The relation between the actual error signal e and the error signal in the software e' can be expressed by $e'(s) = H_i \cdot e(s)$. Similarly, the calculated voltage signal by the controller in the software u' can be converted to the actual signal in the plant u by $u(s) = u'(s)/H_v$. Therefore, the relationship between the actual current controller $G_c(s)$, shown in Figure 3.2, and the controller implemented in the software $G_c'(s)$ can be derived.

$$G_c(s) = \frac{u(s)}{e(s)} = \frac{u'(s)/H_v}{e'(s)/H_i} = G_c'(s) \cdot \frac{H_i}{H_v} \tag{3.7}$$

The cutoff frequency f_c was set about 1.7 kHz and phase margin was set to 45°. The value of the proportional gain and integral gain set in the microcontroller were k_p = 2 and k_i = 2000. The bode plot of the uncompensated system (without a current controller) and the compensated system (with current controller) are shown in Figure 3.3. The open loop gain of the compensated system at the fundamental frequency f_0 is 40 dB, which ensures that the tracking error of the inductor current is less than 1%.

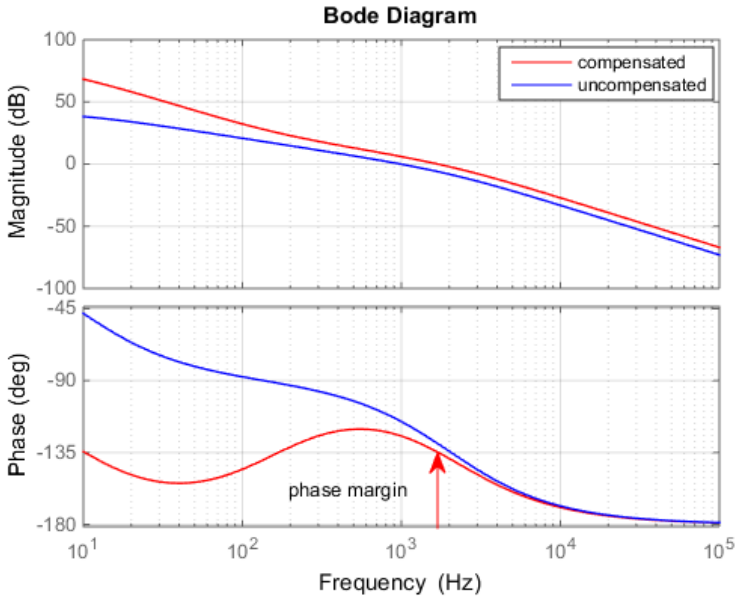

Figure 3.3 Bode plot of the compensated and uncompensated system.

3.2.2 Inverter Output Impedance

Stability analysis of a grid-connected inverter can be carried out by applying the impedance-based stability criterion. Therefore, the inverter output impedance needs to be derived first. Figure 3.2 can be simplified to Figure 3.4 by block diagram equivalent transformations.

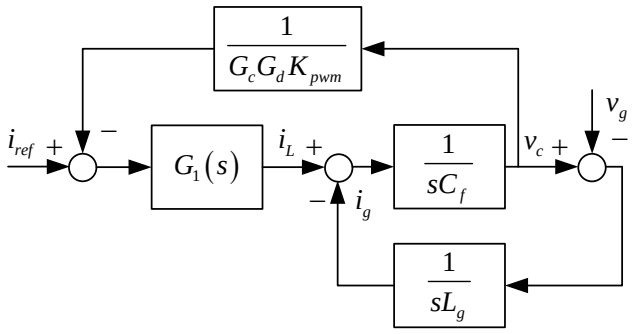

(a)

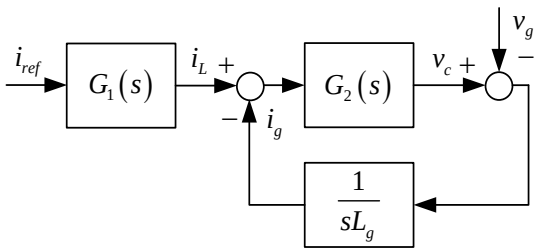

(b)

Figure 3.4 Block diagram equivalent transformation for Figure 3.2.

The resulting transfer function of $G_1(s)$ and $G_2(s)$ can be expressed by:

$$G_1(s) = \frac{K_{pwm} G_c(s) G_d(s)}{L_f s + R_f + K_{pwm} G_c(s) G_d(s)} \tag{3.8}$$

$$G_2(s) = \frac{sL_f + R_f + K_{pwm} G_c(s) G_d(s)}{s^2 L_f C_f + sC_f R_f + sC_f K_{pwm} G_c(s) G_d(s) + 1} \tag{3.9}$$

The output impedance of the inverter can be derived by:

$$Z_o(s) = \left. \frac{v_c(s)}{-i_g(s)} \right|_{i^*_{ref}=0} = \frac{sL_f + R_f + K_{pwm} G_c(s) G_d(s)}{s^2 L_f C_f + sC_f R_f + sC_f K_{pwm} G_c(s) G_d(s) + 1} \tag{3.10}$$

Therefore, the single-phase grid-connected inverter with an LC filter can be modeled by the Norton equivalent circuit shown in Figure 3.5. The inverter is represented by a current source and a parallel output impedance, and the utility grid is modeled by a voltage source and a grid impedance [11]. In this effort, only the grid inductance is considered in the analysis as a worst case scenario. In reality, the grid resistance will help to stabilize the system.

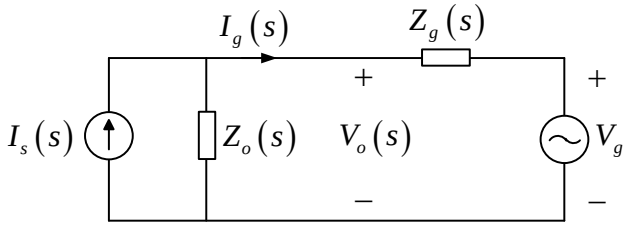

Figure 3.5 Small-signal representation of an inverter-grid system [11].

An expression for the inverter output current can be calculated by:

$$I_g(s) = \frac{I_s(s) Z_o}{Z_o + Z_g} - \frac{V_g(s)}{Z_o + Z_g} \tag{3.11}$$

$$I_g(s) = \frac{1}{1 + Z_g / Z_o} I_s(s) - \frac{1/Z_o}{1 + Z_g / Z_o} V_g(s) \tag{3.12}$$

This model is valid if the grid-connected inverter is stable when the grid impedance is zero [11]. From (3.12), it can be seen that in order to mitigate the effect caused by grid impedance variation, the inverter output impedance should be designed as high as possible to operate stably over a wide range of grid conditions [4,11]. Because the grid voltage at the PCC is often subject to background distortion at low frequency harmonics, reducing the impact of grid voltage distortion on the inverter output current can also be achieved by increasing the inverter output impedance [3]. By analyzing (3.10), it can be found that the inverter output impedance depends on the current control loop design and output filter of the inverter. Therefore, the inverter output impedance can be shaped by adjusting the controller parameters to improve the system stability.

3.2.3 Impedance Based Stability Analysis

When the inverter is connected into a utility grid, the grid impedance can influence the inverter control performance. Figure 3.6 shows the relationship between inverter output impedance and grid impedances in the frequency domain for two different grid impedances (6.5mH, 10.5mH). According to [58,59,60], the stability of the inverter depends on the phase difference between the grid impedance and the inverter output impedance at the frequency where these two impedances intersect in magnitude. The phase difference between the two impedances should be less than 180°. From Figure 3.6, with an increase in the grid impedance, the phase margin is decreasing, which implies the system is less stable.

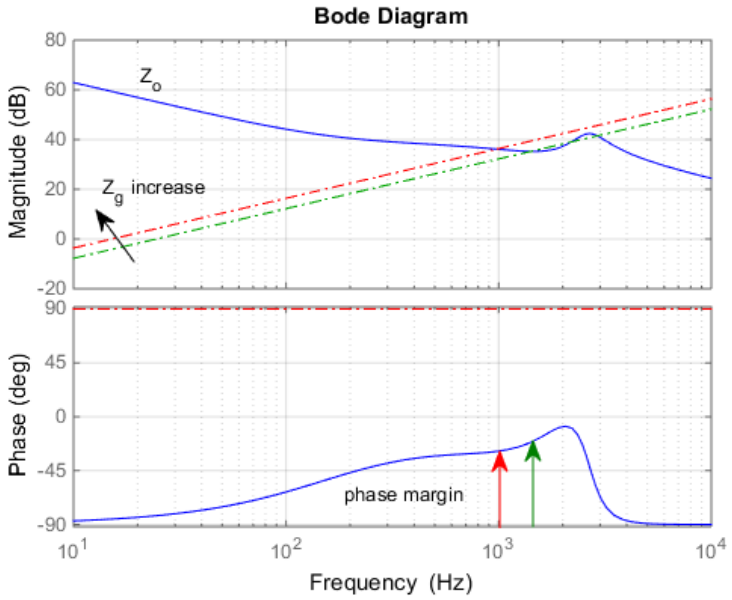

Figure 3.6 Bode plot of the inverter output impedance and different grid impedances.

In order to enhance the stability of the system under a wide range of grid impedance, the phase margin should be increased. The magnitude of the inverter output impedance also needs to be designed as high as possible to get better harmonic rejection ability. This can be achieved by selecting the current controller parameters.

3.3 Inverter Output Impedance Shaping

3.3.1 Controller Parameter Effects on Output Impedance

The controller parameters k_p and k_i are tuned to investigate their effect on the inverter output impedance. As seen in Figure 3.7, the lower frequency part of the bode diagram shows that the magnitude of the inverter output impedance increases with increasing k_p, which improves the ability for harmonic reduction. It also can be seen that the phase margin is decreasing, which means the system might become less stable.

The integral gain of the PI controller mainly affects the inverter output impedance in the low frequency part as shown in Figure 3.8. With increasing k_i, the magnitude of the output

impedance is increased while the phase margin is decreased a little. The effect of changing the integral gain k_i (200, 2000, 4000) is not as significant as the effect of changing the proportional gain k_p (1, 2, 3). Therefore, we need to combine adjusting these two parameters together to shape the inverter output impedance, while not affecting the controller performance.

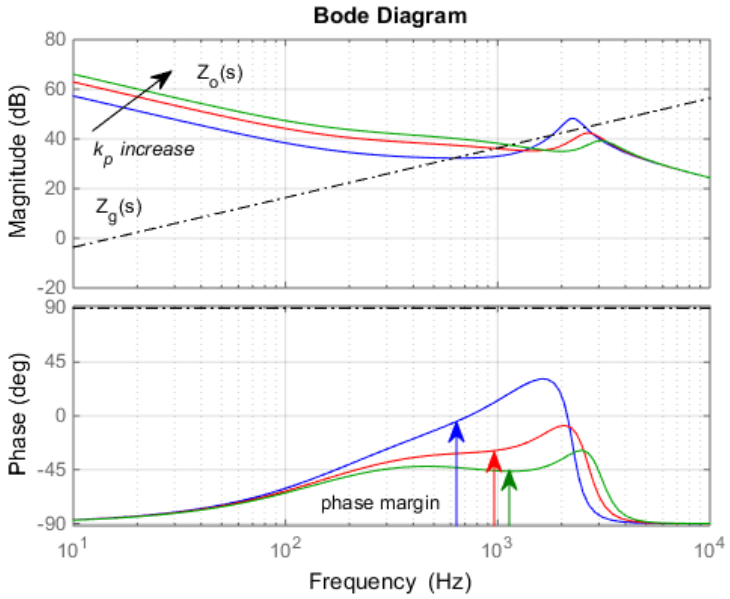

Figure 3.7 Bode plot of inverter output impedances and grid impedance (k_p changes).

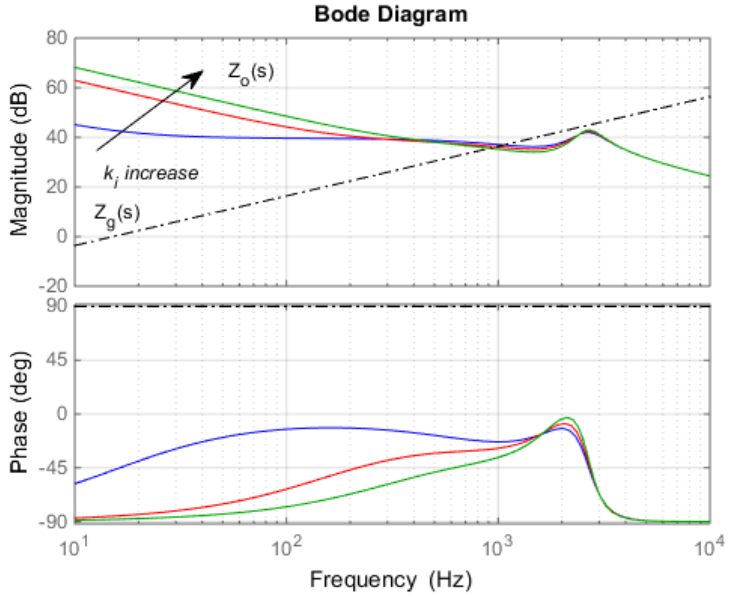

Figure 3.8 Bode plot of inverter output impedances and grid impedance (k_i changes).

3.3.2 Circuit Parameter Effects on Output Impedance

From (3.10), it can be seen that the inverter output impedance depends on the circuit parameters and controller parameters. In reality, the circuit parameters can change due to the temperature variation of the surrounding environment. Therefore, it is necessary to explore the effect of circuit parameter variations on the inverter output impedance. Since the parasitic resistance of the filter inductor has little effect on the inverter output impedance, the resistance variation is not investigated here.

From Figure 3.9, it can be seen that the frequency response of the inverter output impedance shifts to the left slightly as the inductance increases. It mainly affects the magnitude and phase of the inverter output impedance around the peak. As shown in Figure 3.10, with an increase in the filter capacitance, the magnitude of the inverter output impedance remains unchanged in the low frequency range, but it decreases in the high frequency range. The phase margin of the inverter output impedance is also decreased.

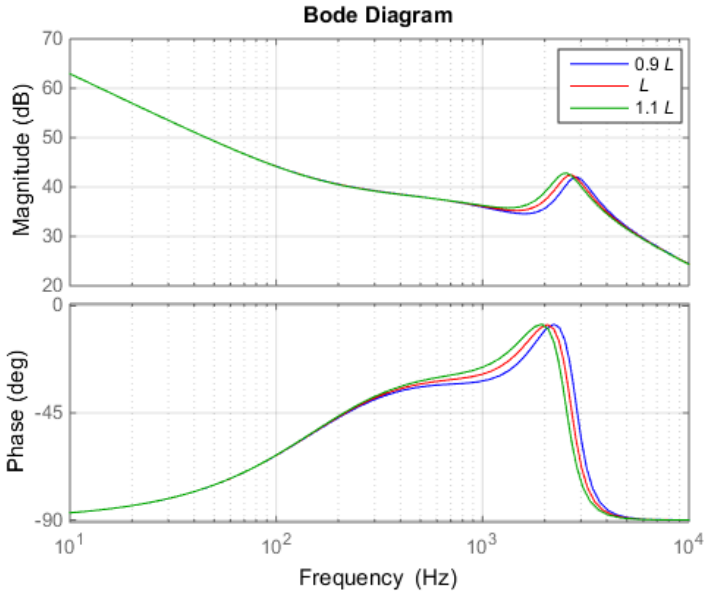

Figure 3.9 The inverter output impedance sensitivity to inductance variation.

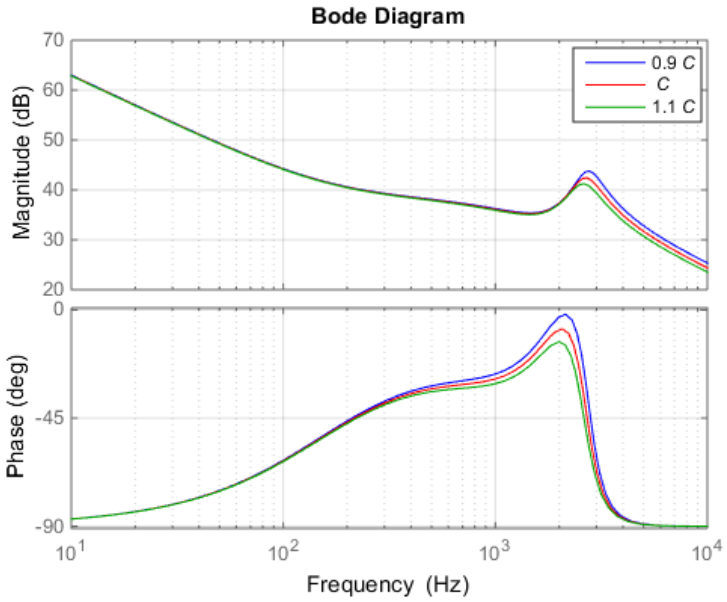

Figure 3.10 The inverter output impedance sensitivity to capacitance variation.

3.4 Simulation and Experimental Results

3.4.1 Simulation Results

The system shown in Figure 3.1 was simulated by MATLAB/Simulink to validate the theoretical analysis. The system parameters are given in Table 2-1. For the simulation, the utility grid voltage is modeled by 7% third harmonics and 5% fifth harmonics and 3% seventh harmonics with phase 30°, 90° and 270°, respectively.

Figure 3.11 and Figure 3.12 show the simulation results when the proportional gain was changed from $k_p = 2$ to $k_p = 3$ with a grid impedance of 19.5 mH. The inverter output current total harmonic distortion (THD) is 4.30% and 3.76%, respectively. The harmonic reduction ability is improved, which validates the analysis. Figure 3.13 and Figure 3.14 show the simulation results when the integral gain was changed from $k_i = 200$ to $k_i = 4000$ with the same grid impedance. The inverter output current THD is 4.83% and 4.51%, respectively. Table 3-1 and Table 3-2 show the harmonic analysis of the inverter output current.

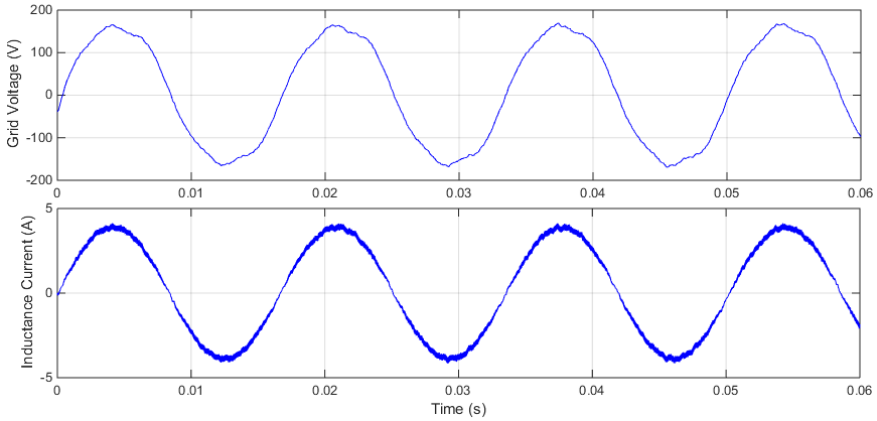

Figure 3.11 Output voltage and output current when L_g = 19.5 mH (k_p = 2).

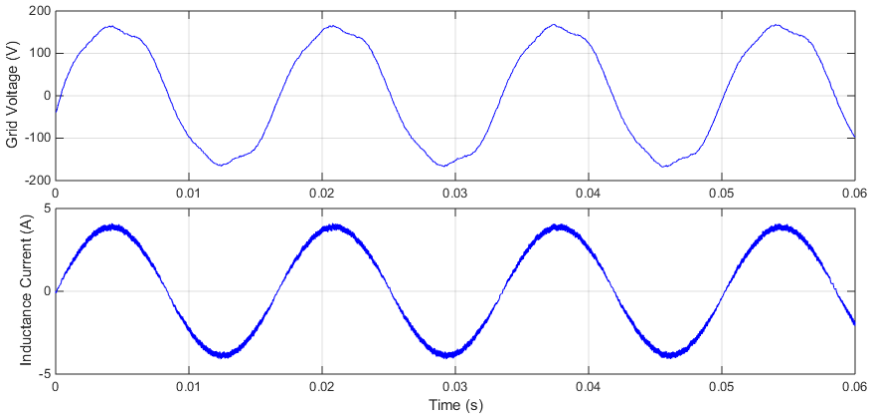

Figure 3.12 Output voltage and output current when L_g = 19.5 mH (k_p = 3).

Table 3-1 Inverter Output Current Harmonics for a Distorted Grid

Harmonic Order	L_g = 6.5 mH		L_g = 19.5 mH	
	k_p = 2	k_p = 3	k_p = 2	k_p = 3
3rd	0.71%	0.73%	1.12%	0.88%
5th	0.34%	0.42%	0.53%	0.17%
7th	0.45%	0.33%	0.53%	0.32%
9th	0.16%	0.17%	0.24%	0.25%
11th	0.13%	0.15%	0.19%	0.18%
13th	0.16%	0.10%	0.12%	0.18%
THD	3.76%	3.51%	4.30%	3.76%

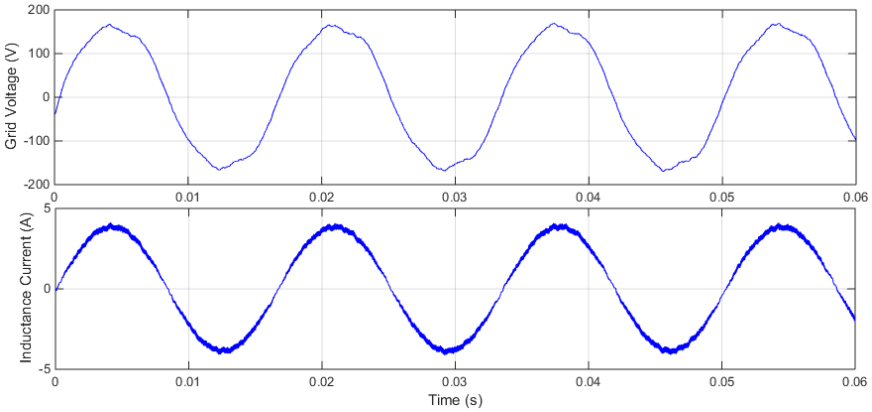

Figure 3.13 Output voltage and output current when L_g = 19.5 mH (k_i = 200).

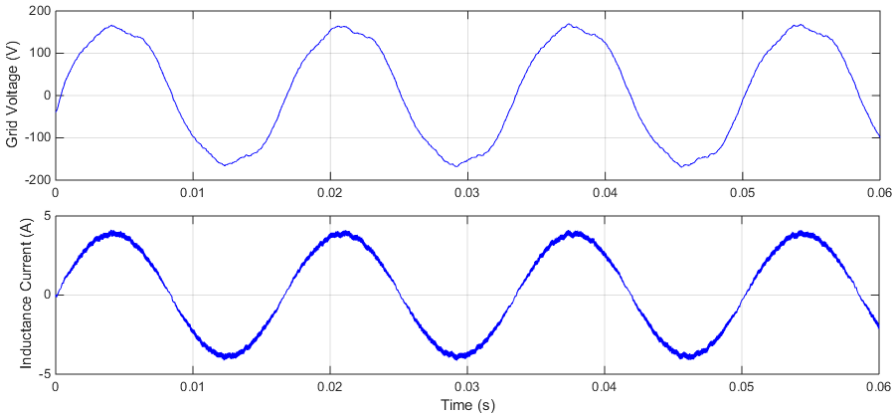

Figure 3.14 Output voltage and output current when L_g = 19.5 mH (k_i = 4000).

Table 3-2 Inverter Output Current Harmonics for a Distorted Grid

Harmonic Order	L_g = 6.5 mH		L_g = 19.5 mH	
	k_i = 200	k_i = 4000	k_i = 200	k_i = 4000
3rd	0.74%	0.52%	0.98%	0.74%
5th	0.29%	0.34%	0.49%	0.14%
7th	0.46%	0.37%	0.45%	0.28%
9th	0.25%	0.14%	0.40%	0.28%
11th	0.01%	0.05%	0.12%	0.20%
13th	0.10%	0.15%	0.04%	0.11%
THD	3.77%	3.51%	4.83%	4.51%

3.4.2 Experimental Results

The experimental testbed described in Chapter 2 was used to verify the effectiveness of the method. The measured single-phase inverter output voltage and output current are presented in Figure 3.15 - Figure 3.24. The inverter output current harmonics, measured by the Tektronix oscilloscope, are given in Table 3-3 through Table 3-6. Under the ideal grid, the THD of inverter output current was reduced from 4.94% to 4.65% by increasing the proportional gain of current controller when the grid impedance was 19.5 mH. The output voltage and output current without a PI controller was also measured for comparison to demonstrate that the current distortion can be improved by adjusting the PI controller parameters. The THD of the inverter output current was decreased from 5.09% to 4.73% by increasing the integral gain of the current controller when L_g was 19.5 mH.

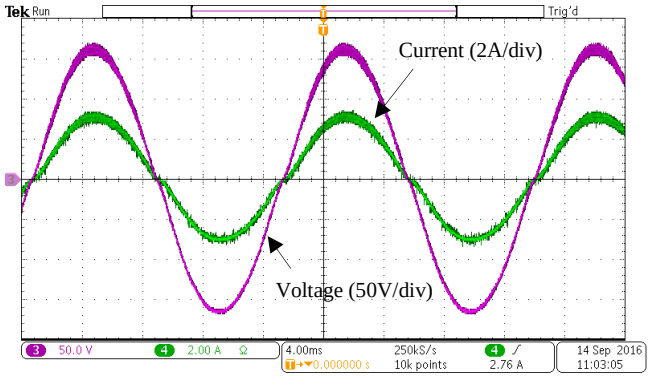

Figure 3.15 Output voltage and output current when L_g = 19.5 mH (without PI).

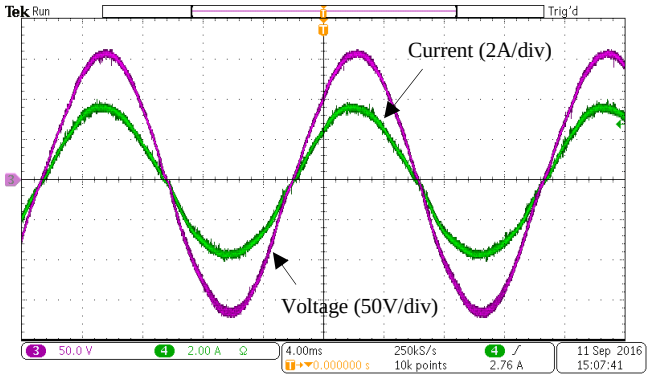

Figure 3.16 Output voltage and output current when L_g = 19.5 mH (k_p = 2).

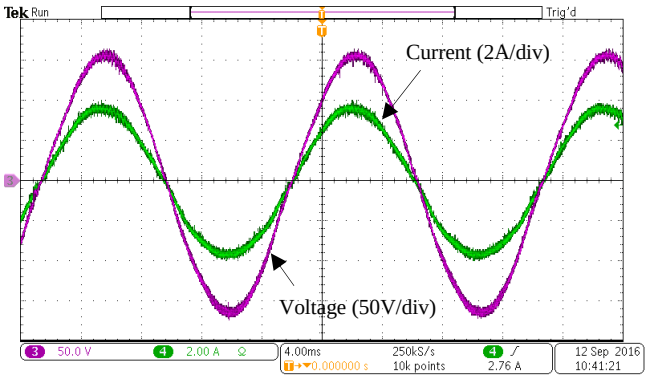

Figure 3.17 Output voltage and output current when L_g = 19.5 mH (k_p = 3).

Table 3-3 Inverter Output Current Harmonics for an Ideal Grid

Harmonic Order	L_g = 6.5 mH			L_g = 19.5 mH		
	No PI	k_p = 2	k_p = 3	No PI	k_p = 2	k_p = 3
3rd	6.87%	2.34%	1.54%	7.29%	2.70%	1.55%
5th	5.53%	1.52%	0.91%	5.71%	1.63%	0.72%
7th	2.83%	1.77%	1.37%	2.64%	1.91%	1.67%
9th	1.70%	1.97%	1.61%	1.61%	2.20%	1.61%
11th	1.09%	1.00%	0.73%	1.09%	1.18%	0.86%
13th	1.03%	0.69%	0.77%	0.89%	0.91%	0.68%
THD	6.83%	4.85%	4.64%	6.61%	4.94%	4.65%

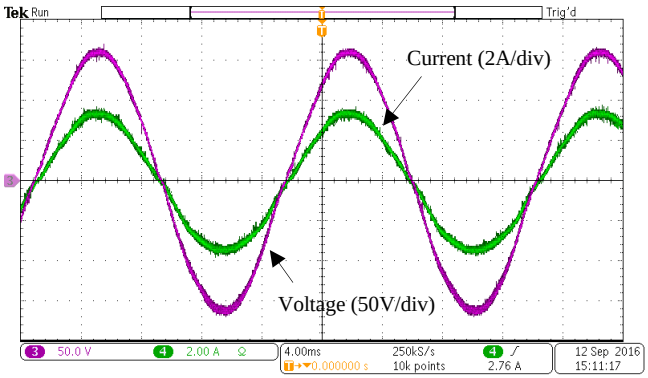

Figure 3.18 Output voltage and output current when L_g = 19.5 mH (k_i = 200).

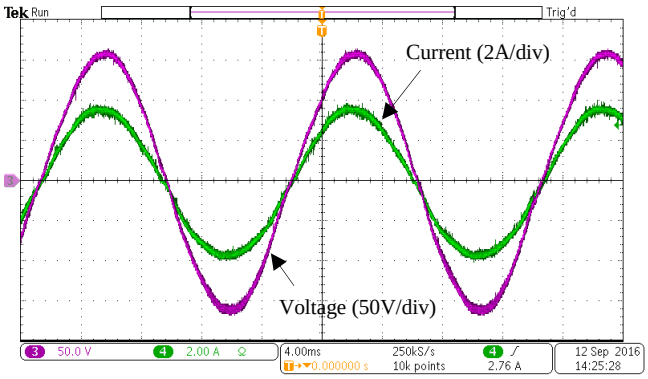

Figure 3.19 Output voltage and output current when L_g = 19.5 mH (k_i = 4000).

Table 3-4 Inverter Output Current Harmonics for an Ideal Grid

Harmonic Order	L_g = 6.5 mH		L_g = 19.5 mH	
	k_i = 200	k_i = 4000	k_i = 200	k_i = 4000
3rd	2.29%	1.82%	2.05%	2.33%
5th	1.80%	0.98%	2.01%	0.92%
7th	2.02%	1.57%	1.77%	1.54%
9th	1.96%	2.13%	1.93%	1.58%
11th	0.72%	1.31%	0.63%	0.77%
13th	0.54%	0.94%	0.40%	0.54%
THD	5.28%	4.78%	5.09%	4.73%

Under the distorted grid, the THD of inverter output current was reduced from 5.21% to 4.69% by increasing the proportional gain of current controller when the grid impedance was 19.5 mH. The THD of the inverter output current was decreased from 5.28% to 4.74% by increasing the integral gain of the current controller. As can be seen from these results, the THD of the inverter output current can be reduced by adjusting the PI controller gains. In this experimental testbed, the single-phase inverter is connected to the AC source through a 1:1 transformer and relay. The impedance of the transformer and relay were not accounted for in the modeling, which might make the actual grid side impedance larger than the grid impedance (19.5 mH). As a result, the THD of

the experimental results are higher than the THD from the simulation results. But it's still in agreement with the theoretical analysis.

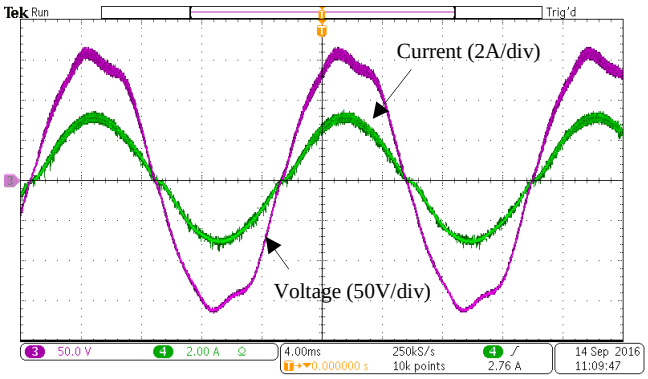

Figure 3.20 Output voltage and output current when L_g = 19.5 mH (without PI).

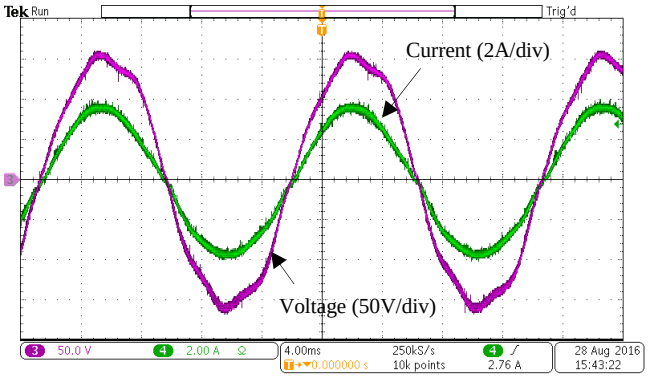

Figure 3.21 Output voltage and output current when L_g = 19.5 mH (k_p = 2).

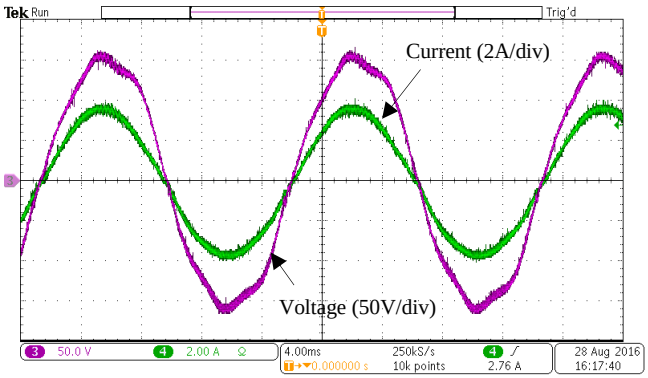

Figure 3.22 Output voltage and output current when L_g = 19.5 mH (k_p = 3).

Table 3-5 Inverter Output Current Harmonics for a Distorted Grid

Harmonic Order	L_g = 6.5 mH			L_g = 19.5 mH		
	No PI	k_p = 2	k_p = 3	No PI	k_p = 2	k_p = 3
3rd	7.62%	3.80%	2.71%	8.10%	3.47%	2.39%
5th	3.56%	1.68%	1.52%	4.43%	1.92%	0.76%
7th	4.51%	1.90%	1.28%	3.90%	2.02%	1.24%
9th	1.64%	1.57%	1.14%	1.61%	1.95%	1.45%
11th	1.13%	0.85%	0.55%	1.09%	1.22%	0.94%
13th	1.05%	0.92%	0.52%	1.08%	0.74%	0.74%
THD	6.91%	5.09%	4.77%	6.86%	5.21%	4.69%

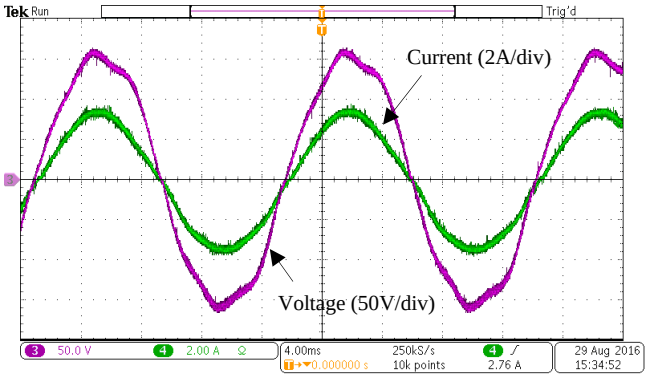

Figure 3.23 Output voltage and output current when L_g = 19.5 mH (k_i = 200).

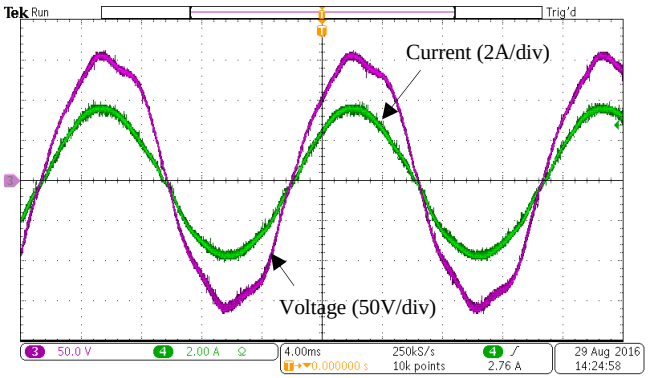

Figure 3.24 Output voltage and output current when L_g = 19.5 mH (k_i = 4000).

Table 3-6 Inverter Output Current Harmonics for a Distorted Grid

Harmonic Order	L_g = 6.5 mH		L_g = 19.5 mH	
	k_i = 200	k_i = 4000	k_i = 200	k_i = 4000
3rd	3.65%	2.78%	2.89%	2.75%
5th	1.51%	1.59%	1.06%	1.62%
7th	2.64%	1.36%	2.32%	1.59%
9th	1.67%	1.59%	1.71%	1.89%
11th	0.86%	1.06%	0.60%	0.85%
13th	0.89%	0.95%	0.58%	0.78%
THD	5.51%	4.85%	5.28%	4.74%

3.5 Conclusion

Introduced in this chapter is a method to increase the output impedance of a single-phase grid-connected inverter with an LC filter to improve the stability and harmonic reduction ability of the system when the inverter is connected to a weak distorted grid. By modeling the output impedance of the inverter, the relationship between output impedance and grid impedance can be investigated. The grid impedance can degrade the control performance of the inverter and make the system less stable. In order to mitigate this effect, PI controller parameters were adjusted to increase the output impedance, which can improve the ability for the harmonic reduction and the stability of the system. Finally, simulation and experimental results verify the effectiveness of the proposed method.

CHAPTER 4 STATE FEEDBACK CONTROLLER DESIGN

The focus of this chapter is to develop a discrete time model based state feedback control combined with a PI/PR controller for a single-phase grid-connected inverter with an LC filter operating under weak grid conditions. In distribution system, variations in the grid impedance can degrade the performance of the inverter. State feedback control offers full controllability, which can enhance stability and increase damping to reduce the LC filter resonance. By using the pole placement design, the state feedback control combined with a PI/PR controller can achieve high bandwidth and suitable stability margin. Therefore, this method has been utilized to maintain inverter performance under weak grid conditions. The impact of grid impedance variations on the closed-loop system has been analyzed. Circuit parameter sensitivity analysis is also performed to verify the robustness of this method to parameter uncertainty. Compared with conventional current feedback control (PI control, PR control), the proposed method is more robust to the grid impedance variation even under a distorted grid.

4.1 Introduction

Classical control theory is based on output feedback; however, state feedback control can give full controllability [31]. State feedback control has been used in many applications such as an uninterruptible power supply and is considered to be more comprehensive than the conventional single variable transfer function based design. The pole locations of a closed-loop system can be assigned by different approaches such as deadbeat control [27,28], linear quadratic regulator method [30] and pole placement method [32,35,36, 62]. Deadbeat control is realized by placing all the poles at the origin. It can give a fast dynamic response, but it is sensitive to measurement noise and model uncertainties. Linear quadratic regulator can offer good stability margins and

robustness [30]. This method aims to minimize a quadratic cost function. However, the need to solve the Riccati equation numerically makes this method complex. Pole placement is a direct approach, which can straightforwardly specify the closed-loop performance in terms of pole and zero locations [31].

Closed-loop performance requirements are related to the common design requirements such as damping ratio and bandwidth to define the controller's response [31,33]. The pole natural frequency can determine the system bandwidth, and the damping ratio can determine the system overshoot [33]. By proper selection of the poles of the closed-loop system using this direct approach, system stability and dynamic response can be guaranteed, and sensitivity to parameter uncertainties in the system also can be reduced.

The discrete time model developed in Chapter 2 is used for the design of the state feedback based control combined with a PI/PR controller. The proposed controller is designed based on the pole placement method to reduce the impact of grid impedance variations on the control performance. The state feedback gain and PI/PR control parameters can be determined from the circuit parameters, and the desired poles and zeros specified for system stability and dynamic performance.

4.2 State Feedback combined with PI control

4.2.1 Controller Design

Since the control is implemented digitally, the discrete state space model in (2.9) is used here for control design and performance analysis. Before designing the state feedback control, the controllability of the system needs to be checked. By calculating the controllability matrix of the discrete system given by $\begin{bmatrix} G & FG & F^2G \end{bmatrix}$, the controllability matrix is full rank, which means the system is fully controllable.

Although the state feedback control can improve the stability and introduce damping ability to reduce the resonant peak of the LC filter, only using state feedback control can yield steady state error. In order to get an accurate reference tracking, a PI controller is utilized.

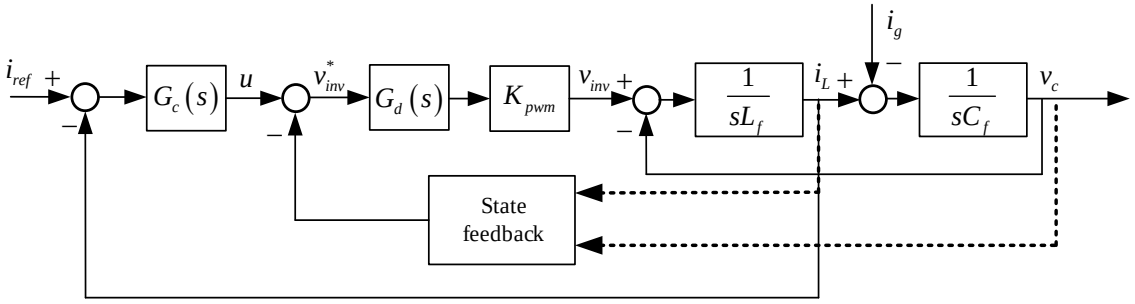

Figure 4.1 Control block diagram for a single-phase grid-connected inverter.

The discrete time PI controller is given in (4.1). The configurable zero generated by the PI controller can improve the reference tracking performance. The control structure of the system is as shown in Figure 4.1.

$$G_c(z) = k_p + \frac{k_i T_s}{1 - z^{-1}} = \frac{k_p(z - z_1)}{z - 1} \tag{4.1}$$

The control law used for state feedback is defined as:

$$v_{inv}^* = u - Kx = u - \begin{bmatrix} k_1 & k_2 & k_3 \end{bmatrix} x \tag{4.2}$$

where u is the output signal of the PI controller, and K is the state feedback gain matrix. The discrete time state space equation in (2.9) can be rearranged:

$$\begin{aligned} x[k+1] &= (F - GK)x[k] + Gu[k] + Ji_g[k] \\ y[k] &= Hx[k] \end{aligned} \tag{4.3}$$

In order to calculate the poles and zeros of the system, the transfer function of the plant system must be derived. The open loop transfer function from controller output signal to inductor current is expressed as follows:

$$G_p = \frac{i_L(z)}{u(z)} = H\left[zI - (F - GK)\right]^{-1} G = \frac{k_0(z-1)}{z^3 + a_1 z^2 + a_2 z + a_3} \tag{4.4}$$

where

$$k_0 = C_f H_i \sin(\omega_{res} T_s)/H_v$$
$$a_1 = k_3/H_v - 2\cos(\omega_{res} T_s)$$
$$a_2 = \left[C_f k_1 \omega \sin(\omega_{res} T_s) + k_2 - k_2 \cos(\omega_{res} T_s) - 2k_3 \cos(\omega_{res} T_s) + H_v\right]/H_v$$
$$a_3 = \left[-C_f k_1 \omega \sin(\omega_{res} T_s) - k_2 \cos(\omega_{res} T_s) + k_2 + k_3\right]/H_v$$

The closed-loop transfer function from the inductor reference current to the inductor current can be derived in terms of circuit parameters and control parameters. Figure 4.2 presents the block diagram of the system in discrete time.

$$G_{cl}(z) = \frac{i_L(z)}{i_{ref}(z)} = \frac{G_c(z)G_p(z)}{1 + G_c(z)G_p(z)} = \frac{k_0 k_p (z - z_1)}{z^3 + a_1 z^2 + a_2 z + a_3 + k_0 k_p (z - z_1)} \tag{4.5}$$

The closed-loop transfer function can be rewritten in pole-zero format.

$$G_{cl}(z) = \frac{k_0 k_p (z - z_1)}{(z - p_1)(z - p_2)(z - p_3)} \tag{4.6}$$

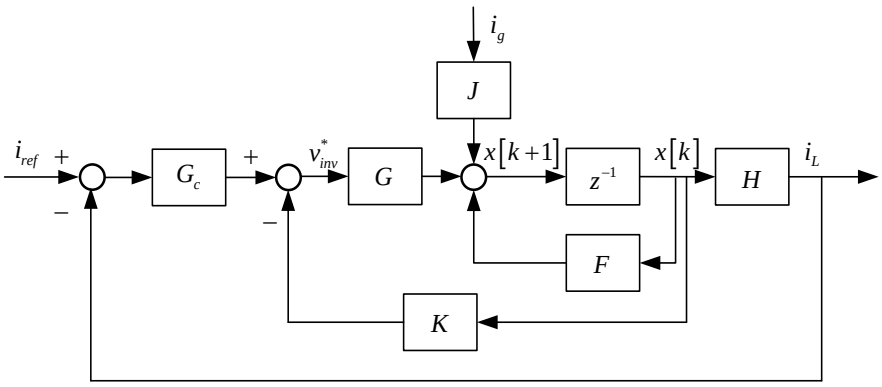

Figure 4.2 Block diagram of the system in discrete time.

Since the system is completely controllable, pole locations of the closed-loop system can be arbitrarily chosen inside the unit circle in the complex plane. The pole locations of the closed-loop characteristic equation affect the stability and the ability to reject disturbances for the system. Therefore, they should be placed at a desired location based on the control specifications.

In the open loop system, there are three poles and one zero as shown in Figure 4.3. The PI controller has a pole located at 1 on the real axis and one configurable zero. Although the closed-loop system is a fourth-order system, only three poles can be placed at desired locations. Because in the closed-loop system the one pole at 1 is canceled by the open loop zero at 1. According to the pole placement method, choose the closed-loop poles as a desired pair of dominant second-order poles. Select the rest of the poles to have real parts corresponding to sufficiently damped modes so that the system will perform as a second-order response with reasonable control effort. Therefore, choose one pole to be real and the other two poles to be a complex conjugate pair. The PI controller zero can be placed near the real pole to counteract its effect.

In general, a complex pole is characterized by its damping ratio ξ and its natural frequency ω_n [31]. They are both related to a continuous time system, and must to be mapped to the discrete time domain through $z = e^{sT_s}$. The desired discrete poles are given in (4.7) and shown in Figure 4.3 [32,33].

$$\begin{gathered} p_1 = 0.7 \quad z_1 = 1.1p_1 \\ p_{2,3} = e^{-\xi\omega_n T}\left[\cos\left(\omega_d T_s\right) \pm j\sin\left(\omega_d T_s\right)\right] \end{gathered} \tag{4.7}$$

where $\omega_d = \omega_n\sqrt{1-\xi^2}$, ξ is set to 0.7 ($0.4 < \xi < 0.7$), and ω_n is set to $0.3\pi/T_s$ ($0.2\pi/T_s < \omega_n < 0.5\pi/T_s$). The resulting control parameters and state feedback gain matrix are:

$$\begin{gathered} [k_p \quad k_i] = [1.386 \quad 7948.8] \\ K = [-0.0537 \quad -0.0011 \quad 0.0001] \end{gathered}$$

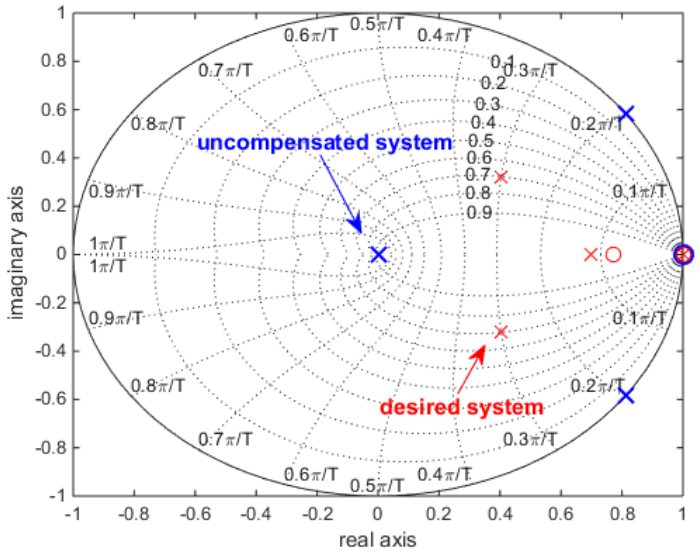

Figure 4.3 Pole and zero locations for the open loop system (blue) and desired pole and zero locations for the closed-loop system (red).

With the desired three closed-loop poles and one configurable zero, there are five unknown control parameters to be determined. Therefore, the proportional gain of the PI controller k_p is designed according to the open loop bode plot shown in Figure 4.4. With an increase of k_p, the magnitude improved greatly while the phase margin doesn't decrease much. In order to have a system with good tracking performance and stability, k_p was chosen to be 1.386. Once k_p is determined, the other four unknown control parameters can be calculated by substituting the desired poles and zeros into the closed-loop system in (4.5).

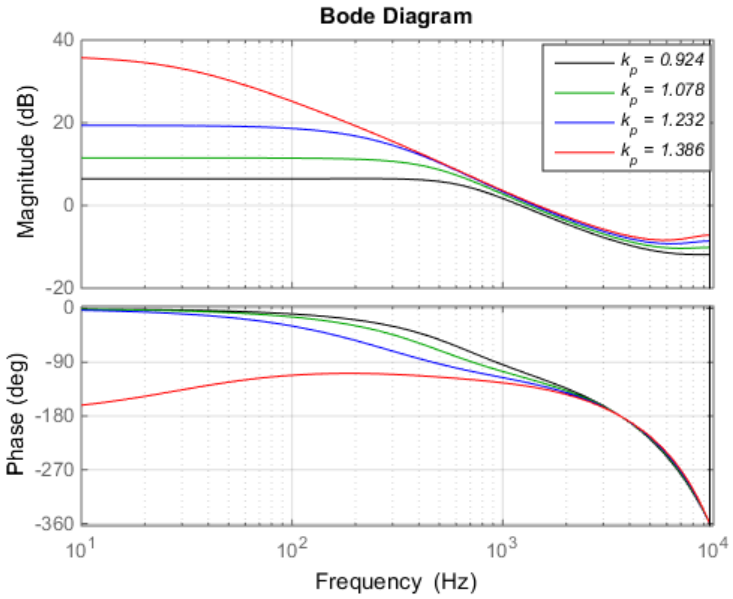

Figure 4.4 Open loop bode plot of the system.

4.2.2 Stability Analysis

The stability analysis is evaluated by the examination of the poles of the closed-loop system [32]. Variations in the grid impedance impact the locations of the poles and zeros for the proposed controller as illustrated in Figure 4.5. It can be seen that the conjugate poles tend to approach the unit circle as the grid impedance increases. Note that the system remains stable until L_g = 49 mH. In comparison, the system becomes unstable for L_g = 28 mH when utilizing only a PI controller (See Figure 4.5). Therefore, the proposed method is more stable under grid impedance variation than utilizing only a PI controller.

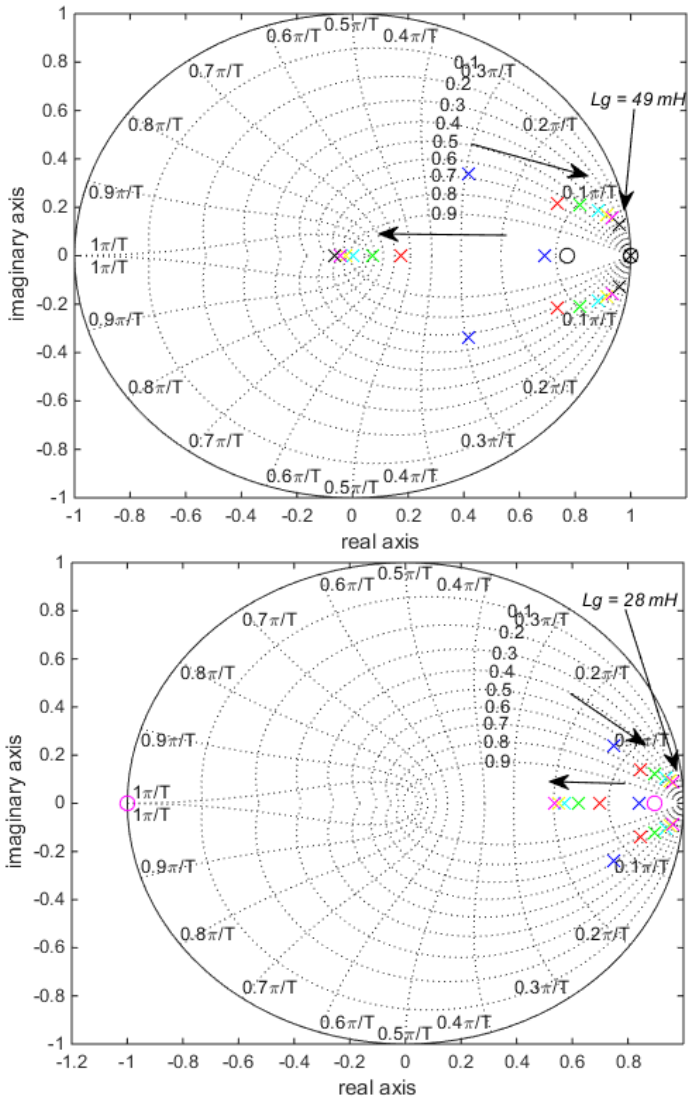

Figure 4.5 Pole and zero locations of the closed-loop system using PI + state feedback control (top) and pole and zero locations of closed-loop system using only PI control (bottom).

4.2.3 Circuit Parameter Robustness Analysis

In practice, the circuit parameters can vary from a nominal value due to environmental conditions such as temperature changes. Therefore, it is necessary to explore the effect of circuit parameter variations on the pole locations of the closed-loop system. Since the parasitic resistance of the filter inductors can improve damping into the system which can increase the stability, the resistance variation is not investigated here.

The robustness of the controller to the inductance variation was evaluated from $0.8L_f$ to $1.2L_f$. It is shown in Figure 4.6 that the closed-loop poles move toward to the unit circle as the inductance increases. Variation of the capacitance from $0.8C_f$ to $1.2C_f$ was also investigated. As indicated in Figure 4.7, capacitance variations have similar effect to the inductance variations shown in Figure 4.6 as the poles approach the unit circle.

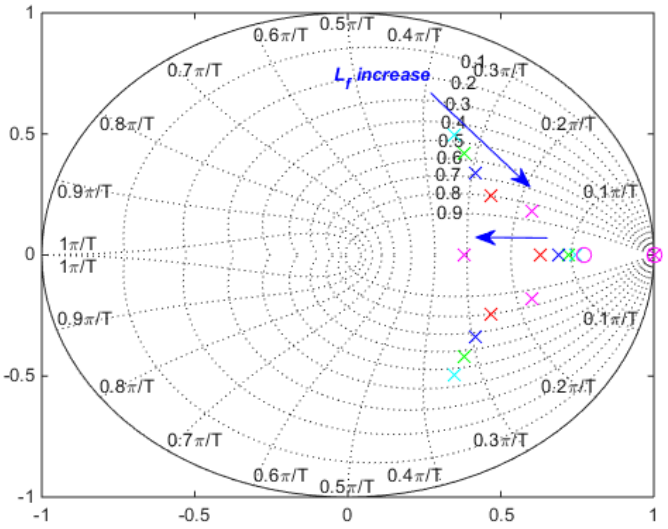

Figure 4.6 Poles and zeros of the closed-loop system when L_f changes from $0.8L_f$ to $1.2L_f$.

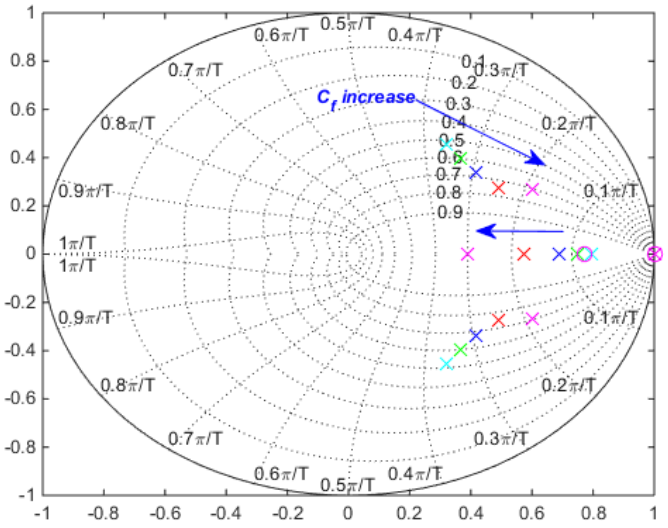

Figure 4.7 Poles and zeros of the closed-loop system when C_f changes from $0.8C_f$ to $1.2C_f$.

4.2.4 Simulation Results

To verify the effectiveness of the proposed method, traditional current feedback control methods (PI control, PR control) are used for comparative analysis. Presented in Figure 4.8 is the simulation results for the inductor current under an ideal grid, which is characterized by a single frequency sinusoidal voltage, when the grid impedance was 13.5 mH. For PI control only, the inductor current total harmonic distortion (THD) was 3.91%. For PR control, the inductor current THD was 3.68%. The current THD was reduced to 3.38% when the PI controller was augmented with state feedback control.

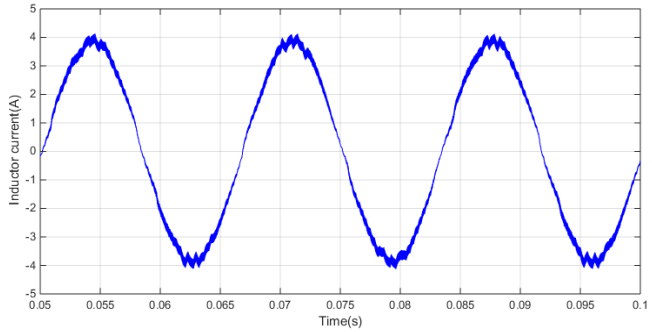

(a) PI control

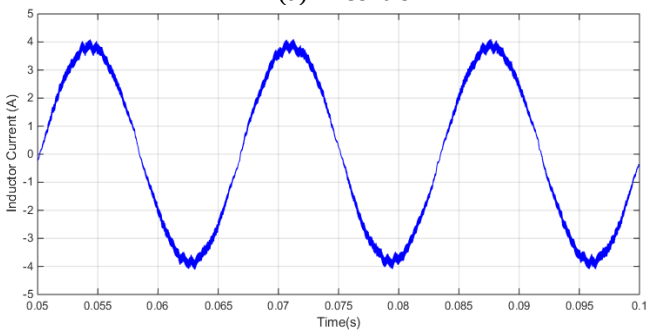

(b) PR control

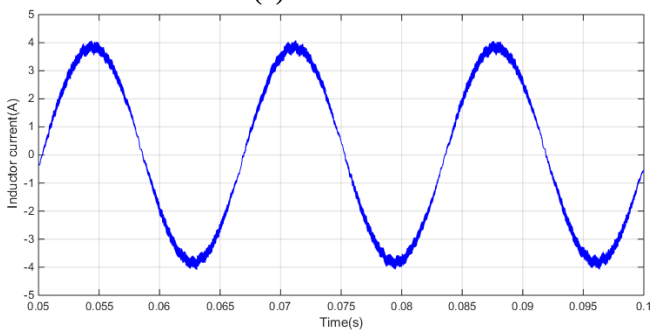

(c) PI + state feedback control

Figure 4.8 Inductor current under ideal grid (L_g=13.5 mH).

The utility grid voltage typically contains harmonics. The impact of grid voltage harmonics was investigated through simulation. A distorted grid voltage, modeled by 10% third harmonics, 5% fifth harmonics, and 3% seventh harmonics, was implemented in the simulation. Figure 4.9 shows the simulation results for a grid impedance of 13.5 mH. The current THD was 4.51% for the PI only control and 4.07% for the PR control. When the PI controller was augmented with state feedback control, the current THD was reduced to 3.78%. These simulation results indicate that the PI + state feedback control was effective in reducing the current THD as compared to the traditional current feedback control.

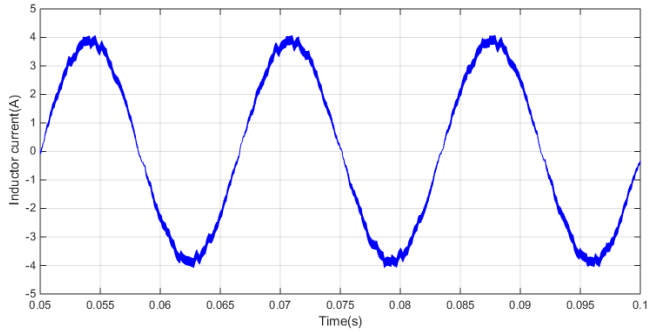

(a) PI control

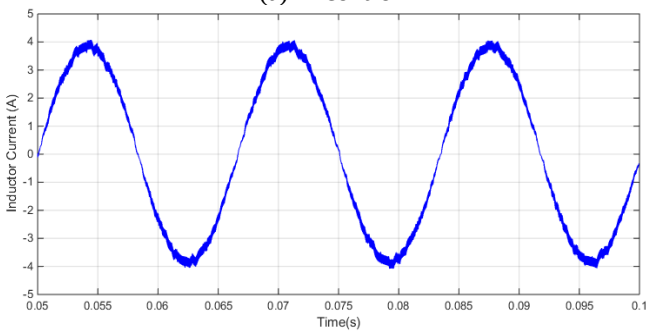

(b) PR control

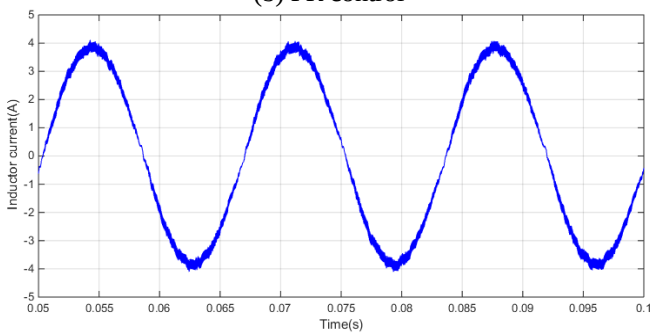

(c) PI + state feedback control

Figure 4.9 Inductor current under distorted grid (L_g=13.5 mH).

4.2.5 Experimental Results

The first comparison of the proposed method (PI + state feedback) and traditional current feedback controller is for L_g = 13.5 mH under an ideal grid voltage. The output voltage and current waveforms for this comparison are presented in Figure 4.10 - Figure 4.12. Note more distortion in the current waveform for the PI controller and PR controller. From these results, it can be determined that the PI controller and PI + state feedback controller have a small steady state error (3.6%) when following the reference current, while the PR controller can perform a more accurate reference tracking.

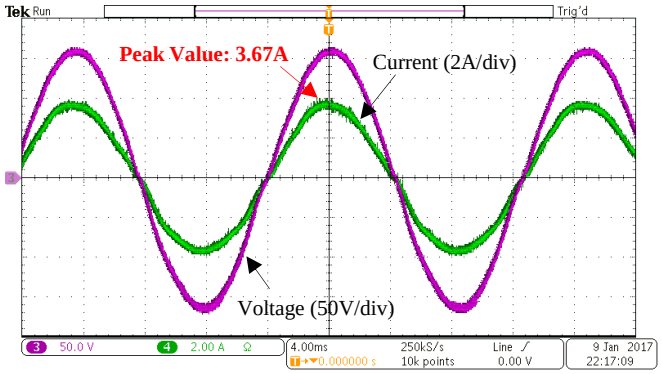

Figure 4.10 Output voltage and current using PI control under ideal grid.

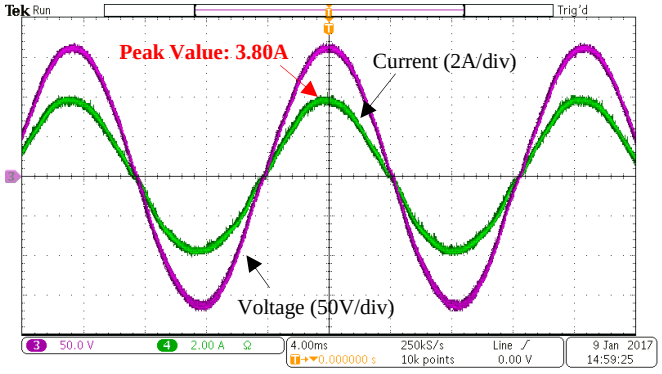

Figure 4.11 Output voltage and current using PR control under ideal grid.

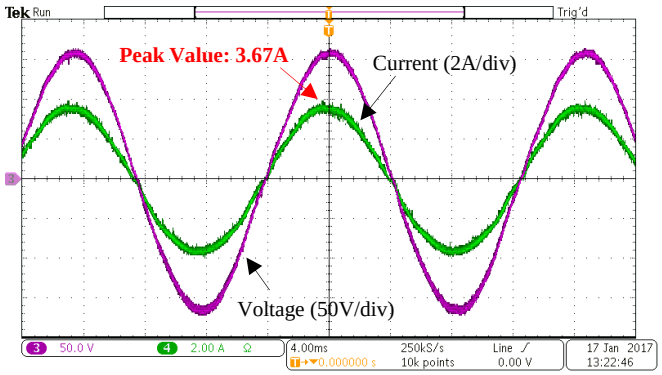

Figure 4.12 Output voltage and current using PI + state feedback control under ideal grid.

The second comparison of the control approaches is for a distorted grid voltage. Presented in Figure 4.13 - Figure 4.15 are the waveforms of the output voltage and current. Based on a close examination of the current waveforms, it appears that the PI + state feedback controller yields a less-distorted waveform.

A harmonic analysis of the inverter output current waveforms was conducted using software on the oscilloscope. The odd order harmonics of the inverter output current under ideal grid and distorted grid are presented in Table 4-1 and Table 4-2. For the ideal grid case, the magnitude of the harmonics with the proposed controller was reduced significantly. For operation with the distorted grid, the magnitude of the third harmonic was reduced by a factor of 2 using the PI + state feedback controller. These results indicate that the PI controller with state feedback performs better than the traditional current feedback controller.

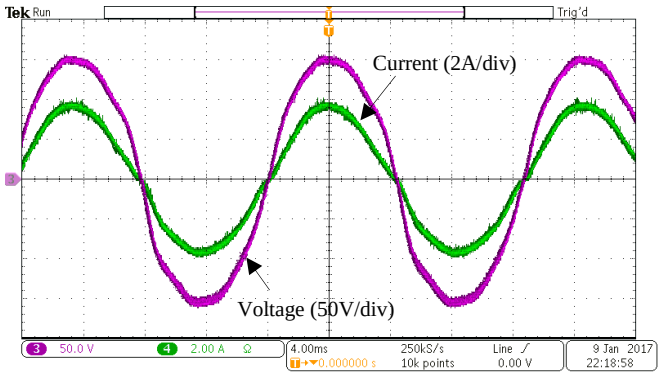

Figure 4.13 Output voltage and current using PI control under distorted grid.

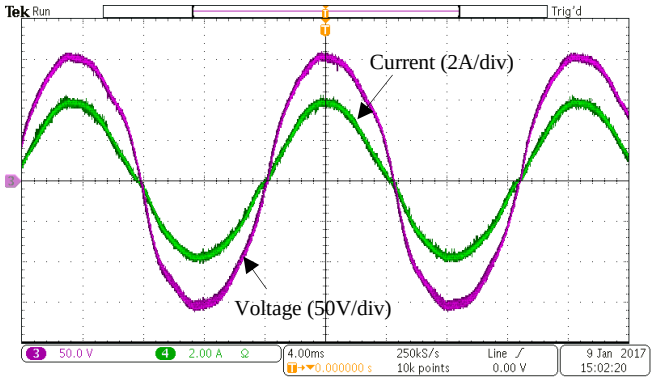

Figure 4.14 Output voltage and current using PR control under distorted grid.

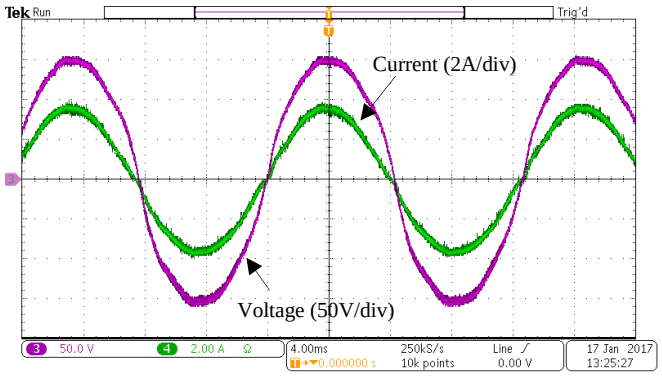

Figure 4.15 Output voltage and current using PI + state feedback control under distorted grid.

Table 4-1 Inverter Output Current Harmonics Under Ideal Grid

Harmonic Order	PI	PR	PI + State feedback
3rd	4.08%	4.25%	1.61%
5th	2.12%	2.24%	0.71%
7th	2.17%	2.23%	1.40%
9th	2.79%	2.49%	1.73%
11th	1.52%	1.00%	1.06%
13th	0.90%	0.72%	1.18%

Table 4-2 Inverter Output Current Harmonics Under Distorted Grid

Harmonic Order	PI	PR	PI + State feedback
3rd	5.67%	5.47%	2.34%
5th	3.56%	3.59%	1.10%
7th	2.75%	2.32%	1.96%
9th	2.38%	2.03%	1.55%
11th	1.59%	1.32%	1.23%
13th	1.10%	0.94%	1.39%

The system sensitivity against grid frequency variation using the proposed control method was also performed when the grid impedance was set at 13.5 mH. Figure 4.16 and Figure 4.17 show the system output voltage and current when the grid voltage frequency is below and above 60 Hz, respectively. The inverter output current harmonics are analyzed in Table 4-3. It can be seen that the current harmonics are much lower when the grid frequency is below 60 Hz. The current harmonics are very similar to normal frequency operation (60 Hz) when the grid frequency is above 60 Hz. Therefore, it can be concluded that the system has robustness to grid frequency variation under a weak grid.

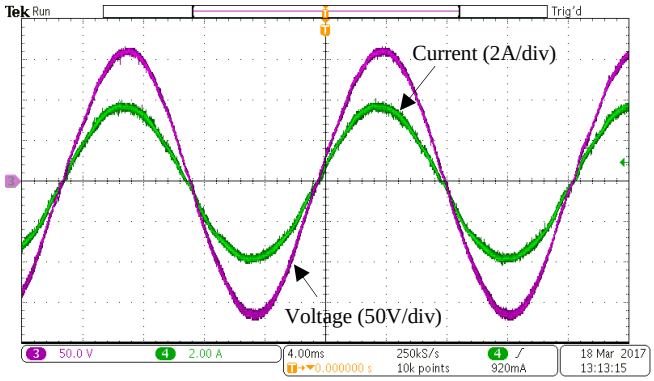

Figure 4.16 Output voltage and current when grid voltage frequency is 59.5 Hz.

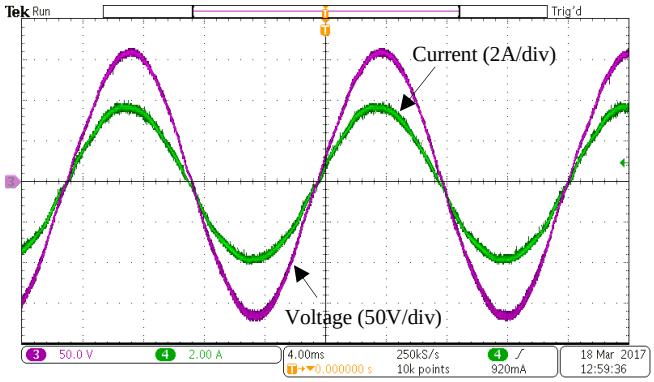

Figure 4.17 Output voltage and current when grid voltage frequency is 60.5 Hz.

Table 4-3 Inverter Output Current Harmonics Under Frequency Variation

Harmonic Order	59 Hz	59.5 Hz	60.5 Hz	61 Hz
3rd	1.28%	1.24%	1.64%	1.70%
5th	0.87%	0.61%	0.57%	0.57%
7th	1.27%	1.33%	1.26%	1.57%
9th	1.92%	1.98%	1.59%	1.77%
11th	0.79%	1.11%	1.12%	1.48%
13th	0.41%	0.85%	0.99%	1.14%

4.3 State Feedback combined with PR control

As previous section shows, the state feedback control combined with a PI controller still has a small steady state error. In order to obtain zero steady state error, a PR controller was used instead. It can produce an infinite gain at the specified frequency, which can guarantee tracking the reference current without steady state error.

4.3.1 Controller Design

A continuous time practical transfer function of a PR controller is shown in (4.8) [15].

$$G_{PR}(s) = k_p + \frac{2k_r\omega_c s}{s^2 + 2\omega_c s + \omega_0^2} \tag{4.8}$$

where k_p is the proportional gain, k_r is the resonant gain, ω_c is the cutoff bandwidth, and ω_0 is the fundamental frequency. The proportional gain k_p determines the bandwidth and stability phase margin. As ω_c gets smaller, the controller becomes more selective, as shown in Figure 4.18.

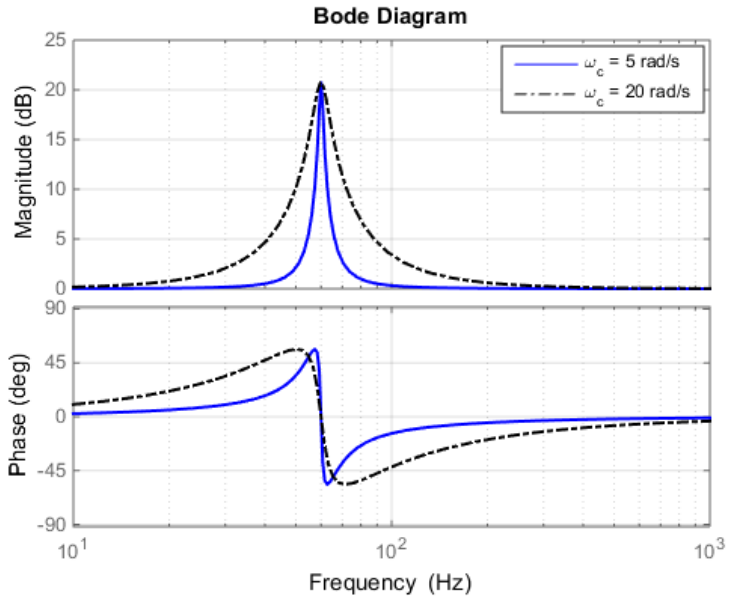

Figure 4.18 Bode plot of a practical PR controller (k_p = 1, k_r = 10).

A small ω_c will make the controller sensitive to frequency variations and lead to slow transient response, while a large ω_c will introduce a phase lag and thus decrease the phase margin. An ω_c of 5-15 rad/s is usually chosen as a compromise [67]. In practice, the fundamental frequency of the grid is allowed to vary within a narrow range, typically between 59.5 and 60.5 Hz. The corresponding frequency fluctuation is Δf = 1 Hz. In this work, $\omega_c = 2\pi\Delta f$ = 6.28 rad/s is set for frequency variation. The discrete time PR controller can be obtained by using the bilinear transformation.

$$G_{PR}(z) = \frac{b_0 + b_1 z^{-1} + b_2 z^{-2}}{1 + a_1 z^{-1} + a_2 z^{-2}} \tag{4.9}$$

where

$$b_0 = k_p + \frac{4k_r\omega_c f_s}{\omega_0^2 + 4\omega_c f_s + 4f_s^2} \quad b_1 = \frac{2k_p\omega_0^2 - 8k_p f_s^2}{\omega_0^2 + 4\omega_c f_s + 4f_s^2} \quad b_2 = k_p - \frac{4k_r\omega_c f_s + 8k_p\omega_c f_s}{\omega_0^2 + 4\omega_c f_s + 4f_s^2}$$

$$a_1 = \frac{2\omega_0^2 - 8f_s^2}{\omega_0^2 + 4\omega_c f_s + 4f_s^2} \quad a_2 = \frac{\omega_0^2 - 4\omega_c f_s + 4f_s^2}{\omega_0^2 + 4\omega_c f_s + 4f_s^2}$$

The state space control is:

$$v_{inv}^{*} = u - Kx = u - \begin{bmatrix} k_1 & k_2 & k_3 \end{bmatrix} x \tag{4.10}$$

where u is the output of the PR controller, and K is the state feedback gain. The discrete time state space equation can be rearranged:

$$\begin{aligned} x[k+1] &= (F - GK)x[k] + Gu[k] + Ji_g[k] \\ y[k] &= Hx[k] \end{aligned} \tag{4.11}$$

The open loop transfer function from controller output signal to inductor current is

$$G_p = \frac{i_L(z)}{u(z)} = H\left[zI - (F - GK)\right]^{-1} G = \frac{k_0(z-1)}{z^3 + c_1 z^2 + c_2 z + c_3} \tag{4.12}$$

where

$$k_0 = C_f H_i \sin\left(\omega_{res} T_s\right) / H_v$$
$$c_1 = k_3 / H_v - 2\cos\left(\omega_{res} T_s\right)$$
$$c_2 = \left[C_f k_1 \omega \sin\left(\omega_{res} T_s\right) + k_2 - k_2 \cos\left(\omega_{res} T_s\right) - 2k_3 \cos\left(\omega_{res} T_s\right) + H_v \right] / H_v$$
$$c_3 = \left[-C_f k_1 \omega \sin\left(\omega_{res} T_s\right) - k_2 \cos\left(\omega_{res} T_s\right) + k_2 + k_3 \right] / H_v$$

The closed-loop transfer function from the inductor reference current to the inductor current can be expressed as the following:

$$G_{cl}(z) = \frac{i_L(z)}{i_{ref}(z)} = \frac{G_c(z) G_p(z)}{1 + G_c(z) G_p(z)} = \frac{k_0 \left(b_0 z^2 + b_1 z + b_2\right)(z-1)}{\left(z^2 + a_1 z + a_2\right)\left(z^3 + c_1 z^2 + c_2 z + c_3\right) + k_0 \left(b_0 z^2 + b_1 z + b_2\right)(z-1)} \tag{4.13}$$

The closed-loop transfer function can be rewritten in pole-zero format.

$$G_{cl}(z) = \frac{k_0 b_0 (z - z_1)(z - z_2)(z-1)}{(z - p_1)(z - p_2)(z - p_3)(z - p_4)(z - p_5)} \tag{4.14}$$

The closed-loop system is a fifth-order system with three zeros and five poles. One zero is fixed by the plant and the other two zeros are generated by the PR controller and are configurable. Since the system is completely controllable, pole locations of the closed-loop system can be arbitrarily chosen inside the unit circle. Three poles should be placed at the zero locations to counteract their effects. According to the pole placement method, choose the other two poles as a desired pair of dominant second-order poles so that the system will perform as a second-order response with reasonable control effort. All poles and the zeros are related to the state feedback gain and the PR controller parameters. Therefore, the five unknown control parameters can be determined by the desired five closed-loop poles and two configurable zeros.

The pole locations are chosen to achieve typical controller parameters such as the system's closed-loop natural frequency ω_n and damping ratio ξ.

$$p_{1,2} = e^{-\xi\omega_n T_s}\left[\cos\left(\omega_d T_s\right) \pm j\sin\left(\omega_d T_s\right)\right]$$
$$p_{3,4} = z_{1,2} = 0.99 \pm j0.01726 \tag{4.15}$$
$$p_5 = z_3 = 1$$

where $\omega_d = \omega_n\sqrt{1-\xi^2}$, ξ is set to 0.7 (0.4< ξ <0.7), and ω_n is set to 0.4π/T_s (0.2π/T_s< ω_n <0.5π/T_s). The dominant poles of the controller are well damped with a damping factor of 0.7 as shown in Figure 4.19.

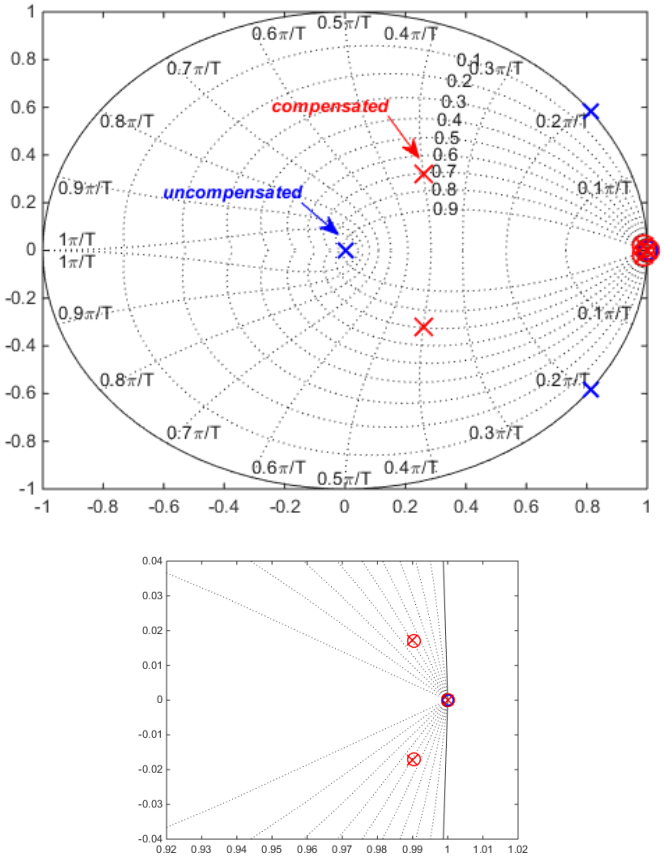

Figure 4.19 Pole and zero locations for the uncompensated system and compensated system (top) zoomed version (bottom).

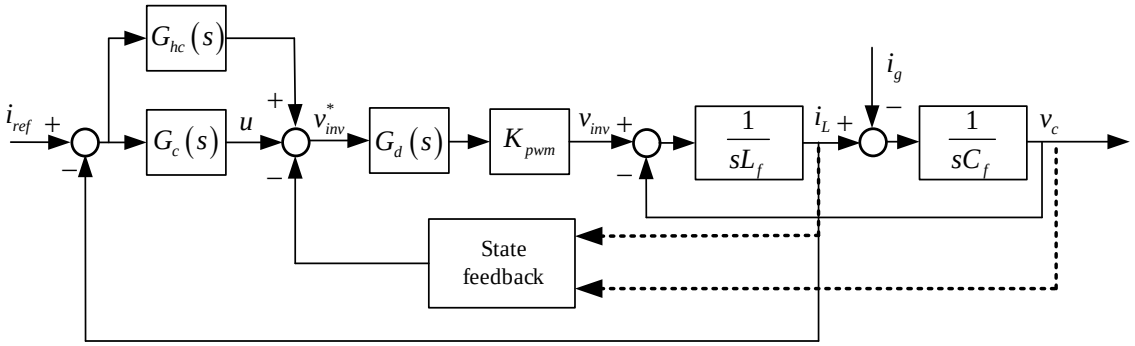

Figure 4.20 Control block diagram for a single-phase grid-connected inverter with the proposed controller.

The grid voltage usually contains low order harmonics, which can have a non-negligible effect on the grid current. In a typical current spectrum, 3rd, 5th and 7th harmonics are the most prominent harmonics [64]. To compensate for the low order harmonic frequencies, a harmonic compensator consisting of resonant controllers at selected frequencies is paralleled to the PR controller designed earlier [16, 63, 64, 65], as shown in the continuous time model of Figure 4.20.

$$G_{hc}(s) = \sum_{h=3,5,7} \frac{2k_{rh}\omega_c s}{s^2 + 2\omega_c s + \omega_h^2} \tag{4.16}$$

where h is the harmonic order, k_{rh} is the individual resonant gain and ω_h is the resonant frequency. Only 3rd, 5th and 7th order harmonics are compensated by the resonant controller, because the system might become unstable if the compensated harmonic frequency is beyond the controller bandwidth [3,17]. The harmonic compensator does not affect the dynamics of the PR controller, because it only compensates at selected frequencies [17].

The pole and zero locations of the closed-loop system with a harmonic compensator are shown in Figure 4.21. Note that it does not affect the desired closed-loop poles designed previously. Although it decreases the open loop gain in the low frequency range, the controller bandwidth and the phase margin of the system remain the same as shown in Figure 4.22.

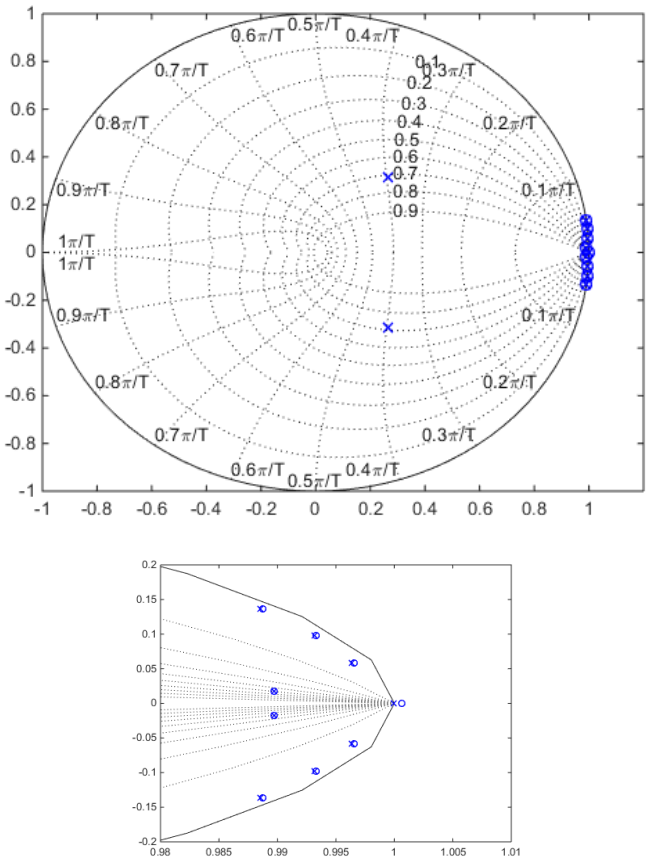

Figure 4.21 Pole and zero locations for the closed-system with a harmonic compensator (top) zoomed version (bottom).

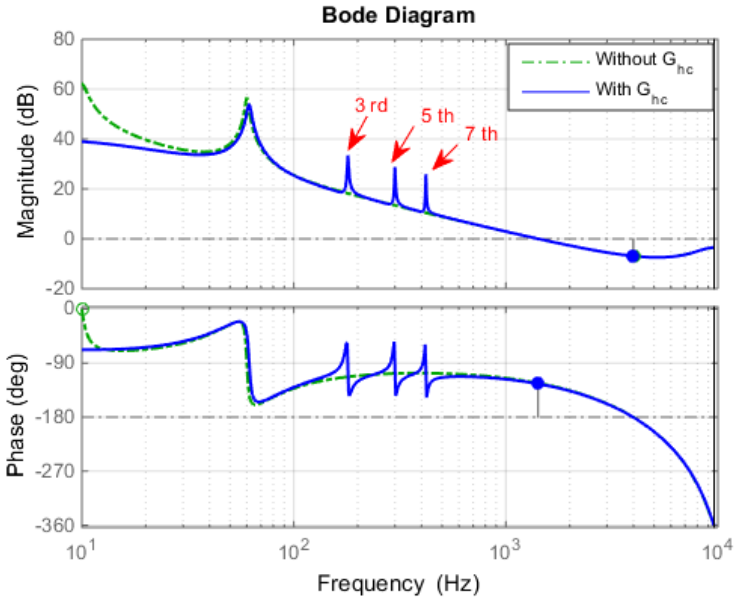

Figure 4.22 Open loop bode plot of the system without and with harmonic compensator.

4.3.2 Stability Analysis

Variations in the grid impedance impact the pole locations for the proposed controller as illustrated in Figure 4.23. It can be seen that the dominant conjugate poles tend to approach the real axis and then move towards the unit circle as the grid impedance increases from 0 to $2L_f$. The other three poles remain the same.

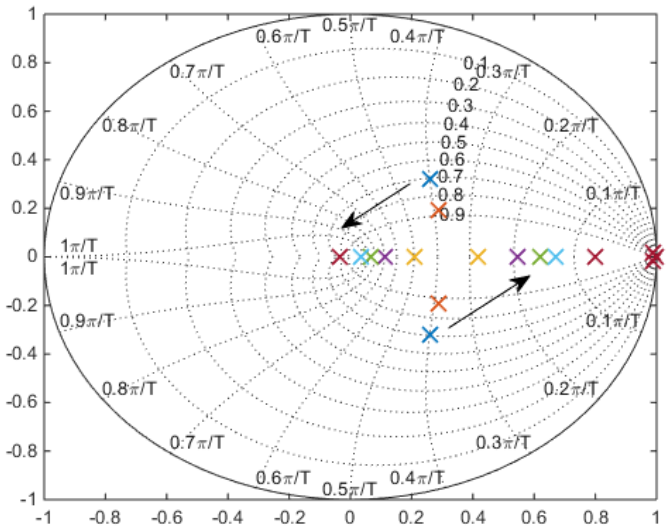

Figure 4.23 Pole locations of the closed-loop system with L_g increasing from 0 to $2L_f$.

4.3.3 Simulation Results

Two sets of comparative simulations were performed to verify the effectiveness of the proposed controller. The first comparative simulation was performed under an ideal grid, while the second utilized a distorted grid to demonstrate the effectiveness of the system's harmonic rejection ability. The ideal grid and distorted grid are the same as in a previous section. Figure 4.24 and Figure 4.25 show the results under ideal grid conditions when the grid inductance was set at 13.5 mH and 17.5 mH. Table 4-4 contains a harmonic analysis of the inductor current. Note that the magnitude of the harmonics is roughly the same for the two impedance values. The results from the second simulation with a distorted grid voltage for 13.5 mH and 17.5 mH are given in Figure 4.26 and Figure 4.27. Again, note that the magnitude of the harmonics are very similar as

illustrated in Table 4-5. Based on the data in Table 4-4 and Table 4-5, it is evident that the system is robust to grid inductance variation.

The inductor current waveforms below are very similar for all cases. In addition, the results in Table 4-4 and Table 4-5 indicate good harmonic rejection capability for the proposed controller. The harmonic compensator mitigates the impact of the harmonics in the distorted grid voltage.

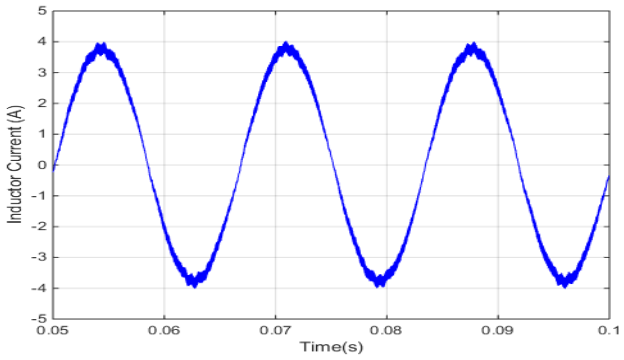

Figure 4.24 Inductor current under ideal grid (L_g = 13.5 mH).

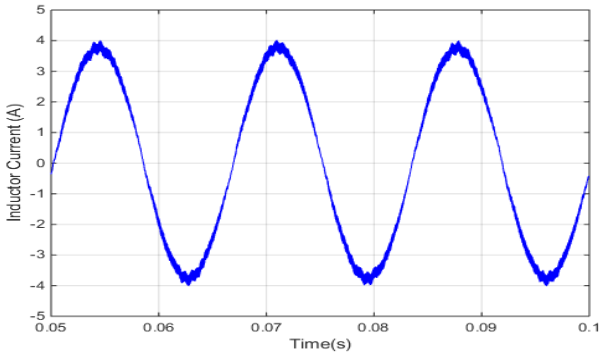

Figure 4.25 Inductor current under ideal grid (L_g = 17.5 mH).

Table 4-4 Inductor Current Harmonics Under Ideal Grid

Harmonic Order	L_g = 13.5 mH	L_g = 17.5 mH
3rd	0.46%	0.42%
5th	0.29%	0.32%
7th	0.14%	0.10%
9th	0.30%	0.21%
11th	0.07%	0.09%
13th	0.23%	0.22%

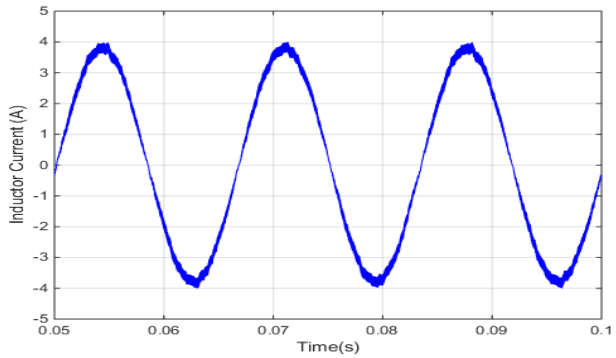

Figure 4.26 Inductor current under distorted grid (L_g = 13.5 mH).

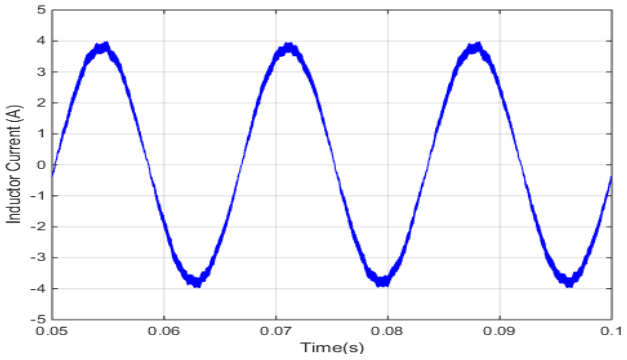

Figure 4.27 Inductor current under distorted grid (L_g = 17.5 mH).

Table 4-5 Inductor Current Harmonics Under Distorted Grid

Harmonic Order	L_g = 13.5 mH	L_g = 17.5 mH
3rd	0.57%	0.42%
5th	0.20%	0.15%
7th	0.07%	0.10%
9th	0.19%	0.22%
11th	0.13%	0.11%
13th	0.22%	0.19%

4.3.4 Experimental Results

The control algorithm was implemented on a fixed-point DSP TMS320F28M35. When implementing a PR controller on a fixed-point DSP, the effects of finite precision representation of the system coefficients and the effects of the truncation of intermediate computations should be considered [66, 67]. Generally, the control performance degrades when the shift-operator based

resonant implementation given in (4.8) is programmed in a fixed-point DSP. It's mainly caused by round-off errors [67]. However, the delta operator has the advantage of superior finite word length performance and improved rounding error performance. It is defined in (4.16).

$$\gamma = \frac{z-1}{\Delta} \Rightarrow \gamma^{-1} = z^{-1}\Delta + \gamma^{-1}z^{-1} \tag{4.16}$$

Where Δ is a time step less than 1 and usually should be designed to achieve small round-off error. The delta operator form of the PR controller can be expressed by (4.17). By substituting (4.16) into (4.8), the coefficients of the delta operator-based PR controller can be derived.

$$G_c(\gamma) = \frac{\beta_0 + \beta_1\gamma^{-1} + \beta_2\gamma^{-2}}{\alpha_0 + \alpha_1\gamma^{-1} + \alpha_2\gamma^{-2}} \tag{4.17}$$

Where $\alpha_0 = 1$, $\alpha_1 = (2 + a_1)/\Delta$, $\alpha_2 = (1 + a_1 + a_2)/\Delta^2$, $\beta_0 = b_0$, $\beta_1 = (2b_0 + b_1)/\Delta$, $\beta_2 = (b_0 + b_1 + b_2)/\Delta^2$. The implementation of the controller should use the structure of direct form II shown in Figure 4.28, because it can provide the best round-off noise performance [67]. The difference equations implemented in the DSP can be expressed by (4.18).

$$\begin{aligned} w_1[k] &= w_0[k-1]\cdot\Delta + w_1[k-1] \\ w_2[k] &= w_1[k-1]\cdot\Delta + w_2[k-1] \\ w_0[k] &= -\alpha_1 w_1[k] - \alpha_2 w_2[k] + u[k] \\ y[k] &= \beta_0 w_0[k] + \beta_1 w_1[k] + \beta_2 w_2[k] \end{aligned} \tag{4.18}$$

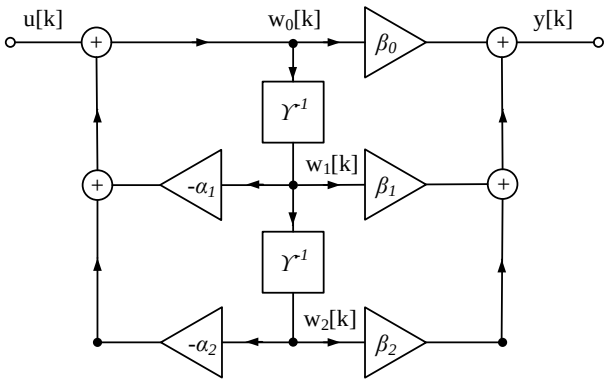

Figure 4.28 Direct Form II digital filter structure.

The experimental inverter output voltage and current waveforms under ideal grid voltage conditions are presented in Figure 4.29 and Figure 4.30 for two different grid inductance values. Note from Table 4-6 that the harmonic magnitudes are very similar. Presented in Figure 4.31 and Figure 4.32 are the experimental waveforms for the inverter output voltage and current for the distorted grid voltage. Again, note the similarity in the harmonic magnitudes for the different inductance values. With the exception of the 3rd harmonic, the other harmonic magnitudes are very similar. This is because the harmonic compensator reduces the effects of the distorted grid voltage on the output current. Examination Table 4-6 of and Table 4-7 indicate that state space current control combined with a harmonic compensator is robust to grid inductance variation.

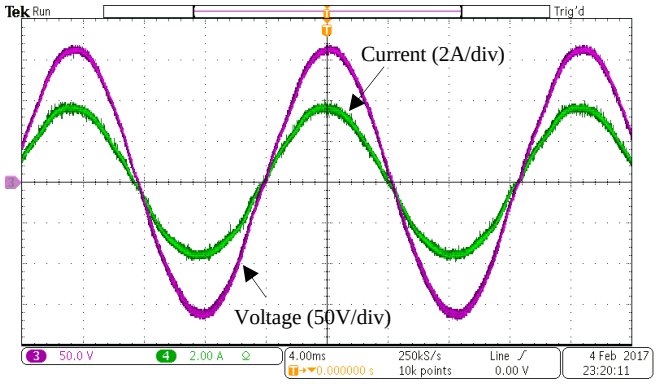

Figure 4.29 Output voltage and output current under ideal grid (L_g=13.5 mH).

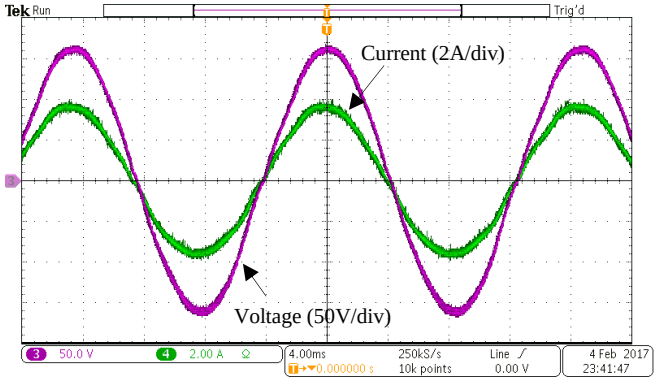

Figure 4.30 Output voltage and output current under ideal grid (L_g=17.5 mH).

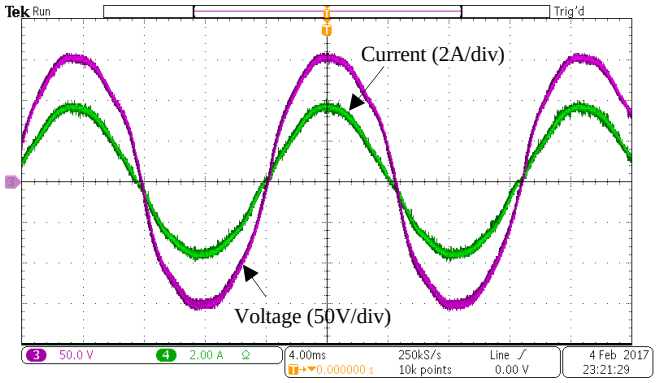

Figure 4.31 Output voltage and output current under distorted grid (L_g=13.5 mH).

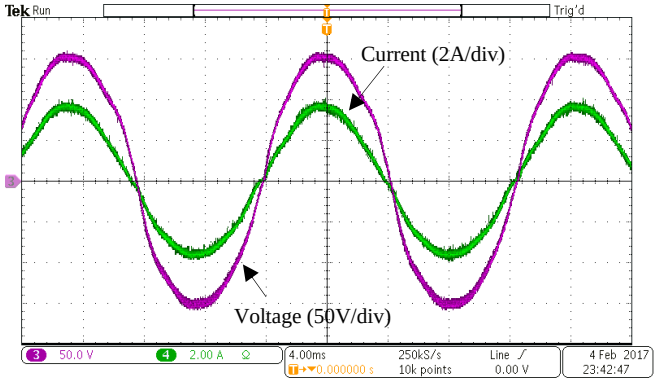

Figure 4.32 Output voltage and output current under distorted grid (L_g=17.5 mH).

Table 4-6 Inverter Output Current Harmonics Under Ideal Grid

Harmonic Order	L_g = 13.5 mH	L_g = 17.5 mH
3rd	1.36%	1.57%
5th	0.67%	0.53%
7th	0.94%	0.65%
9th	2.19%	2.26%
11th	0.69%	0.91%
13th	0.90%	0.66%

Table 4-7 Inverter Output Current Harmonics Under Distorted Grid

Harmonic Order	L_g = 13.5 mH	L_g = 17.5 mH
3rd	1.91%	1.82%
5th	0.98%	0.42%
7th	1.07%	1.02%
9th	1.94%	2.27%
11th	0.88%	1.07%
13th	0.74%	1.06%

Figure 4.33 and Figure 4.34 illustrate the dynamic performance of the system. A step change in the reference current from 2.55 A to 5.10 A occurs at the peak of the current as shown in Figure 4.33. The reference current is changed from 5.10 A to 2.55 A at the peak of the current in Figure 4.34. It can be seen that the inverter output current changes quickly with little overshoot in both cases.

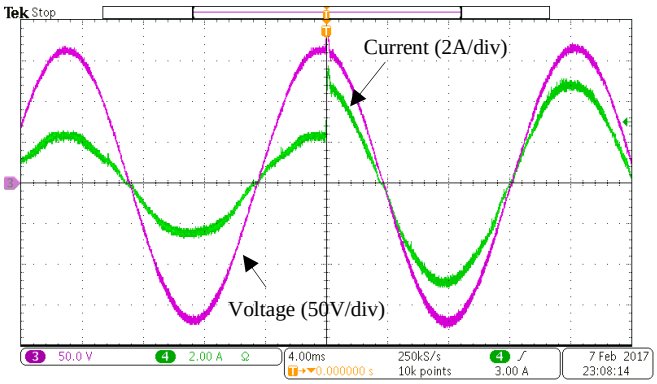

Figure 4.33 Response to an increasing step change of the reference current.

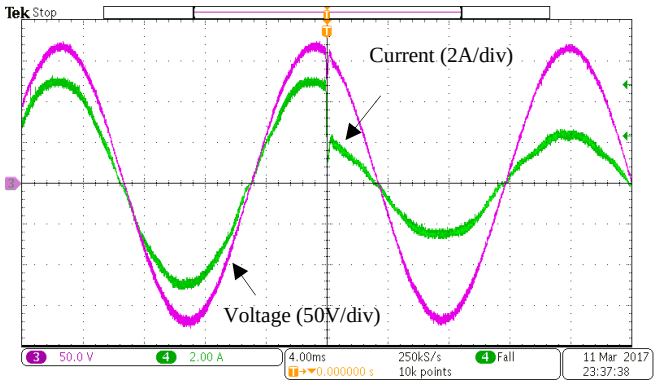

Figure 4.34 Response to a decreasing step change of the reference current.

4.4 Conclusion

The proposed state feedback control combined with a PI/PR controller for a single-phase grid-connected inverter show the robustness for a larger grid impedance than either the PI or PR only control approach. The current harmonics are also reduced by using the proposed controller as compared to utilizing only a PI or PR controller. Although the PI + state feedback control shows a small steady state error in reference tracking, it is still an effective method with robustness against grid impedance variations as well as harmonic rejection ability. Furthermore, the PR + state feedback control with a harmonic compensator can effectively suppress the low order current harmonics and show a good dynamic performance.

CHAPTER 5 GAIN SCHEDULING CONTROLLER DESIGN

As previous discussed, the grid impedance can impact the control performance of the inverter. With an increase in the grid impedance, the open loop cutoff frequency decreases, which affects the transient performance. Also, the phase margin of the system decreases, which deteriorates the system stability. In order to address this problem, a detection of the grid impedance and an adjustment of control parameters are needed because of the grid impedance impact on the system bandwidth and stability [3,17]. In this chapter, a gain scheduling control strategy based on grid impedance estimation is used to adjust the controller parameters so as to make the system robust to grid impedance variations. The grid impedance effect on the current controller performance is analyzed. In order to mitigate its effect, an optimal gain is derived based on the desired controller bandwidth and phase margin of the system. It has been demonstrated that this adaptive controller can maintain the controller bandwidth and phase margin at satisfactory levels in the presence of a grid impedance.

5.1 Introduction

For the grid-connected inverter, a proportional integral (PI) controller is often used for current control to achieve a sinusoidal grid current with unity power factor. The high bandwidth of the controller is required to guarantee accurate reference tracking and good transient performance. A sufficient stability margin is also necessary to make the system stable. As the grid-connected inverters are often installed at the distribution level, the grid impedance can be large. Moreover, due to the continuous variation of loads, the grid impedance can vary widely. As a result, it can impact the control performance of the inverter. Variations in the grid impedance can not only decrease the bandwidth and loop gain, but also cause a negative impact on the phase

margin of the system, which will degrade the stability of the grid-connected inverter. Generally, in practice, the grid impedance value is unknown; therefore, it is hard to design a controller robust to grid impedance variations. Although a large proportional gain can compensate for the effect of a weak grid, it generally deteriorates the system stability [24].

Adaptive control methods such as model reference adaptive control [37] and gain scheduling control [38,39] have been utilized to tune the controller parameters to improve the controller performance when the grid impedance is unknown. Model reference adaptive control adjusts the controller parameters based on the difference between the output of the system and the output of a reference model, but it has the possibility of making the system unstable. The gain scheduling method is a more conservative adaptive control method, which can ensure system stability while adapting. To improve the bandwidth and phase margin of the controller, the gain scheduling method is adopted to adjust the controller parameters.

5.2 Controller Design

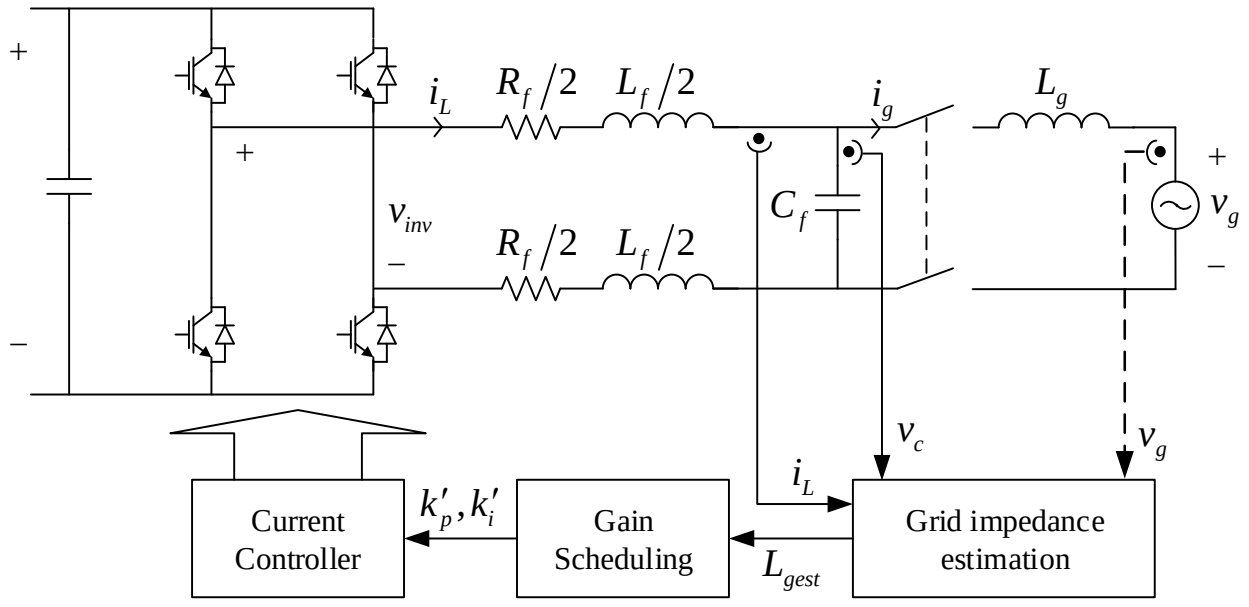

Figure 5.1 Single-phase grid-connected inverter using gain scheduling control.

Figure 5.1 shows the diagram of the single-phase grid-connected inverter using gain scheduling control. The control block diagram for this single-phase grid-connected inverter is presented in Figure 5.2. The open loop transfer function from the current reference i_{ref} to the inductor current i_L derived in (3.1) is rewritten below:

$$G_{open1}(s) = \frac{K_{pwm} G_c(s) G_d(s)}{sL_f + R_f} \tag{5.1}$$

where $G_c(s)$ is the transfer function of a PI controller. In order to achieve a good transient performance, the controller cutoff frequency is set at 1 kHz and the phase margin is set at 45°. Therefore, the proportional gain and integral gain can be derived by (3.4) and (3.6), respectively. According to the circuit parameters given in Table 2-1, the proportional gain k_p is 1.0156, and the integral gain k_i is 2179.

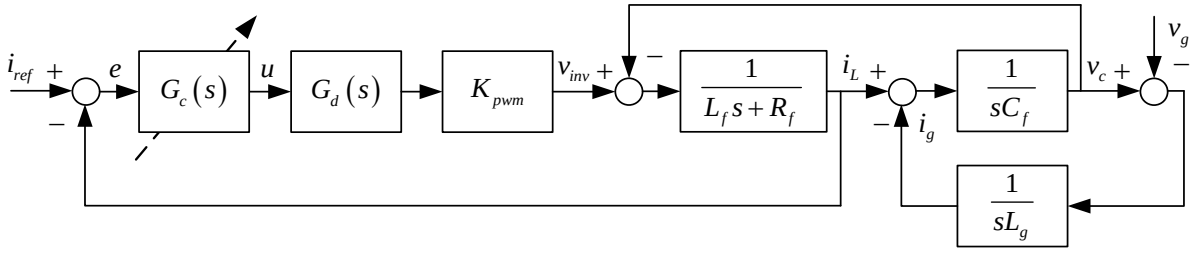

Figure 5.2 Control block diagram for a single-phase grid-connected inverter.

5.2.1 Grid Impedance Effect on Control Performance

When the single-phase inverter is connected to the grid, the grid side inductance combined with the LC filter of the inverter can form an LCL structure. The transfer function from inverter output voltage to inductor current can be derived as:

$$G_p'(s) = \frac{L_g C_f s^2 + 1}{L_f L_g C_f s^3 + (L_f + L_g) s} \tag{5.2}$$

The open loop transfer function from i_{ref} to i_L can be expressed as:

$$G_{open2}(s)=\frac{K_{pwm}G_c(s)G_d(s)\left(L_gC_fs^2+1\right)}{L_fL_gC_fs^3+\left(L_f+L_g\right)s} \tag{5.3}$$

Because the open loop cutoff frequency is much lower than the resonant frequency of the LCL structure, the filter capacitor can be neglected. The open loop transfer function of the system can be approximated by:

$$G_{open3}(s)=\frac{K_{pwm}G_c(s)G_d(s)}{\left(L_f+L_g\right)s} \tag{5.4}$$

The bode plot of the open loop transfer functions, given by (5.1), (5.3) and (5.4), is presented in Figure 5.3. It can be seen that ignoring the filter capacitance doesn't affect the frequency response in the low frequency range. Also note that the bandwidth of the open loop system is decreased significantly by the grid impedance, while the phase margin didn't change much. As a result, it is necessary to tune the controller parameters to maintain a satisfactory bandwidth. In this effort, a gain scheduling method was utilized to tune the controller parameters.

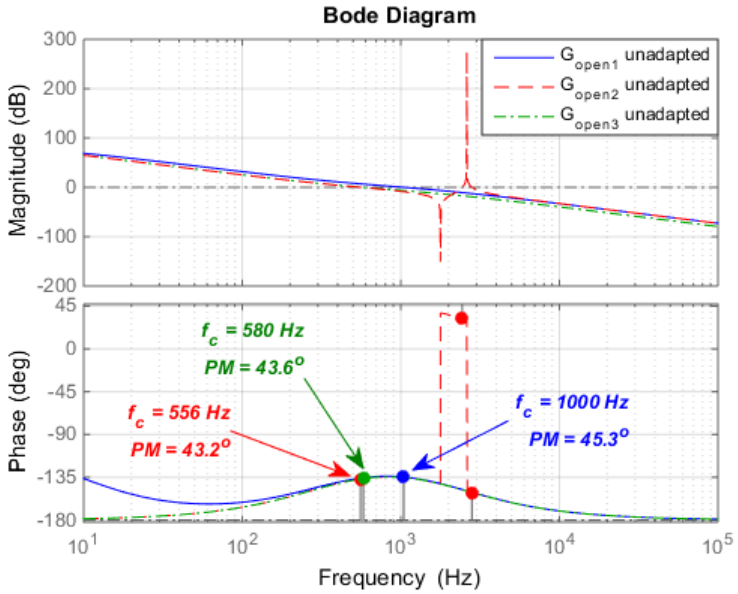

Figure 5.3 Bode plot of grid impedance (8 mH) effect on the system bandwidth and phase margin before adapting.

5.2.2 Gain Scheduling Control

When the inverter is connected into a weak grid ($L_g >> L_f$), the effect of grid impedance cannot be ignored. The basic idea of gain scheduling is to change the controller parameters by measurements of the process to compensate for variations in the process parameters. In order to maintain the controller bandwidth and phase margin when connecting to grid, the PI controller parameters need to be tuned taking into account the grid impedance. Therefore, the adaptation rule for the proportional gain and integral gain can be derived by:

$$\begin{aligned} k_p' &= k_p \cdot \frac{\omega_{res}'^2 - \omega_c^2}{\omega_r^2 - \omega_c^2} \\ k_i' &= \frac{k_p'\omega_c - k_p'\omega_c^2 T_d \tan(PM)}{\omega_c T_d + \tan(PM)} \end{aligned} \tag{5.5}$$

where $\omega_{res}' = \sqrt{\left(L_f + L_g\right)/L_f L_g C_f}$ is the resonant frequency and $\omega_r = \sqrt{1/L_g C_f}$. By examining (5.5), it can be seen that the adaptive control rule depends on the circuit parameters and the grid impedance. Figure 5.4 shows the open loop bode diagram after tuning the controller. Note that the bandwidth is maintained and the phase margin is also largely unaffected after adapting the controller parameters. It can also be found that neglecting the capacitor doesn't affect the bandwidth and phase margin too much. Therefore, the adaption rules can be simplified to (5.6).

$$\begin{aligned} k_p' &= k_p \cdot \left(1 + L_g / L_f\right) \\ k_i' &= k_i \cdot \left(1 + L_g / L_f\right) \end{aligned} \tag{5.6}$$

However, in general the grid impedance is usually unknown, so it is necessary to estimate it to apply the adaptive control rules.

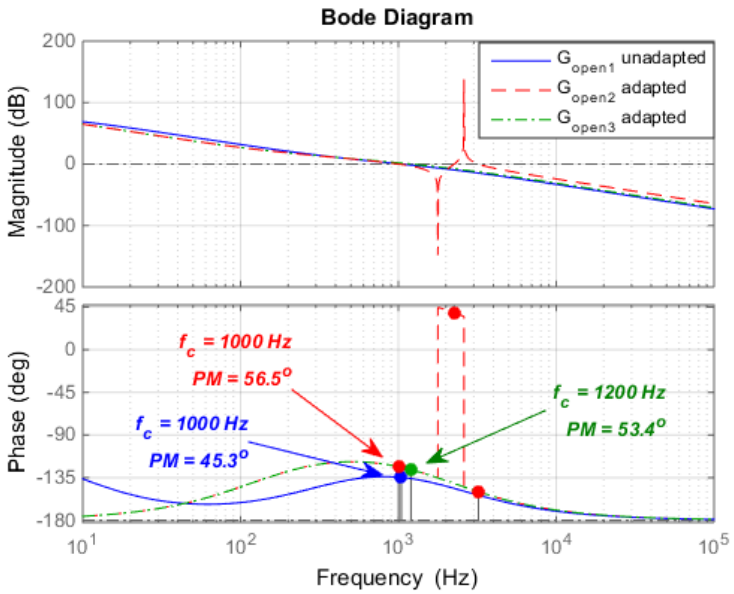

Figure 5.4 Bode plot of grid impedance (8 mH) effect on the system bandwidth and phase margin after adapting.

5.3 Grid Impedance Estimation

The online grid impedance estimation is required for controller parameter adaptation to mitigate the effect caused by grid impedance variations. Grid impedance estimation methods can be divided into active methods [50,51] and passive methods [54]. Active methods deliberately inject a disturbance signal periodically or randomly to measure the grid response so as to estimate the grid impedance, which might decrease the current quality. Passive methods use the grid background harmonics signal to estimate the grid impedance. However, both methods need to implement an online discrete Fourier transformation (DFT) analysis, which needs a lot of computational effort and will burden the DSP. In [55], the authors utilized a model predictive control algorithm to estimate the grid impedance. For an inverter operating under PQ control, the grid impedance can be estimated using PQ variations [53].

The simplest and most straightforward method to estimate the grid impedance is to measure the voltage across and the current flowing through the grid impedance. Since the filter capacitance

is very small, the current flow into it can be ignored. Therefore, the grid current can be approximated by the inductor current. The grid impedance can be estimated by the circuit equation (5.7), see Figure 5.1.

$$V_c(s) \approx V_g(s) + sL_g \cdot I_L(s) \tag{5.7}$$

The grid voltage cannot be measured directly in reality. To simplify the problem, we assume that the grid voltage is an ideal sinusoidal waveform (120V, 60Hz). The effect of a distorted grid voltage on the estimation results will be discussed later. The grid impedance can be estimated using the equation below [56].

$$L_g(k) = \frac{T_s}{N} \sum_{k=i}^{i+N} \frac{v_g(k) - v_c(k)}{i_L(k) - i_L(k-1)} \tag{5.8}$$

For this equation, it is necessary to sample the capacitor voltage and inductor current every T_s seconds. The difference between the grid voltage and capacitor voltage at a given sample and the difference between two consecutive current samples are utilized to estimate L_g. The grid impedance estimate is updated every 1 ms using this approach. The calculations are highly dependent on the accuracy of the samples. A ‘noisy’ sample can create a spike in the estimates. In order to reduce random errors due to sampling noise, the estimated grid impedance data is averaged every 0.25 s. Figure 5.5 presents the flow chart for the proposed grid impedance estimation algorithm.

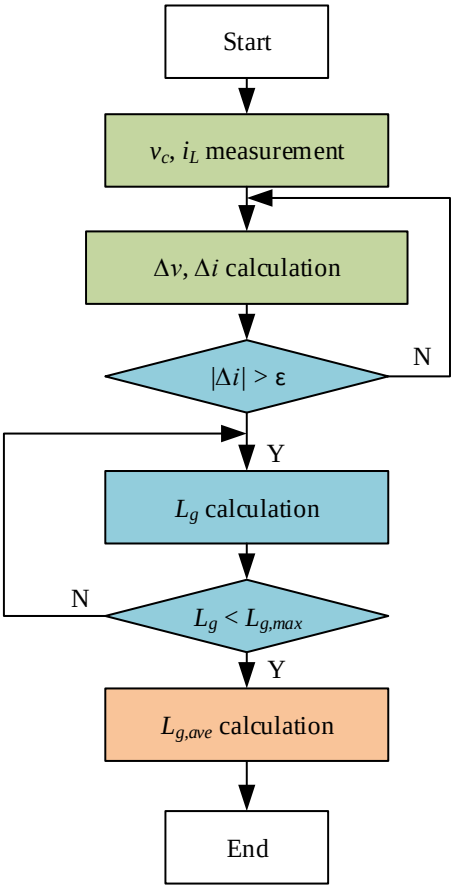

Figure 5.5 Flowchart of grid impedance estimation algorithm.

5.4 Controller Parameter Adaptation

Once the grid impedance estimation is completed, it can be used to update the current controller parameters. According to (5.6), the adapted proportional gain and integral gain can be obtained. Since the controller is implemented digitally, the continuous time PI controller needs to be transformed to a discrete time PI controller by the bilinear transformation, which is expressed in (5.9).

$$G_c(z) = \frac{b_0 + b_1 z^{-1}}{1 - z^{-1}}$$
$$b_0 = \frac{2k_p + k_i T}{2}, \quad b_1 = \frac{-2k_p + k_i T}{2} \tag{5.9}$$

Figure 5.6 shows the control block diagram for grid impedance estimation and controller parameter adaptation. Although increasing the proportional gain can maintain the system bandwidth, it may cause a resonance between the grid-connected inverter and the grid. Therefore, the proportional gain should be limited by the stability of the system.

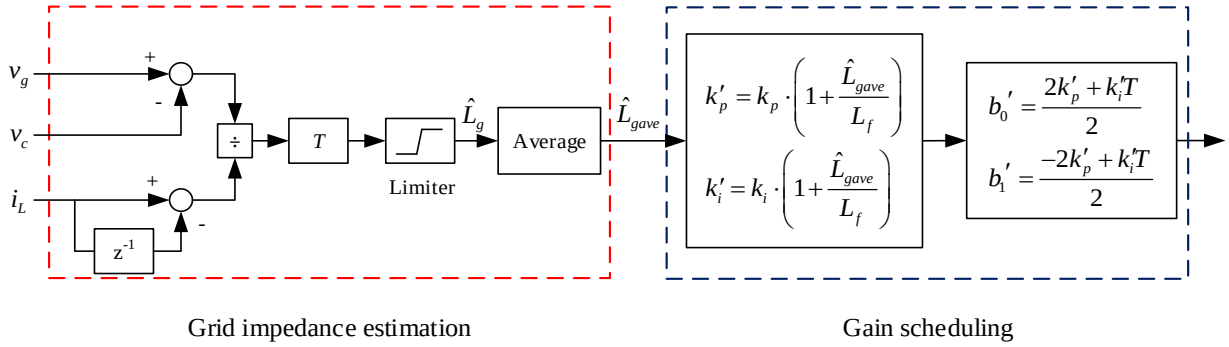

Figure 5.6 Control block diagram for grid impedance estimation and controller parameter adaptation.

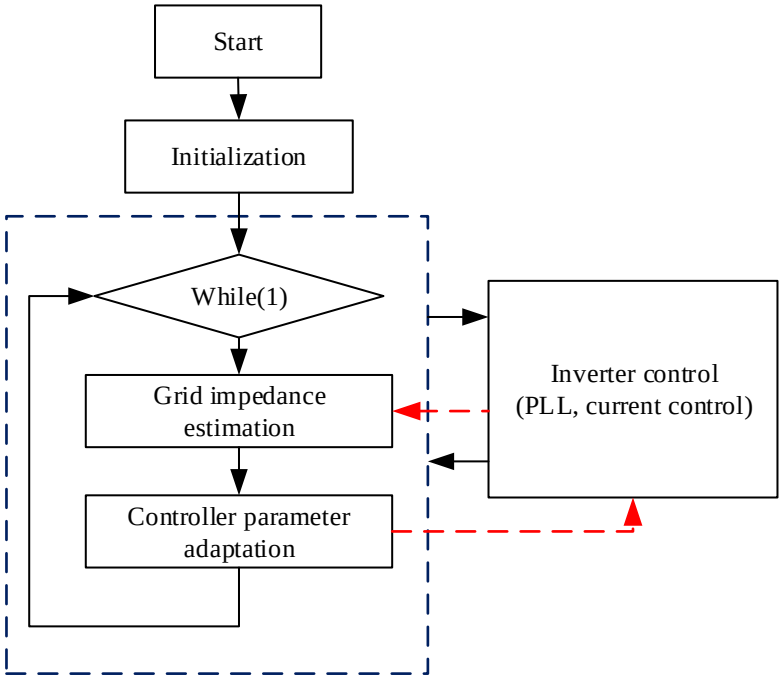

Figure 5.7 Flowchart of the computational process.

Figure 5.7 shows the flowchart of the overall tasks implemented within the DSP. After the DSP initialization, the inverter current control is executed every switching period. The grid impedance estimation and controller parameter adaptation are time-based tasks. The grid impedance estimation receives the voltage and current information preprocessed by the inverter control module. Once the grid impedance is estimated, the control parameters can be updated by the adaptation rules. The red dotted line represents the transfer of the information.

5.5 Simulation and Experimental Results

5.5.1 Simulation Results

To verify the effectiveness of the proposed method, simulation was performed using MATLAB to validate the theoretical analysis. The system parameters, as taken from the Texas Instruments single-phase grid-connected inverter, are given in Table 2-1. Figure 5.8 is a plot of the measured and estimated grid inductance under an ideal grid. Figure 5.9 is plot of the proportional and integral gain adaption based on the estimated grid inductance. Simulations were repeated with a distorted grid voltage, which is characterized by the presence of voltage harmonics. Figure 5.10 shows the estimated grid impedance and the measured grid impedance under a distorted grid. The proportional gain and integral gain adaptation based on the estimated grid impedance under a distorted grid is shown in Figure 5.11. Although the grid impedance estimation under a distorted grid fluctuates more than under an ideal grid, the controller parameter adaptation values don't change too much, which validates the effectiveness of the method. Since the grid impedance estimation value might vary around the true value all the time, the controller parameters are updated every 0.25 s in order to make the controller work stably.

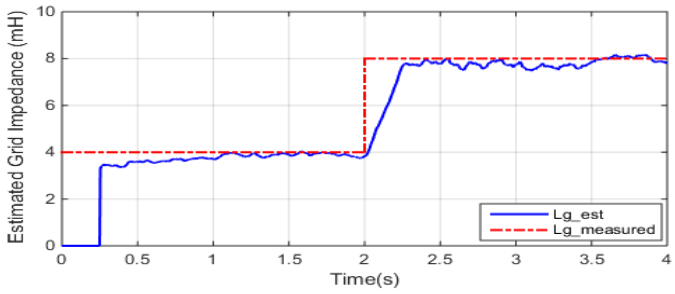

Figure 5.8 Measured and estimated grid impedance under ideal grid.

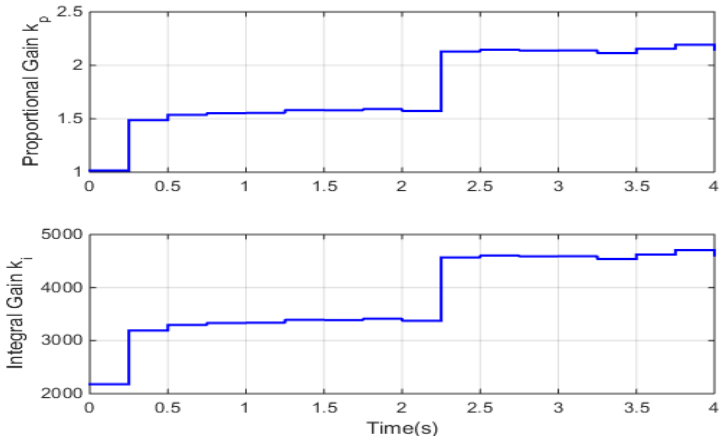

Figure 5.9 Controller parameter adaptation under ideal grid.

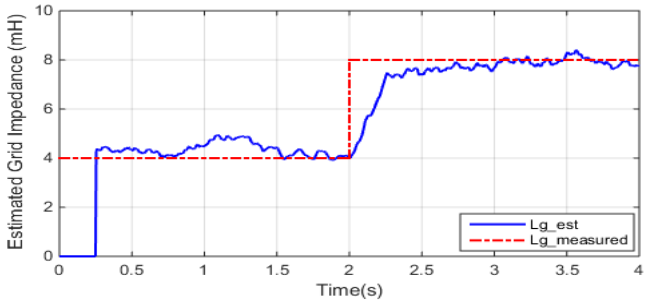

Figure 5.10 Measured and estimated grid impedance under distorted grid.

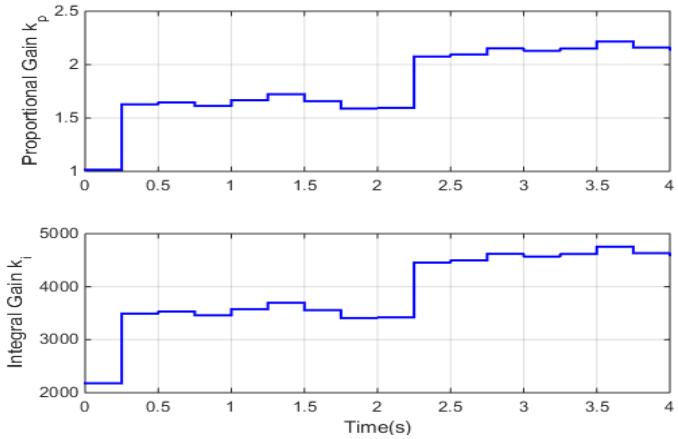

Figure 5.11 Controller parameter adaptation under distorted grid.

Presented in Figure 5.12 is the inverter output current waveform for a grid inductance of 14 mH when adapting the controller parameters at 0.25 s. The result shows the current is less distorted after adapting the parameter. Figure 5.13 and Figure 5.14 show the simulation results under ideal grid. The inverter output current total harmonic distortion decreased from 3.94% to 3.13% under adaptation. In practice, the utility grid always has harmonics: a distorted grid voltage was modeled by 10% third harmonics, 5% fifth harmonics, and 3% seventh harmonics. Figure 5.15 and Figure 5.16 show the simulation results under this distorted grid voltage. The current total harmonic distortion decreased from 4.52% to 3.22% under adaptation.

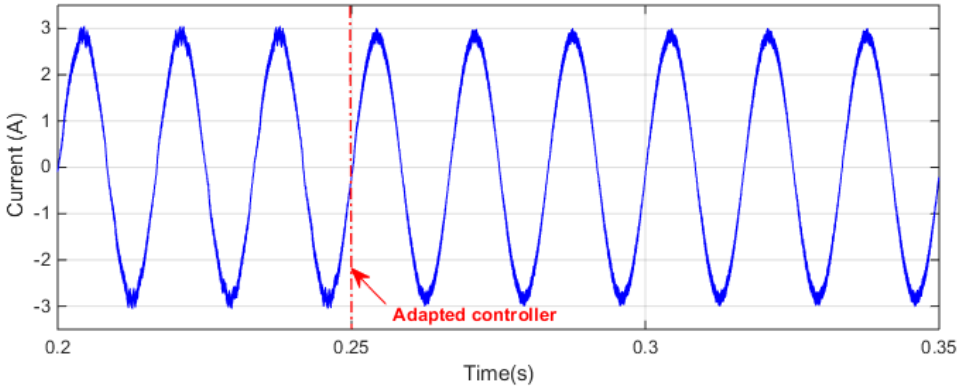

Figure 5.12 Inverter output current for L_g =14 mH adapted at 0.25s.

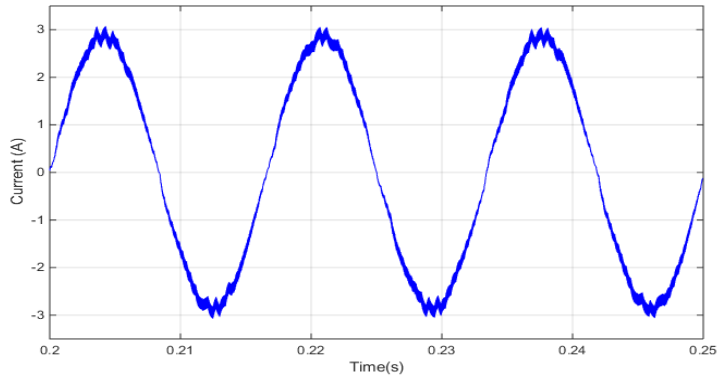

Figure 5.13 Inverter output current under ideal grid (unadapted).

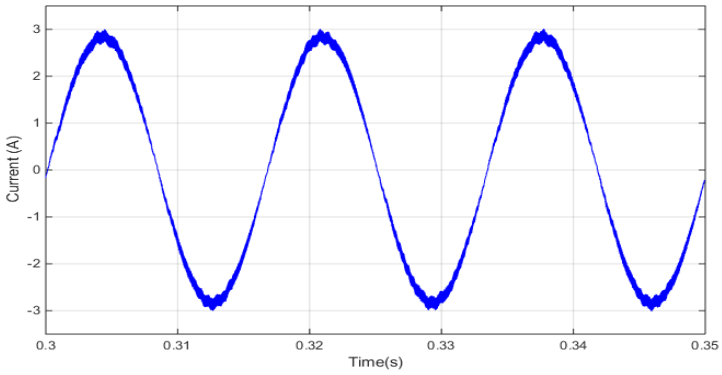

Figure 5.14 Inverter output current under ideal grid (adapted).

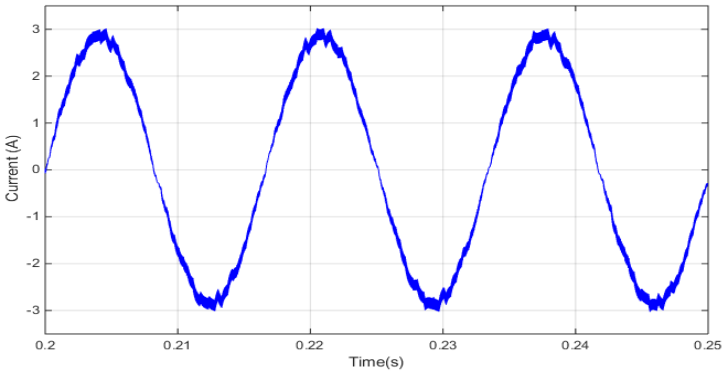

Figure 5.15 Inverter output current under distorted grid (unadapted).

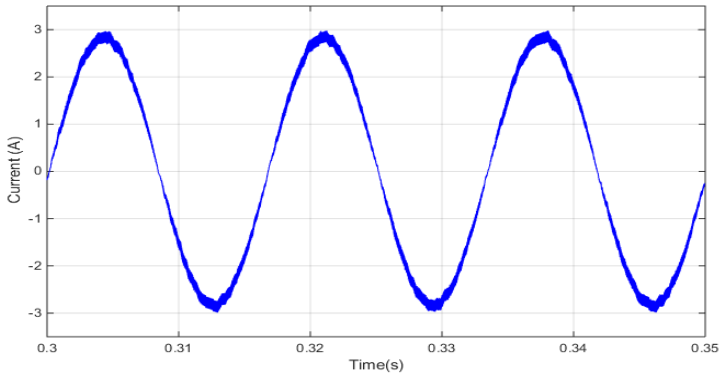

Figure 5.16 Inverter output current under distorted grid (adapted).

5.5.2 Experimental Results

Figure 5.17 shows the experimental results when grid impedance was 14 mH under ideal grid without adaptation and with adaptation. Figure 5.18 shows the experimental results for a distorted grid. The total harmonic distortion in the output current under ideal grid and distorted grid is presented in Table 5-1 and Table 5-2. The harmonics in the experimental results are much higher than in simulation. That is because the accuracy of the impedance estimation results might not be as good as the simulation estimation results due to the error caused by the voltage and current measurements and the data processing truncation in the DSP controller. Note that the magnitude of the current harmonics was reduced in both cases - ideal grid and distorted grid - with the gain scheduling algorithm.

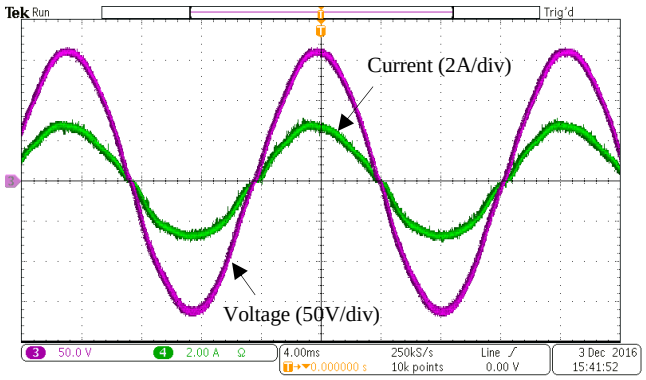

(a) unadapted

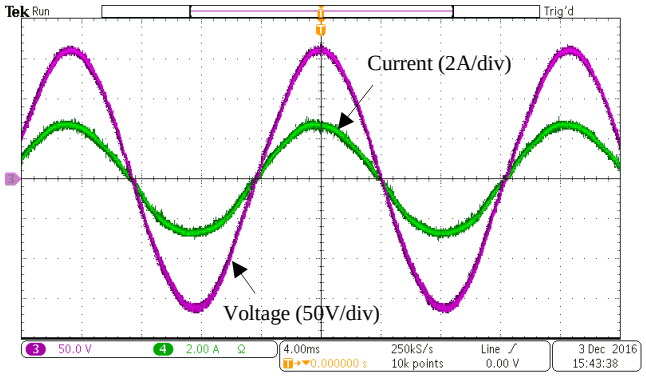

(b) adapted

Figure 5.17 Inverter output voltage and current under ideal grid.

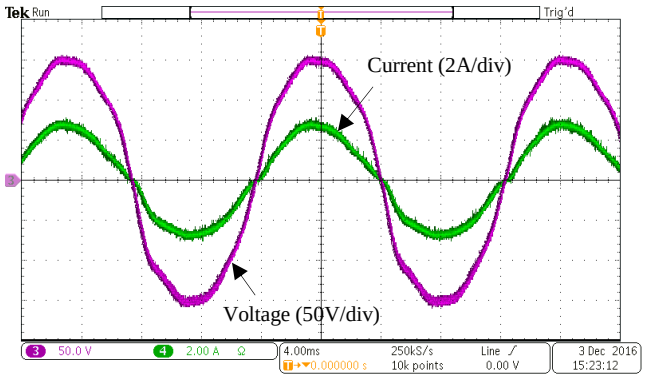

(a) unadapted

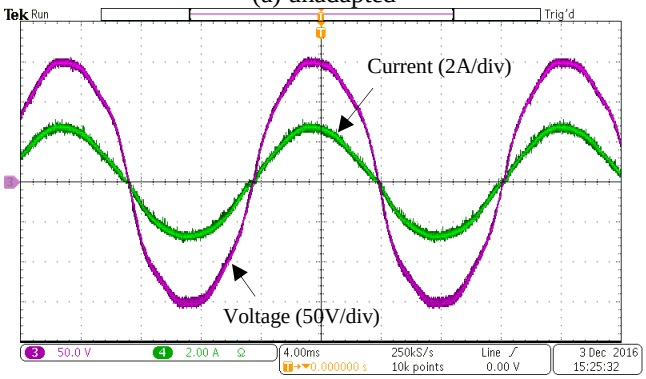

(b) adapted

Figure 5.18 Inverter output voltage and current under distorted grid.

Table 5-1 Inverter Output Current Harmonic Under Ideal Grid

Harmonic Order	Unadapted system	Adapted system
3rd	4.79%	2.11%
5th	3.34%	0.78%
7th	3.69%	0.81%
9th	3.21%	1.08%
11th	1.47%	0.44%

13th	0.93%	0.46%

Table 5-2 Inverter Output Current Harmonic Under Distorted Grid

Harmonic Order	Unadapted system	Adapted system
3rd	5.71%	2.68%
5th	4.72%	1.21%
7th	4.06%	1.86%
9th	2.89%	1.09%
11th	1.59%	0.78%
13th	1.04%	0.83%

5.6 Conclusion

The effect of the grid impedance on the control performance of a single-phase grid-connected inverter with an LC filter has been studied. The control performance can be degraded and even become unstable when the grid impedance is large. To maintain the control performance, a gain scheduling control method has been proposed. This method requires estimation of the grid impedance. By adjusting the controller parameters using the estimated grid impedance, the bandwidth and phase margin of the controller can be maintained. The effectiveness of the proposed method has been demonstrated through both simulated and experimental results. It has been shown that the magnitude of the current harmonics was reduced for both an ideal grid and a distorted grid.

CHAPTER 6 GRID CURRENT OBSERVER BASED CONTROLLER DESIGN

In the distribution system, grid voltage distortion and grid impedance uncertainty can degrade the control performance of a grid-connected inverter. A technique commonly used for improving the performance of the control loop is to introduce a feed forward term which compensates for the effect of one or more system disturbance terms. This chapter presents a grid current observer based compensation control for a single-phase grid-connected inverter that is connected to a weak grid. Traditional single-loop PI current control performance suffers in the presence of the grid voltage distortion and grid impedance uncertainty. To compensate for disturbances from the grid side, two different compensation control structures are proposed. One is a feed forward method, which uses estimated grid current as a feed forward signal. The other one is a modified disturbance observer method, which compensates for the estimated disturbance. Simulation and experiments have been carried out on the experimental testbed.

6.1 Introduction

The grid-connected inverter is usually connected between the renewable energy and the utility grid. In reality, the grid voltage is not always an ideal sinusoidal waveform, but is distorted. Furthermore, the grid impedance is usually unknown, which will also introduce harmonics into the system, and in some cases even make the inverter system unstable.

In order to get an accurate control, any disturbance should be compensated. In general, when a disturbance is measurable, a feed forward strategy could reduce or even eliminate the effect of the disturbance [68, 69]. But an additional sensor will increase the inverter cost. The grid current observer-based feed forward compensation method was proposed to solve the problem in this work. When a disturbance cannot be measured directly, the disturbance observer is often used to

compensate for the influence of the disturbance [25, 70, 71]. A modified disturbance observer was described that can achieve more accurate disturbance estimation. With properly designed observer parameters, it is possible to reduce control sensitivity to model uncertainties, parameter mismatches, and noise on sensed variables. Consequently, the influence of uncertainties can be more effectively suppressed, and inverter performance robustness can be improved.

6.2 Grid Current Observer Based Compensation

When the inverter is connected to a weak grid, the effect of grid impedance and grid voltage distortion cannot be ignored. The grid voltage distortion and grid impedance uncertainty will introduce harmonics into the inverter output current. Therefore, compensation is used to reduce the grid disturbance and improve the system stability. The relationship between the grid current and the disturbances, i.e., grid impedance and grid voltage, can be expressed as follows: $v_c = L_g \frac{di_g}{dt} + v_g$ (see Figure 3.1). Since the grid voltage is usually unmeasurable and the grid impedance is unknown, the grid current is selected as the compensation signal. Therefore, the compensation control can be realized in two different ways.

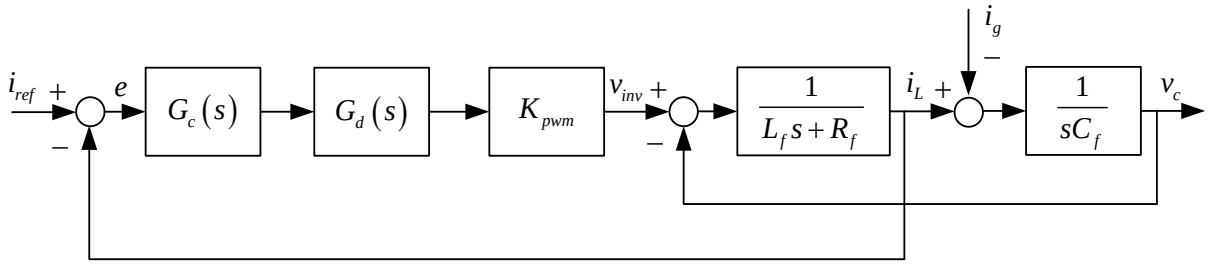

Figure 6.1 Control block diagram for a single-phase grid-connected inverter.

6.2.1 Feed Forward Compensation Design

The feed forward compensation method can eliminate the effect of the disturbance on the system [68]. Since an additional current sensor will increase the cost of the system, an observer is

used to estimate the grid current and will be described in Section 6.3. The estimated grid current is fed forward in the system to reduce the disturbance caused by the grid voltage distortion and grid impedance. In order to derive the feed forward gain, the estimated grid current is replaced by the grid current, as shown in Figure 6.2.

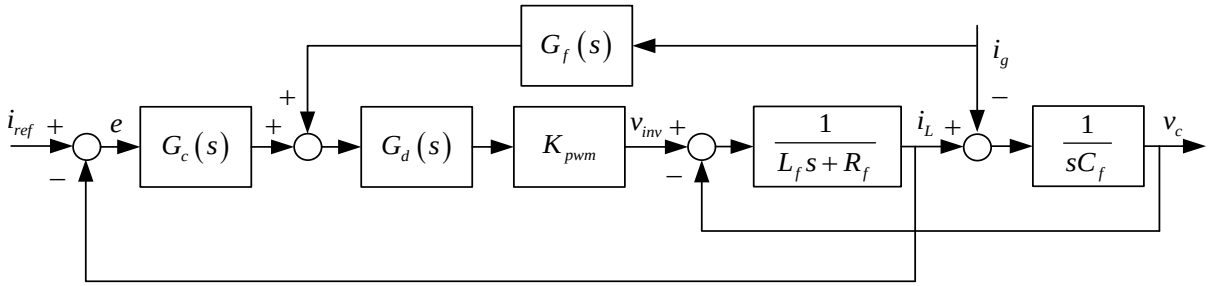

Figure 6.2 Control block diagram for a single-phase grid-connected inverter with feed forward strategy.

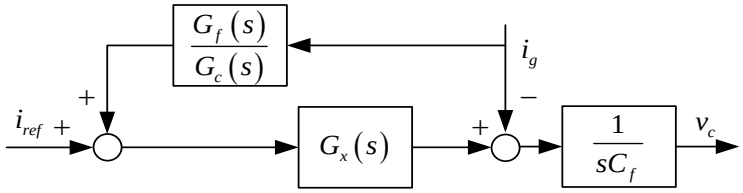

Figure 6.3 Equivalent transformation control block diagram of Figure 6.2.

Figure 6.2 can be further simplified to Figure 6.3 by block diagram equivalent transformations. The feed forward transfer function can be shown to be equivalent to:

$$G_f(s) = \frac{L_f s + R_f}{G_d(s)} + G_c(s) \tag{6.1}$$

where $G_c(s)$ is the transfer function of a PI controller, and $G_d(s)$ is the transfer function of the delay. Generally, it is difficult to implement a second order differentiation in a digital control system especially for the case of weak grid and heavy noise, so the feed forward gain can be simplified into (6.2).

$$G_f(s) = R_f + k_p \tag{6.2}$$

6.2.2 Modified Disturbance Observer Design

A disturbance observer has been reported in many control system studies in which the external disturbance cannot be directly measured. The basic idea is to compensate the external disturbance based on disturbance estimation from measurable variables through a combination of the inverse plant model and a low pass filter. The estimated disturbances, which include system uncertainties, are fed back so that robustness of a system is achieved.

In the present application, the harmonic content in the grid current caused by the grid voltage distortion and grid impedance uncertainty can be regarded as the system disturbance. Figure 6.4 shows the control diagram of a single-phase grid-connected inverter with a disturbance observer. Assume that the current control loop in Figure 6.1 is ideally controlled [70]. From Figure 6.4, it can be found that the disturbance signal, i.e., the grid current, is estimated from the inductor current and capacitor voltage. Research shows that a better estimate could be obtained if more accurate information was incorporated into the observer [72], which has been verified in our work. The researchers in [73] also demonstrated that only using the capacitor dynamics equation to estimate the grid current is very sensitive to noise in the measurements caused by the derivative of the capacitor voltage. Therefore, a modified disturbance observer is used to get a more accurate estimation. Figure 6.4 can be rearranged into Figure 6.5. A notch filter is added to filter out the fundamental frequency content in the estimated grid current. Therefore, the harmonic content introduced into the grid current by the disturbances and system uncertainties can be compensated by the estimated grid current except for the fundamental frequency.

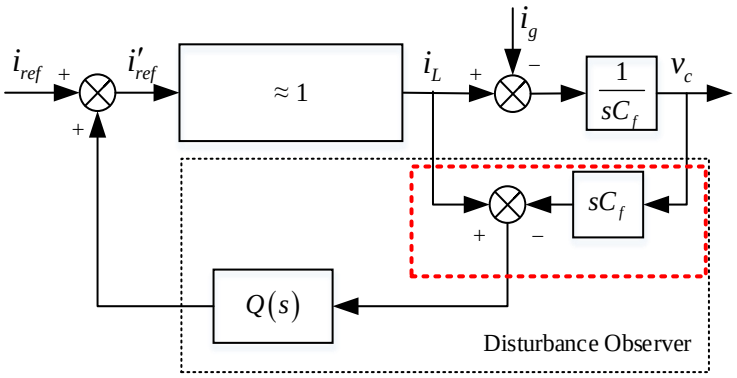

Figure 6.4 Control block diagram of the system using disturbance observer.

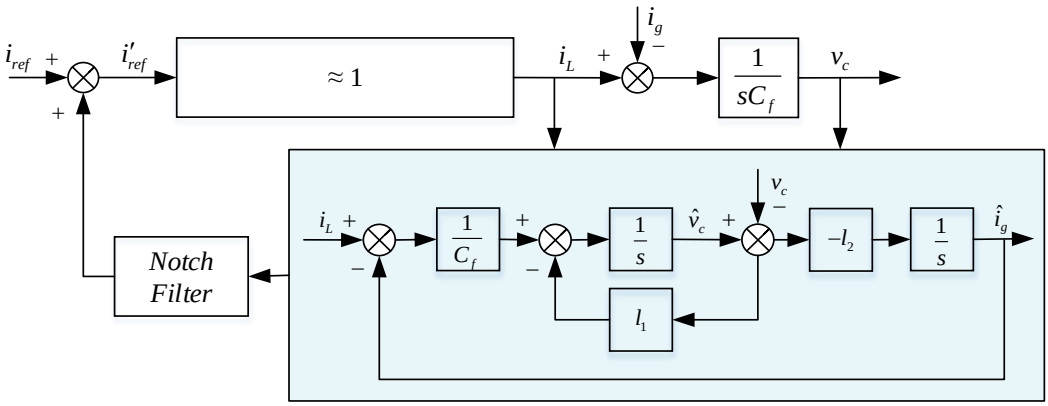

Figure 6.5 Control block diagram of the system using modified disturbance observer.

The notch filter is designed to filter out the fundamental frequency in the estimated grid current and is given by (6.3).

$$G_{notch}(s) = \frac{s^2 + \xi\omega_c s + \omega_0^2}{s^2 + \omega_c s + \omega_0^2} \tag{6.3}$$

where ξ is the depth of the notch filter, ω_c is the width of the notch, and ω_0 is the frequency of the notch. In this work, the notch filter parameters were set as follows: ξ = 0.001, ω_c = 125.7 rad/s, and ω_0 = 377 rad/s. Details of the proposed grid current observer are described next.

6.3 Grid Current Observer Design

Assume that the grid current is constant in one sampling period [73]. Select the capacitor voltage and grid current as the state variables and the inductor current i_L as the input. Then a continuous time state space model can be expressed by:

$$\begin{aligned} \dot{x} &= Ax + Bu \\ y &= Cx \end{aligned} \tag{6.4}$$

where

$$A = \begin{bmatrix} 0 & -1/C_f \\ 0 & 0 \end{bmatrix} \quad B = \begin{bmatrix} 1/C_f \\ 0 \end{bmatrix} \quad C = \begin{bmatrix} 1 & 0 \end{bmatrix} \quad x = \begin{bmatrix} v_c \\ i_g \end{bmatrix}$$

The equivalent discrete time state space equations is:

$$\begin{aligned} x[k+1] &= Fx[k] + Gu[k] \\ y[k] &= Hx[k] \end{aligned} \tag{6.5}$$

where

$$F = \begin{bmatrix} 1 & -T/C_f \\ 0 & 1 \end{bmatrix} \quad G = \begin{bmatrix} T/C_f \\ 0 \end{bmatrix} \quad H = C$$

The state estimator is described by (6.6). Figure 6.6 shows the control block diagram of the plant and the observer.

$$\begin{aligned} \hat{x}[k+1] &= F\hat{x}[k] + Gu[k] + L\left(y[k] - \hat{y}[k]\right) \\ \hat{y}[k] &= H\hat{x}[k] \end{aligned} \tag{6.6}$$

where L is the observer gain.

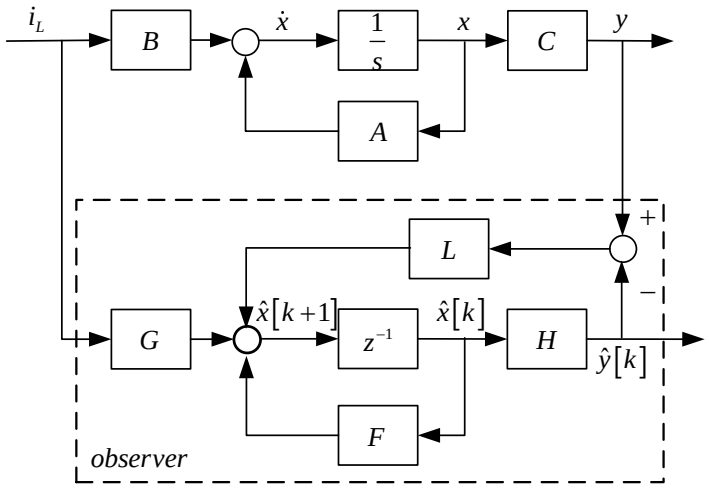

Figure 6.6 Block diagram of the plant and state observer.

The observability matrix in (6.7) has full rank, which means that the system is observable.

$$rank\begin{bmatrix} H \\ HF \end{bmatrix} = 2 \tag{6.7}$$

The error dynamic can be expressed as follows. The error will converge to zero if the eigenvalues of *F-LH* are within the unit circle in the *z*-plane.

$$e[k+1] = x[k+1] - \hat{x}[k+1] = (F - LH)\left(x[k] - \hat{x}[k]\right) = (F - LH)e[k] \tag{6.8}$$

Since the state variables are observable, the eigenvalues of the characteristic equation in (6.9) can be freely chosen within the unit circle. Usually the observer poles are chosen at least 2 times higher than the poles of the closed-loop system [69, 74]. In this work, the observer poles are selected 3 times faster than the closed-loop poles as shown in Figure 6.7. The circuit shown in Figure 3.1 is simulated with the designed state observer. The measured grid current and estimated grid current are shown in Figure 6.8. It has been shown that the observer makes a good estimation of the grid current without the need of an additional current sensor.

$$\det\left(zI - \left(F - LH\right)\right) = 0 \tag{6.9}$$

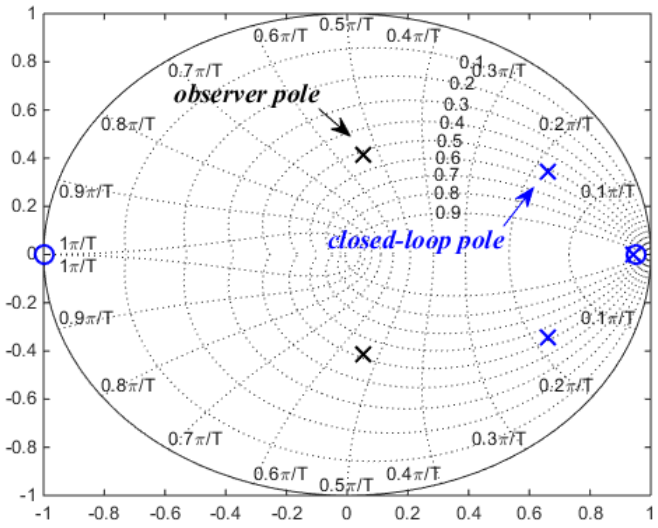

Figure 6.7 Pole locations for observer and the closed-loop system.

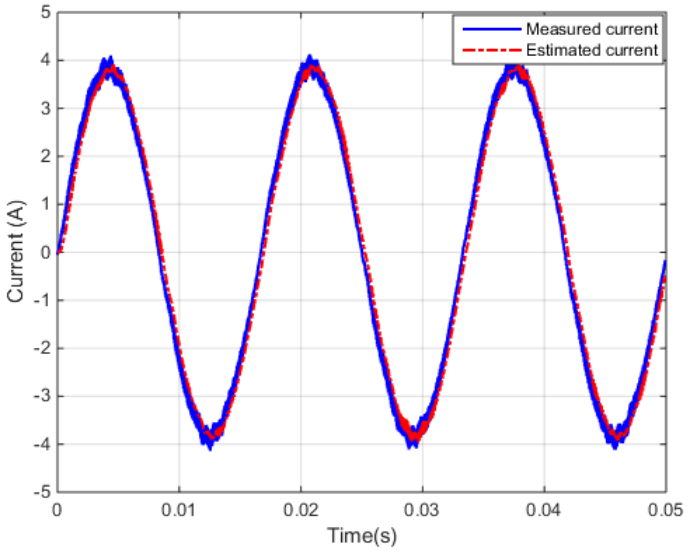

Figure 6.8 Measured grid current and estimated grid current.

6.4 Simulation and Experimental Results

6.4.1 Simulation Results

Two sets of simulations were performed to verify the effectiveness of the proposed controller. The first simulations were for an ideal grid with: 1) the feed forward, 2) the modified disturbance observer, and 3) without compensation. The grid impedance (L_g = 15.5 mH) is connected to the grid side at 0.15 s. The inverter output current THD using the feed forward method

before and after adding the grid impedance is 3.04% and 3.22%, respectively. The current THD using the modified disturbance observer method before and after adding grid impedance is 3.20% and 3.25%, respectively. The current THD without any compensation before and after adding grid impedance is 3.43% and 3.54%, respectively. The simulation results are shown in Figure 6.9 - Figure 6.11.

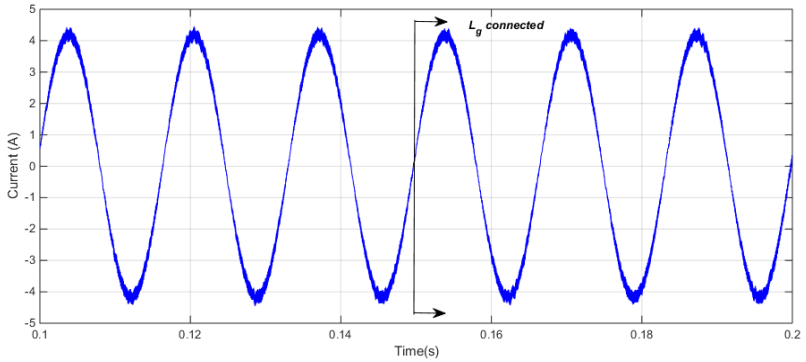

Figure 6.9 Inverter output current using the feed forward method.

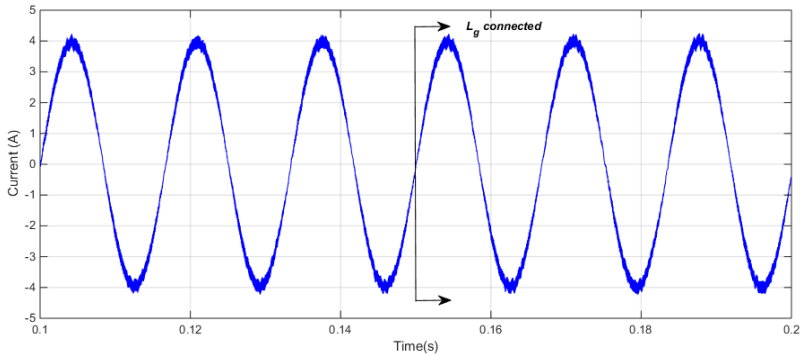

Figure 6.10 Inverter output current using the modified disturbance observer.

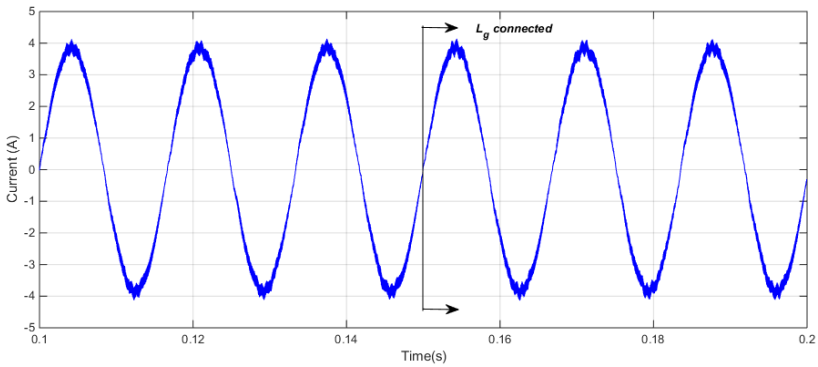

Figure 6.11 Inverter output current without compensation.

Next the simulations were repeated for a distorted grid (20% 3rd harmonic, 10% 5th harmonic and 10% 7th harmonic). The grid impedance (L_g = 15.5 mH) was connected to the grid side at 0.15 s. The inverter output current THD using the feed forward method before and after adding grid impedance is 3.24% and 3.28%, respectively. The current THD using the modified disturbance observer method before and after adding grid impedance is 3.48% and 3.52%, respectively. The current THD without any compensation before and after adding grid impedance is 3.67% and 3.74%, respectively. The simulation results are shown in Figure 6.12 - Figure 6.14.

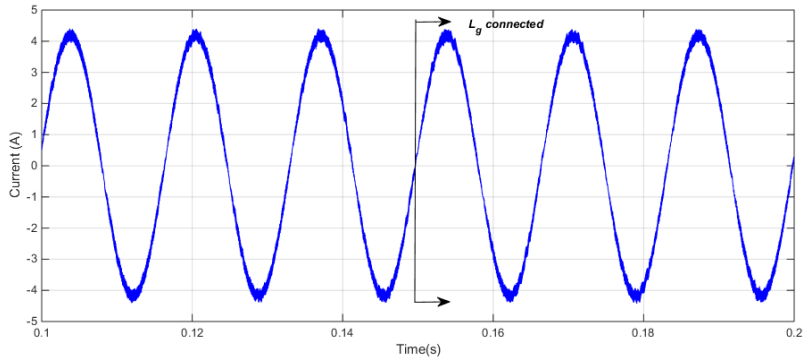

Figure 6.12 Inverter output current using the feed forward method.

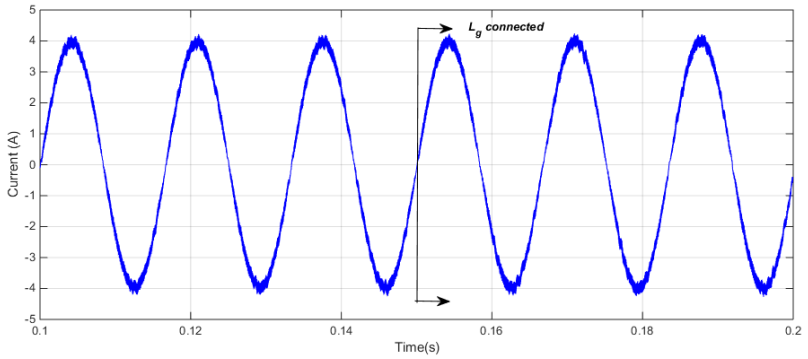

Figure 6.13 Inverter output current using the modified disturbance observer.

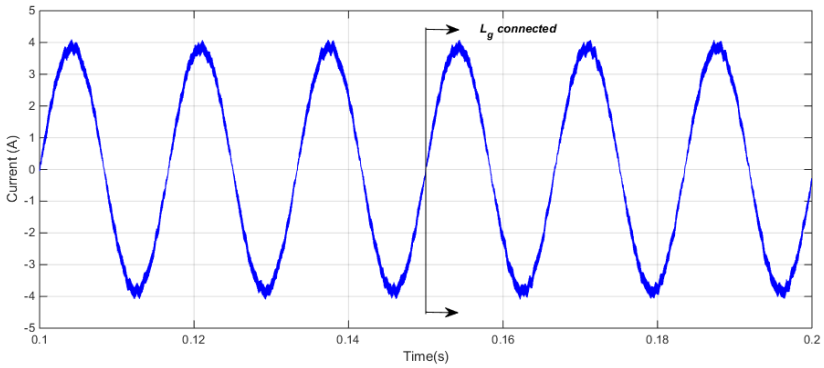

Figure 6.14 Inverter output current without compensation.

6.4.2 Experimental Results

The experimental testbed was used to validate the theoretical analysis. Figure 6.15 - Figure 6.17 show the experimental waveforms using the feed forward method, the modified disturbance observer method and without compensation under an ideal grid. The current harmonic analysis is shown in Table 6-1. The harmonics are reduced by using either the feed forward method or the modified disturbance observer method as compared to the control without any compensation.

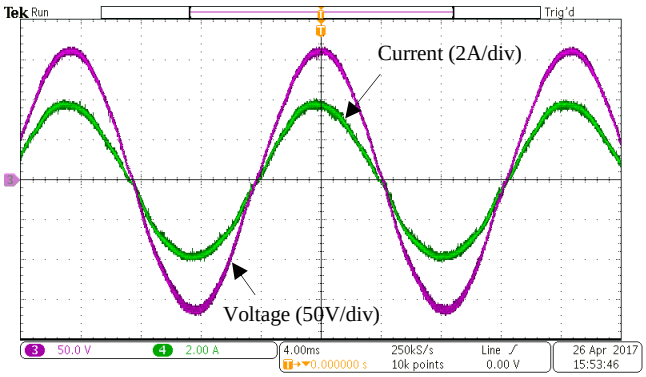

Figure 6.15 Output voltage and current using the feed forward method.

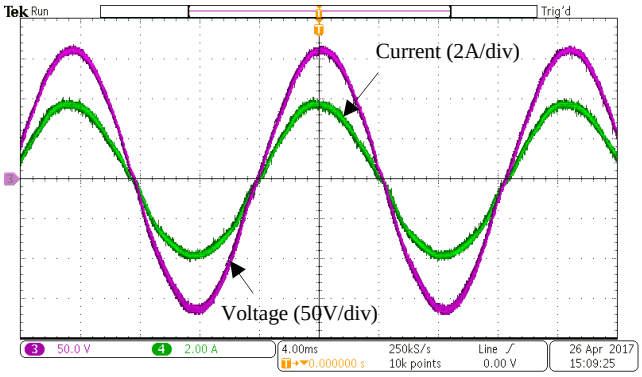

Figure 6.16 Output voltage and current using the modified disturbance observer.

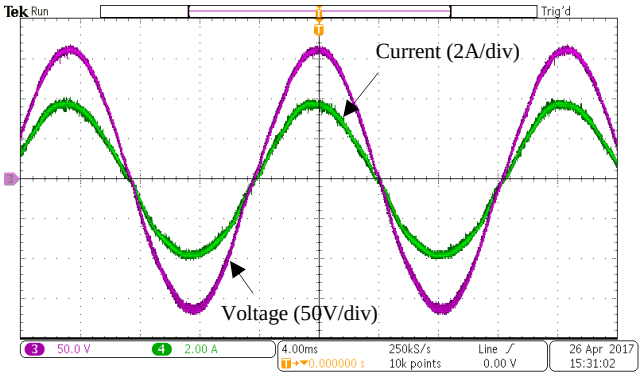

Figure 6.17 Output voltage and current without compensation.

Table 6-1 Grid Current Harmonics Under Ideal Grid

Harmonic Order	Feed Forward Method	Modified Disturbance Observer	Without Compensation
3rd	2.52%	2.66%	3.85%
5th	1.83%	1.79%	1.71%
7th	1.99%	1.90%	1.90%
9th	2.27%	2.65%	2.56%
11th	1.42%	1.57%	1.20%
13th	0.71%	0.99%	0.60%

Figure 6.18 - Figure 6.20 show the experimental waveforms using the feed forward method, the modified disturbance observer method and without compensation under a distorted grid. The

current harmonic analysis is shown in Table 6-2. The feed forward method and modified disturbance observer can improve the disturbance rejection ability of the system.

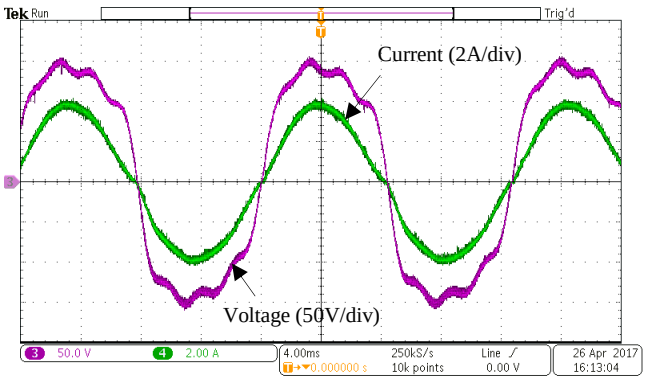

Figure 6.18 Output voltage and current using the feed forward method.

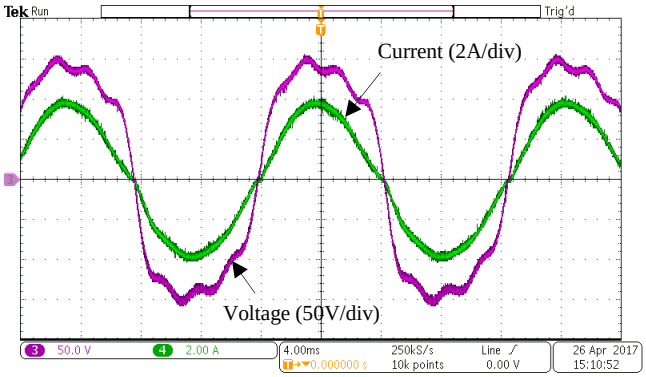

Figure 6.19 Output voltage and current using the modified disturbance observer.

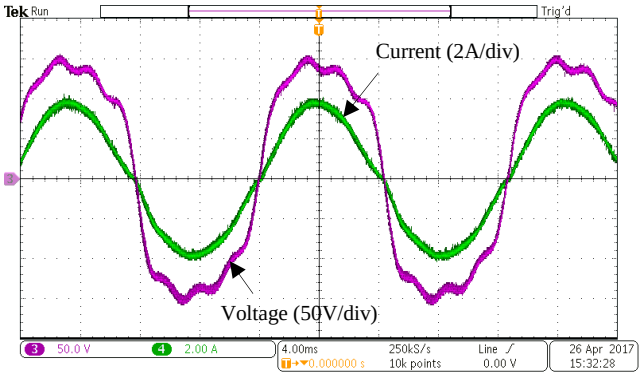

Figure 6.20 Output voltage and current without compensation.

Table 6-2 Grid Current Harmonics Under Distorted Grid

Harmonic Order	Feed Forward Method	Modified Disturbance Observer	Without Compensation
3rd	6.61%	7.03%	7.81%
5th	3.71%	4.10%	4.22%
7th	4.33%	4.29%	4.76%
9th	1.90%	1.68%	1.77%
11th	1.28%	0.89%	1.17%
13th	0.85%	0.65%	0.90%

6.5 Conclusion

Grid current observer based feed forward method and a modified disturbance observer have been proposed to reduce the effect of the grid impedance uncertainty and grid voltage distortion on a single-phase grid-connected inverter. Disturbance rejection ability can be improved by adopting disturbance compensation. Simulation and experimental results have shown that the proposed controller can achieve reduced total harmonic distortion (THD) and robustness to grid impedance variation.

CHAPTER 7 CONCLUSION AND FUTURE WORK

In this work, the control methods including regulating inverter output impedance by adjusting controller parameters, state feedback control combined with PI/PR controller, gain scheduling method based on grid impedance estimation and grid current observer based compensation method have been investigated to solve the impact of grid impedance on the control performance and stability of the system. These works are summarized in this chapter, and suggestions for future work are provided.

7.1 Summary of Research

Regulating the output impedance of the single-phase grid-connected inverter by shaping the controller parameters can improve the stability of the inverter system when it is connected to a weak grid. Based on the frequency domain analysis, it can be found that by increasing the proportional gain of the PI controller, the magnitude of the inverter output impedance can be increased to improve the ability for harmonic rejection, while the phase margin is decreased which might make the system unstable. Changing the integral gain of the PI controller has the similar effect as the proportional gain, which mainly influences on the low frequency characteristics. Although this method is effective to reduce the grid impedance effect, it is an offline control method which needs to know the grid impedance value before shaping the controller parameters.

State feedback control combined with PI/PR controller is a robust method which can enhance stability and increase damping to reduce the LC filter resonance. Pure state feedback control can yield a steady state error. Therefore, a PI/PR controller was augmented to improve the controller performance. The state feedback gain and PI/PR controller parameters were determined by using the pole placement method. This method provides a straightforward way to design the

controller parameters according to the system specification. By proper selection of the poles of the closed-loop system, sensitivity to parameter uncertainties can be reduced. Experimental results showed that the state feedback control combined with PI controller provided good harmonic rejection ability and robustness to grid impedance variations compared to traditional PI/PR control only. For the state feedback control combined with PR controller, a harmonic compensator is utilized to suppress 3rd, 5th and 7th order current harmonics. This method also provided good harmonic rejection ability and dynamic performance. Therefore, the state feedback control combined with PI/PR controller is effective to a wide range of grid impedance variations even under a distorted grid.

Gain scheduling control method is an adaptive method based on grid impedance estimation to adjust the controller parameters. With an increase in the grid impedance, the open loop cutoff frequency decreases, which affects the transient performance. Also, the phase margin of the system decreases, which deteriorates the system stability. In order to maintain the controller bandwidth and phase margin at satisfactory levels, the controller parameters were tuned based on the grid impedance estimation to compensate for the system parameter variations caused by the presence of grid impedance. Compared to the method introduced in Chapter 3, this method is an online control method, which can adjust the controller parameters in real time.

The grid current observer based compensation methods provide two different compensation control structures to attenuate the impact of grid impedance uncertainty and grid voltage distortion. These two compensation structures, i.e., feed forward compensation and a modified disturbance observer compensation, are essentially the same. Experiment results have shown the similar performance of these two methods. The disturbance rejection ability of the system was improved by using the proposed compensation methods.

7.2 Suggestion for Future Work

The interaction between the grid-connected inverter and the utility grid is mainly discussed from the inverter current control perspective. In the experimental testbed, the phase lock loop (PLL) control, which is used to synchronize inverter output current with the grid voltage, is also a part of inverter control system. The impact of the PLL control on the stability of the inverter system hasn't been explored in this work. Since the inverter reference current is produced by the current amplitude and the phase detected by PLL, the PLL can affect the stability of the inverter system when the grid is weak. Researchers have shown that PLL can introduce a paralleled admittance into the output admittance of the inverter, which may cause low order harmonic oscillation in a weak grid. This requires further investigation to optimize the PLL parameters to improve the stability of the inverter system under a weak grid.

REFERENCES

[1] F. Blaabjerg, R. Teodorescu, M. Liserre and A. V. Timbus, "Overview of Control and Grid Synchronization for Distributed Power Generation Systems," in IEEE Transactions on Industrial Electronics, vol. 53, no. 5, pp. 1398-1409, Oct. 2006.

[2] M. Liserre, F. Blaabjerg and S. Hansen, "Design and control of an LCL-filter-based three-phase active rectifier," in IEEE Transactions on Industry Applications, vol. 41, no. 5, pp. 1281-1291, Sept.-Oct. 2005.

[3] Liserre, M., Teodorescu, R., Blaabjerg, F., "Stability of photovoltaic and wind turbine grid-connected inverters for a large set of grid impedance values," Power Electronics, IEEE Transactions on, vol.21, no.1, pp.263,272, Jan. 2006.

[4] J. H. R. Enslin and P. J. M. Heskes, "Harmonic interaction between a large number of distributed power inverters and the distribution network," in IEEE Transactions on Power Electronics, vol. 19, no. 6, pp. 1586-1593, Nov. 2004.

[5] A. A. Girgis and R. B. McManis, "Frequency domain techniques for modeling distribution or transmission networks using capacitor switching induced transients," in IEEE Transactions on Power Delivery, vol. 4, no. 3, pp. 1882-1890, Jul 1989.

[6] S. Cobreces, E. Bueno, F. J. Rodriguez, F. Huerta1 and P. Rodriguez, "Influence analysis of the effects of an inductive-resistive weak grid over L and LCL filter current hysteresis controllers," 2007 European Conference on Power Electronics and Applications, Aalborg, 2007, pp. 1-10.

[7] M. Cespedes and J. Sun, "Renewable Energy Systems Instability Involving Grid-Parallel Inverters," 2009 Twenty-Fourth Annual IEEE Applied Power Electronics Conference and Exposition, Washington, DC, 2009, pp. 1971-1977.

[8] Henrik Binder, “Power Control for Wind Turbines in weak Grids: Concepts Development” RisØ National Laboratory, Roskilde March 1999.

[9] G. Ledwich and H. Sharma, "Connection of inverters to a weak grid," 2000 IEEE 31st Annual Power Electronics Specialists Conference. Conference Proceedings (Cat. No.00CH37018), Galway, 2000, pp. 1018-1022 vol.2.

[10] T. Abeyasekera, C. M. Johnson, D. J. Atkinson and M. Armstrong, "Suppression of line voltage related distortion in current controlled grid connected inverters," in IEEE Transactions on Power Electronics, vol. 20, no. 6, pp. 1393-1401, Nov. 2005.

[11] J. Sun, "Impedance-Based Stability Criterion for Grid-Connected Inverters," in IEEE Transactions on Power Electronics, vol. 26, no. 11, pp. 3075-3078, Nov. 2011.

[12] J. Xu, S. Xie and T. Tang, "Evaluations of current control in weak grid case for grid-connected LCL-filtered inverter," in IET Power Electronics, vol. 6, no. 2, pp. 227-234, Feb. 2013.

[13] D. G. Holmes, T. A. Lipo, B. P. McGrath and W. Y. Kong, "Optimized Design of Stationary Frame Three Phase AC Current Regulators," in IEEE Transactions on Power Electronics, vol. 24, no. 11, pp. 2417-2426, Nov. 2009.

[14] G. Shen, D. Xu, L. Cao and X. Zhu, "An Improved Control Strategy for Grid-Connected Voltage Source Inverters With an LCL Filter," in IEEE Transactions on Power Electronics, vol. 23, no. 4, pp. 1899-1906, July 2008.

[15] D. N. Zmood and D. G. Holmes, "Stationary frame current regulation of PWM inverters with zero steady-state error," in IEEE Transactions on Power Electronics, vol. 18, no. 3, pp. 814-822, May 2003.

[16] R. Teodorescu and F. Blaabjerg, "Proportional-resonant controllers. A new breed of controllers suitable for grid-connected voltage-source converters," in Proc. OPTIM, 2004, vol. 3, pp. 9–14.

[17] G. Shen, X. Zhu, J. Zhang and D. Xu, "A New Feedback Method for PR Current Control of LCL-Filter-Based Grid-Connected Inverter," in IEEE Transactions on Industrial Electronics, vol. 57, no. 6, pp. 2033-2041, June 2010.

[18] V. Blasko and V. Kaura, "A novel control to actively damp resonance in input LC filter of a three phase voltage source converter," Applied Power Electronics Conference and Exposition, 1996. APEC '96. Conference Proceedings 1996., Eleventh Annual, San Jose, CA, 1996, pp. 545-551 vol.2.

[19] J. Dannehl, C. Wessels and F. W. Fuchs, "Limitations of Voltage-Oriented PI Current Control of Grid-Connected PWM Rectifiers With LCL Filters," in IEEE Transactions on Industrial Electronics, vol. 56, no. 2, pp. 380-388, Feb. 2009.

[20] Erika Twining and D. G. Holmes, "Grid current regulation of a three-phase voltage source inverter with an LCL input filter," in IEEE Transactions on Power Electronics, vol. 18, no. 3, pp. 888-895, May 2003.

[21] Poh Chiang Loh and D. G. Holmes, "Analysis of multiloop control strategies for LC/CL/LCL-filtered voltage-source and current-source inverters," in IEEE Transactions on Industry Applications, vol. 41, no. 2, pp. 644-654, March-April 2005.

[22] Y. W. Li, "Control and Resonance Damping of Voltage-Source and Current-Source Converters With LC Filters," in IEEE Transactions on Industrial Electronics, vol. 56, no. 5, pp. 1511-1521, May 2009.

[23] M. S. Munir, J. He and Y. W. Li, "Comparative analysis of closed-loop current control of grid connected converter with LCL filter," 2011 IEEE International Electric Machines & Drives Conference (IEMDC), Niagara Falls, ON, 2011, pp. 1641-1646.

[24] J. He and Y. W. Li, "Generalized Closed-Loop Control Schemes with Embedded Virtual Impedances for Voltage Source Converters with LC or LCL Filters," in IEEE Transactions on Power Electronics, vol. 27, no. 4, pp. 1850-1861, April 2012.

[25] T. Yokoyama and A. Kawamura, "Disturbance observer based fully digital controlled PWM inverter for CVCF operation," in IEEE Transactions on Power Electronics, vol. 9, no. 5, pp. 473-480, Sep 1994.

[26] O. Kukrer, "Deadbeat control of a three-phase inverter with an output LC filter," in *IEEE Transactions on Power Electronics*, vol. 11, no. 1, pp. 16-23, Jan 1996.

[27] O. Kukrer and H. Komurcugil, "Deadbeat control method for single-phase UPS inverters with compensation of computation delay," in IEE Proceedings - Electric Power Applications, vol. 146, no. 1, pp. 123-128, Jan 1999.

[28] P. Mattavelli, "An improved deadbeat control for UPS using disturbance observers," in IEEE Transactions on Industrial Electronics, vol. 52, no. 1, pp. 206-212, Feb. 2005.

[29] B. K. Bose, "An adaptive hysteresis-band current control technique of a voltage-fed PWM inverter for machine drive system," in IEEE Transactions on Industrial Electronics, vol. 37, no. 5, pp. 402-408, Oct 1990.

[30] E. Wu and P. W. Lehn, "Digital Current Control of a Voltage Source Converter With Active Damping of LCL Resonance," in IEEE Transactions on Power Electronics, vol. 21, no. 5, pp. 1364-1373, Sept. 2006.

[31] J. Dannehl, F. W. Fuchs and P. B. Thøgersen, "PI State Space Current Control of Grid-Connected PWM Converters With LCL Filters," in IEEE Transactions on Power Electronics, vol. 25, no. 9, pp. 2320-2330, Sept. 2010.

[32] J. Kukkola, M. Hinkkanen and K. Zenger, "Observer-Based State-Space Current Controller for a Grid Converter Equipped With an LCL Filter: Analytical Method for Direct Discrete-Time Design," in IEEE Transactions on Industry Applications, vol. 51, no. 5, pp. 4079-4090, Sept.-Oct. 2015.

[33] R. Turner, S. Walton and R. Duke, "Robust High-Performance Inverter Control Using Discrete Direct-Design Pole Placement," in IEEE Transactions on Industrial Electronics, vol. 58, no. 1, pp. 348-357, Jan. 2011.

[34] I. J. Gabe, V. F. Montagner and H. Pinheiro, "Design and Implementation of a Robust Current Controller for VSI Connected to the Grid Through an LCL Filter," in IEEE Transactions on Power Electronics, vol. 24, no. 6, pp. 1444-1452, June 2009.

[35] M. Xue, Y. Zhang, Y. Kang, Y. Yi, S. Li and F. Liu, "Full Feedforward of Grid Voltage for Discrete State Feedback Controlled Grid-Connected Inverter With LCL Filter," in IEEE Transactions on Power Electronics, vol. 27, no. 10, pp. 4234-4247, Oct. 2012.

[36] B. Li, M. Zhang, L. Huang, L. Hang, and L. M. Tolbert, "A new optimized pole placement strategy of grid-connected inverter with LCL-filter based on state variable feedback and state observer," in Proc. IEEE Appl. Power Electron. Conf., Mar. 2013, pp. 2900–2906.

[37] J. R. Massing, M. Stefanello, H. A. Grundling and H. Pinheiro, "Adaptive Current Control for Grid-Connected Converters With LCL Filter," in IEEE Transactions on Industrial Electronics, vol. 59, no. 12, pp. 4681-4693, Dec. 2012.

[38] M. Cespedes and J. Sun, "Adaptive Control of Grid-Connected Inverters Based on Online Grid Impedance Measurements," in IEEE Transactions on Sustainable Energy, vol. 5, no. 2, pp. 516-523, April 2014.

[39] J. Xu, S. Xie and T. Tang, "Improved control strategy with grid-voltage feedforward for LCL-filter-based inverter connected to weak grid," in IET Power Electronics, vol. 7, no. 10, pp. 2660-2671, Oct. 2014.

[40] S. Yang, Q. Lei, F. Z. Peng and Z. Qian, "A Robust Control Scheme for Grid-Connected Voltage-Source Inverters," in IEEE Transactions on Industrial Electronics, vol. 58, no. 1, pp. 202-212, Jan. 2011.

[41] IEEE Standard for Interconnecting Distributed Resources with Electric Power Systems, IEEE Std. 1547–2003, 2003.

[42] "High Voltage Solar Inverter DC-AC Kit," User's Guide, Texas Instruments, September 2014.

[43] Concerto F28M35x Technical Reference Manual. Available:

http://www.ti.com/lit/ug/spruh22h/spruh22h.pdf

[44] E. Twining, “Modeling grid-connected voltage source inverter operation,” in Proc. AUPEC’01, 2001, pp. 501–506.

[45] F. Wang, J. L. Duarte, M. A. M. Hendrix and P. F. Ribeiro, "Modeling and Analysis of Grid Harmonic Distortion Impact of Aggregated DG Inverters," in IEEE Transactions on Power Electronics, vol. 26, no. 3, pp. 786-797, March 2011.

[46] S. Buso and P. Mattavelli, Digital Control in Power Electronics, San Francisco, CA: Morgan & Claypool Publ., 2006.

[47] D. M. VandeSype, K. DeGusseme, F. M. L. L. DeBelie, A. P. VandenBossche and J. A. Melkebeek, "Small-Signal z-Domain Analysis of Digitally Controlled Converters," in IEEE Transactions on Power Electronics, vol. 21, no. 2, pp. 470-478, March 2006.

[48] X. Zhang, J. W. Spencer and J. M. Guerrero, "Small-Signal Modeling of Digitally Controlled Grid-Connected Inverters With LCL Filters," in IEEE Transactions on Industrial Electronics, vol. 60, no. 9, pp. 3752-3765, Sept. 2013.

[49] L. Asiminoaei, R. Teodorescu, F. Blaabjerg and U. Borup, "A new method of on-line grid impedance estimation for PV inverter," Applied Power Electronics Conference and Exposition, 2004. APEC '04. Nineteenth Annual IEEE, 2004, pp. 1527-1533 Vol.3.

[50] L. Asiminoaei, R. Teodorescu, F. Blaabjerg and U. Borup, "Implementation and Test of an Online Embedded Grid Impedance Estimation Technique for PV Inverters," in IEEE Transactions on Industrial Electronics, vol. 52, no. 4, pp. 1136-1144, Aug. 2005.

[51] M. Céspedes and J. Sun, "Online grid impedance identification for adaptive control of grid-connected inverters," 2012 IEEE Energy Conversion Congress and Exposition (ECCE), Raleigh, NC, 2012, pp. 914-921.

[52] M. Sumner, B. Palethorpe and D. W. P. Thomas, "Impedance measurement for improved power quality-Part 1: the measurement technique," in IEEE Transactions on Power Delivery, vol. 19, no. 3, pp. 1442-1448, July 2004.

[53] M. Ciobotaru, R. Teodorescu, P. Rodriguez, A. Timbus and F. Blaabjerg, "Online grid impedance estimation for single-phase grid-connected systems using PQ variations," 2007 IEEE Power Electronics Specialists Conference, Orlando, FL, 2007, pp. 2306-2312.

[54] Herong Gu, X. Guo, Deyu Wang and W. Wu, "Real-time grid impedance estimation technique for grid-connected power converters," 2012 IEEE International Symposium on Industrial Electronics, Hangzhou, 2012, pp. 1621-1626.

[55] B. Arif, L. Tarisciotti, P. Zanchetta, J. C. Clare and M. Degano, "Grid Parameter Estimation Using Model Predictive Direct Power Control," in IEEE Transactions on Industry Applications, vol. 51, no. 6, pp. 4614-4622, Nov.-Dec. 2015.

[56] S. C. Liu, K. C. Wu and Y. Y. Tzou, "Control of a single-phase grid inverter with on-line inductance identification," 2016 IEEE 25th International Symposium on Industrial Electronics (ISIE), Santa Clara, CA, USA, 2016, pp. 454-459.

[57] L. Harnefors, M. Bongiorno and S. Lundberg, "Input-Admittance Calculation and Shaping for Controlled Voltage-Source Converters," in IEEE Transactions on Industrial Electronics, vol. 54, no. 6, pp. 3323-3334, Dec. 2007.

[58] M. Céspedes and J. Sun, "Impedance shaping of three-phase grid-parallel voltage-source converters," 2012 Twenty-Seventh Annual IEEE Applied Power Electronics Conference and Exposition (APEC), Orlando, FL, 2012, pp. 754-760.

[59] D. Yang, X. Ruan and H. Wu, "Impedance Shaping of the Grid-Connected Inverter with LCL Filter to Improve Its Adaptability to the Weak Grid Condition," in IEEE Transactions on Power Electronics, vol. 29, no. 11, pp. 5795-5805, Nov. 2014.

[60] Xiao-Qiang Li, Xiao-Jie Wu, Yi-Wen Geng, and Qi Zhang; "Stability Analysis of Grid-Connected Inverters with an LCL Filter Considering Grid Impedance", Journal of Power Electronics, Vol. 13, No. 5, September 2013.

[61] C. Bao, X. Ruan, X. Wang, W. Li, D. Pan and K. Weng, "Step-by-Step Controller Design for LCL-Type Grid-Connected Inverter with Capacitor–Current-Feedback Active-Damping," in IEEE Transactions on Power Electronics, vol. 29, no. 3, pp. 1239-1253, March 2014.

[62] F. Liu, Y. Zhou, S. Duan, J. Yin, B. Liu and F. Liu, "Parameter Design of a Two-Current-Loop Controller Used in a Grid-Connected Inverter System With LCL Filter," in IEEE Transactions on Industrial Electronics, vol. 56, no. 11, pp. 4483-4491, Nov. 2009.

[63] Xiaoming Yuan, W. Merk, H. Stemmler and J. Allmeling, "Stationary-frame generalized integrators for current control of active power filters with zero steady-state error for current harmonics of concern under unbalanced and distorted operating conditions," in IEEE Transactions on Industry Applications, vol. 38, no. 2, pp. 523-532, Mar/Apr 2002.

[64] R. Teodorescu, F. Blaabjerg, U. Borup and M. Liserre, "A new control structure for grid-connected LCL PV inverters with zero steady-state error and selective harmonic

compensation," Applied Power Electronics Conference and Exposition, 2004. APEC '04. Nineteenth Annual IEEE, 2004, pp. 580-586 Vol.1.

[65] Y. Zhuhuan, X. Guochun, Z. Zhong, T. Guofei and J. Yaoqin, "PR and harmonic compensation control scheme with current state feedback for an single-phase Active Voltage Quality Regulator," 8th International Conference on Power Electronics - ECCE Asia, Jeju, 2011, pp. 2749-2756.

[66] M. J. Newman and D. G. Holmes, "Delta operator digital filters for high performance inverter applications," in IEEE Transactions on Power Electronics, vol. 18, no. 1, pp. 447-454, Jan 2003.

[67] R. Teodorescu, F. Blaabjerg, M. Liserre and P. C. Loh, "Proportional-resonant controllers and filters for grid-connected voltage-source converters," in IEE Proceedings - Electric Power Applications, vol. 153, no. 5, pp. 750-762, September 2006.

[68] X. Wang, X. Ruan, S. Liu and C. K. Tse, "Full Feedforward of Grid Voltage for Grid-Connected Inverter With LCL Filter to Suppress Current Distortion Due to Grid Voltage Harmonics," in IEEE Transactions on Power Electronics, vol. 25, no. 12, pp. 3119-3127, Dec. 2010.

[69] J. Xu, Q. Qian, S. Xie and B. Zhang, "Grid-voltage feedforward based control for grid-connected LCL-filtered inverter with high robustness and low grid current distortion in weak grid," 2016 IEEE Applied Power Electronics Conference and Exposition (APEC), Long Beach, CA, 2016, pp. 1919-1925.

[70] Jae-Young Jang, Kyo-Beum Lee, Joong-Ho Song and Ick Choy, "Disturbance observer-based digital control for single-phase UPS inverters," ISIE 2001. 2001 IEEE International Symposium on Industrial Electronics Proceedings (Cat. No.01TH8570), Pusan, 2001, pp. 1095-1105 vol.2.

[71] H. Haga, K. Sayama, K. Ohishi and T. Shimizu, "Current control system based on repetitive control and disturbance observer for single-phase five-level inverter," IECON 2015 - 41st Annual Conference of the IEEE Industrial Electronics Society, Yokohama, 2015, pp. 004370-004375.

[72] A. Radke and Zhiqiang Gao, "A survey of state and disturbance observers for practitioners," 2006 American Control Conference, Minneapolis, MN, 2006.

[73] P. Cortes, G. Ortiz, J. I. Yuz, J. Rodriguez, S. Vazquez and L. G. Franquelo, "Model Predictive Control of an Inverter With Output LC Filter for UPS Applications," in IEEE Transactions on Industrial Electronics, vol. 56, no. 6, pp. 1875-1883, June 2009.

[74] Dou, X., Yang, K., Quan, X., Hu, Q., Wu, Z., Zhao, B., Li, P., Zhang, S., Jiao, Y. An Optimal PR Control Strategy with Load Current Observer for a Three-Phase Voltage Source Inverter. Energies 2015, 8, 7542-7562.